PREPARATION AND PROPERTIES OF THERMALLY/ELECTRICALLY CONDUCTIVE MATERIAL ARCHITECTURES BASED ON GRAPHENE AND OTHER NANOMATERIALS

A Thesis
Presented to
The Academic Faculty

by

Qizhen Liang

In Partial Fulfillment
of the Requirements for the Degree
Doctor of Philosophy in
School of Polymer, Textile and Fiber Engineering

Georgia Institute of Technology
August 2011

PREPARATION AND PROPERTIES OF THERMALLY/ELECTRICALLY CONDUCTIVE MATERIAL ARCHITECTURES BASED ON GRAPHENE AND OTHER NANOMATERIALS

Approved by:

Dr. C. P. Wong, Advisor
School of Materials Science and Engineering
Georgia Institute of Technology

Dr. Meilin Liu
School of Materials Science and Engineering
Georgia Institute of Technology

Dr. Karl Jacob
School of Materials Science and Engineering
Georgia Institute of Technology

Dr. Donggang Yao
School of Materials Science and Engineering
Georgia Institute of Technology

Dr. Anselm Griffin
School of Materials Science and Engineering
Georgia Institute of Technology
Date Approved: June 14, 2011

PREPARATION AND PROPERTIES OF THERMALLY/ELECTRICALLY CONDUCTIVE MATERIAL ARCHITECTURES BASED ON GRAPHENE AND OTHER NANOMATERIALS

Approved by:

Dr. C. P. Wong, Advisor
School of Materials Science and Engineering
Georgia Institute of Technology

Dr. Meilin Liu
School of Materials Science and Engineering
Georgia Institute of Technology

Dr. Karl Jacob
School of Materials Science and Engineering
Georgia Institute of Technology

Dr. Donggang Yao
School of Materials Science and Engineering
Georgia Institute of Technology

Dr. Anselm Griffin
School of Materials Science and Engineering
Georgia Institute of Technology

Date Approved: June 14, 2011

To my family

ACKNOWLEDGEMENTS

I wish to address my great appreciation to those contributed to my research in Ph.D degree study. The first should be acknowledged is Dr. CP Wong, my thesis advisor, for his instructive advisory. During the past 5 years of a fruitful study on various topics in materials science and engineering, Dr. Wong encouraged to handle challenging topics and provide me opportunities to stand on the most front of real industrial applications. I also feel that I should appreciate my cooperators in various research topics and related publications, for their instructive enlightening and help in access to various instruments to realize my ideas. They are Dr. Wei Wang, Ms. Xuxia Yao, Dr. Lingbo Zhu, Dr. Yonghao Jiang, Dr. Hongjin Jiang, Mr. Sinsar A Hsie, Mr. Ken Wilkons (Polymer Ageing Conception Co. GA), Ms Lilian T. Morato (Polymer Ageing Conception Co. GA), and Dr. Madeline Feltus (US Department of Energy).

I also wish to thanks most of members in Dr. Wong's research group at School of Materials Science and Engineering, Georgia Tech. Some of them are mentioned above. In particular, the other individuals include: Dr. Jiongxin Lu, Dr. Yi Li, Ms. Yan Liu, Mr. Ziyin Lin, Dr. Rongwei Zhang, and Mr. Owen Heldrich.

My teachers and friends at Georgia Tech should also be appreciated not only for their great help within college-wide region but also for my personal life issues in my Ph. D study. Their help contribute to every achievement that I have made and assist me past even the hardest time. They are Dr. Mohan Srinivasarao, Dr. Anselm Griffin, Dr. Meilin Liu, Dr. Karl Jacob, Dr. Donggang Yao, Ms. Xuxia Yao, Dr. Wei Zhang, Dr. Zhan Liu, Dr. Wenjun Xu, Mr. Yao Li, Dr. Chunqing Peng, Dr. Xuejia Yan, Mr. Bo Xu, Mr. Benjamin Findley, *et al*.

Finally, I would like to thanks my parents, my uncle, and my brother for their supporting and encouraging during all career of studying ever since 1986.

TABLE OF CONTENTS

LIST OF TABLES

Page

LIST OF FIGURES

Page

LIST OF SYMBOLS AND ABBREVIATIONS

k	Thermal conductivity
α	Thermal diffusivity
ρ	Density
C_p	Heat capacity
R_s	Sheet electrical resistance
R	Measured electrical resistance
W	Sample width
L	Sample length
C_{oxygen}	Oxygen concentration on GO
P_{O1s}	Integrated area of O1s peak
P_{C1s}	Integrated area of C1s peak
S_{O1s} and S_{C1s}	Empirical atomic sensitivity factor of C1s and O1s, respectively
A	Optical absorption
T	Optical Transparency
α'	Absorption coefficient
$\alpha_{//}$ and $\alpha_{\perp}$	In-plane and out-of-plane coefficient of thermal expansion, respectively
θ	Angle between polarization of incident light and fMGs orientation
$I_{VV}(\theta)$	Measured G band Raman intensity in "*VV*" configuration
$I_{VH}(\theta)$	Measured G band Raman intensity in "*VH*" configuration
$I_{R,VV}(\theta)$	Relative G band Raman intensity in "*VV*" configuration
$I_{R,VH}(\theta)$	Relative G band Raman intensity in "*VH*" configuration

$\sigma_{//}$ and $\sigma_{\perp}$	In-plane and out-of-plane electrical conductivity, respectively
$\rho_{//}$ and $\rho_{\perp}$	In-plane and out-of-plane electrical resistivity, respectively
$k_{//}$ and $\sigma_{\perp}$	In-plane and out-of-plane thermal conductivity, respectively
R_{TIM}	Total thermal resistance of TIM architecture
BLT	Bottom-line thickness
$R_{A-fMGs/In/Si}$	Thermal resistance across the A-fMGs/In/Si multiple interface
p	Vacuum concentration of fillers
p_c	Percolation threshold
C	Relative weight factor of epoxy resin matrix
n	Exponent of power equation (Order of) polymer degradation reaction
t	Age of epoxy/carbon black composite
x	Weight ratio of carbon black in epoxy matrix

LIST OF ABBREVIATIONS

AFM	Atomic force microscopy
A-fMGs	Aligned functionalized multilayer graphene
CNFs	Carbon nanofibers
CNTs	Carbon nanotubes
CPCs	Conductive Polymer Composites
CTE	Coefficient of thermal expansion
CVD	Chemical vapor deposition
DMA	Dynamic mechanical analysis/analyzer
DSC	Differential scanning calorimeter
fMGs	Functionalized multilayer graphene
FTIR	Fourier-Transform Infrared (spectrum/spectroscopy)
GO	Graphene oxide
GPTMS	γ-glycidoxypropyl-trimethoxysilane
HOPG	Highly ordered pyrolytic graphite
MHHPA	4-Methylhexahydrophthalic anhydride
MW	Microwave
MWNTs	Multi-walled carbon nanotubes
RA-fMGs	Recumbent aligned functionalized multilayer graphene
SEM	Scanning electronic microscopy
TECs	Transparent electrical conductors
TGA	Thermo gravimetric analysis/analyzer
TIMs	Thermal interfacial materials
TMA	Thermo mechanical analysis/analyzer
VA-CNFs	Vertically aligned carbon nanofibers

VA-CNTs	Vertically aligned carbon nanotubes
VA-fMGs	Vertically aligned functionalized multilayer graphene
VFM	Variable frequency microwave system
"*VH*"	Vertical/ horizontal configurations of polarized Raman measurement
"*VV*"	Vertical/vertical configurations of polarized Raman measurement

SUMMARY

With excellent electrical, thermal and mechanical properties as well as large specific surface area, graphene has been applied in next-generation nano-electronics, gas sensors, transparent electrical conductors, thermally conductive materials, and superior energy capacitors *etc*. Convenient and productive preparation of graphene is thereby especially important and strongly desired for its manifold applications.

Chemically developed functionalized graphene from graphene oxide (GO) has significantly high productivity and low cost, however, toxic chemical reduction agents (*e.g.* hydrazine hydrate) and raised temperature (400-1100°C) are usually necessary in GO reduction yet not preferred in current technologies. Here, microwaves (MW) are applied to reduce the amount of graphene oxide (GO) at a relatively low temperature (~165^{o}C). Experimental results indicate that resurgence of interconnected graphene-like domains contributes to a low sheet resistance with a high optical transparency after MW reduction, indicating the very high efficiency of MW in GO's reduction.

Moreover, graphene is usually recumbent on solid substrates, while vertically aligned graphene architecture on solid substrate is rarely available and less studied. For TIMs, electrodes of ultracapacitors, *etc*, efficient heat dissipation and electrical conductance in normal direction of solid surfaces is strongly desired. In addition, large-volume heat dissipation requires a joint contribution of a large number of graphene sheets. Graphene sheets must be aligned in a large scale array in order to meet the requirements for TIM application. Here, thermally conductive fuctionalized multilayer graphene sheets (fMGs) are efficiently aligned in a large scale by vacuum filtration method at room temperature, as evidenced by SEM images and polarized Raman

spectroscopy. A remarkably strong anisotropy in properties of aligned fMGs is observed. Moreover, VA-fMG TIMs are prepared by constructing a three-dimensional vertically aligned functionalized multilayer graphene architecture between contact Silicon/Silicon surfaces with pure Indium as a metallic medium. Compared with their counterpart from recumbent A-fMGs, VA-fMG TIMs have significantly higher equivalent thermal conductivity and lower contact thermal resistance.

Electrical and thermal conductivities of polymer composite are also greatly interested here. Previous researches indicated that filler loading, morphology of fillers, and chemical bonding across filler/polymer interfaces have significant influence on electrical/thermal conductivity of polymer composite. Therefore, the research also pays substantial attention to these issues. First, electrical resistivity of CPCs is highly sensitive on volume or weight ratio (filler loading) of conductive fillers in polymer matrix, especially when filler loading is close to percolation threshold (p_c). Thermal oxidation aging usually can cause a significant weight loss of polymer matrix in a CPC system, resulting in a filler loading change which can be exhibited by a prompt alteration in electrical resistivity of CPCs. Here, the phenomena are applied as approach for *in-situ* monitoring thermal oxidation status of polymeric materials is developed based on an electrical sensors based on conductive polymeric composites (CPCs). The study developed a model for electrical resistivity of sensors from the CPCs as a function of aging time at constant aging temperature, which is in a good agreement with a Boltzmann-Sigmoidal equation. Based on the finding, the sensors show their capability of *in-situ* in-situ monitor and estimate aging status of polymeric components by a fast and convenient electrical resistance measurement.

Second, interfacial issues related to these thermal conductive fillers are systemically studied. On the one hand, the study focuses on relationship between morphology of h-BN particles and thermal conductivity of their epoxy composites. It is

found that spherical-agglomeration of h-BN particles can significantly enhance thermal conductivity of epoxy resin, compared with dispersed h-BN plates, by substantially reducing specific interfacial area between h-BN and epoxy resin. On the other hand, surface of high thermal conductive fillers such as SiC particles and MWNTs are successfully functionalized, which makes their surface reactive with bisphenol A diglycidyl ether and able to form chemical bonding between fillers and epoxy resin. By this means, thermal conductivity of polymer composites is found to be significantly enhanced compared with control samples, indicating the interfacial chemical bonding across interface between thermal conductive fillers and polymer matrix can promote heat dissipation in polymeric composites. The finding can benefit a development of high thermal conductive polymer composites by interfacial chemical bonding enhancement to meet the demanding requirements in current fine pitch and Cu/low k technology.

CHAPTER 1 INTRODUCTION

The aim of the research is to development of various thermally/electrically conductive architectures based on graphene and other nanomaterials, which are currently widely interested. Here, material architectures are developed and studied not only for various industry-compatible applications but also for further scientific understanding of several important issues in the research region.

Graphene, a building material of several important carbon allotropies such as fullerenes, carbon nanotubes, and graphite, is chemically stable in common environment and physically excellent in mechanical, electronic and thermal properties [1]. Ever since graphene's discovery in 2004 [2], substantial efforts have been made in order to understand its physical structure, explore its properties, and further its applications for various propose. With the early-stage efforts, graphene has been found promising in field-effect-transistors [3], electrodes of energy-collectors [4], transparent conductors [5, 6, 7], thermal conductive materials[8], sensors [9], and so on. However, major barriers in preparation of graphene still exist, which has been preventing its large-volume manufacture as well as broad applications. Studies here pay effort to handle several bottlenecks in preparation and property optimization of graphene architecture, and provide instructive solutions with promising potentials, which will promote the application of graphene for transparent conductive conductors, thermal interfacial materials, fillers in polymer composites, etc.

Moreover, it is noticed that real industrial applications give various requirements for conductive materials. Among current conductive materials (*e.g.* metals and metallic alloys), most are both electrically and thermally conductive, which could satisfy many traditional applications (*e.g.* electrical cords for power transmission). However, exceptional situation always exist, as industrial requirements keep becoming more demanding. For instance, thermally conductive electrical-insulators are strongly desired

for underfill materials, which are important for packaging of photonics and electronic devices. Naturally, here, electrically-insulating yet thermally conductive nano-materials with acceptable cost, such as boron nitride, surface treated silicon carbide, *etc*, are also chosen and studied as thermal conductive fillers. Properties of their polymer composites are also significantly highlighted in the study for their excellent preformance in industrial applications.

In summary, graphene as well as a series of other nanomaterials are applied as thermally and electrically conductive materials in several different architectures, which are important for various applications, such as transparent electrical conductors, thermal interfacial materials, packaging materials for electronics, *in-situ* polymer aging sensors, *etc*.

1.1 Graphene

1.1.1 A Network from Conjugated sp^2-hybridized carbon atoms

As one of the most important elements, carbon is a component of most molecules in the world. As the lightest atom in the sixth element group, carbon has six electrons, among which the outermost four electrons usually occupy $2s^2 2p^2$ atomic orbital. The relatively low energy difference between $2s^2$ and $2p^2$ allows at least three hybridized atomic orbitals such as sp, sp^2 and sp^3 of carbon atoms, through which the four valence electrons of carbon atoms can form various covalent bonds with other atoms. Thus, the hybridized atomic orbitals of carbon element provide almost infinite possibility of innumerable molecule structures. Moreover, with a view angle of material science, stereoscopic structures of the most common hybrid atomic orbitals sp, sp^2 and sp^3 provide especially-interested and powerful strategies of material design.

Carbon nano-materials have been highlighted as one of the most interested next generation materials groups for structural, electronic, thermal, and photonic applications. Current research on carbon nano-materials has been broadened extensively from “zero-

dimensional" fullerenes, to 1D carbon nanotubes, 2D graphene structures and 3D diamond-like nanoparticles.

Among these carbon nanomateirals, 2-D graphene is being highlighted in current research. However, until its discovery in 2004, graphene had not been widely interested nor studied. Calculation results indicated that a graphene structure with less than 6000 carbon atom is most unstable compared among carbon allotropes, e. g. fullerenes, while it becomes most stable if the carbon atom number exceeds 24,000. Confirming these, it was found that synthesis of a polycyclic aromatic structure with more than 222 carbon atoms is very difficult. In 2004, researchers form University of Manchester broke the experimental barriers by developing a drawing method for graphene preparation. As a network from regularly stacked sp^2-hybrided carbon atoms lattice, graphene is a flat film of carbon atoms bonded with π-π conjugated covalent bonds in honeycomb-like hexagonal rings in which carbon-carbon bond length is ~0.142 nm. Also, originally prepared from mechanically exfoliating highly ordered pyrolytic graphite (HOPG), graphene can be considered as an isolated layer unit of graphite. Due to the unique structure, graphene is considered as a "building material" of various daughter carbon allotropies, such as fullerenes, carbon nanotubes, and graphite, as schematically illustrated in Figure 1.1 [10, 11, 12].

Derived from similar chemical structure with other carbon nanomaterials (e.g. carbon nanotubes), it is not surprising that graphene can usually react with various chemicals in similar way as that of fullerenes, which has been substantially reported recently. Moreover, many properties of graphene are quite similar as those of carbon nanotubes. For example, thermal conductivity of free-standing graphene sheets is ~ 6000W/m K, which is very close to the reported values of carbon naotubes around 5300W/m K.

Moreover, although the name "graphene" is theoretically applied to describe a monolayer carbon film as maintained above, it is noticed that research on graphene has

been widely expanded to those carbon nanomaterials with chemical structures closely related to graphene such as graphene oxide, few- or multi- layer graphene sheets, graphene ribbons, etc., most of which have considerable functional groups.

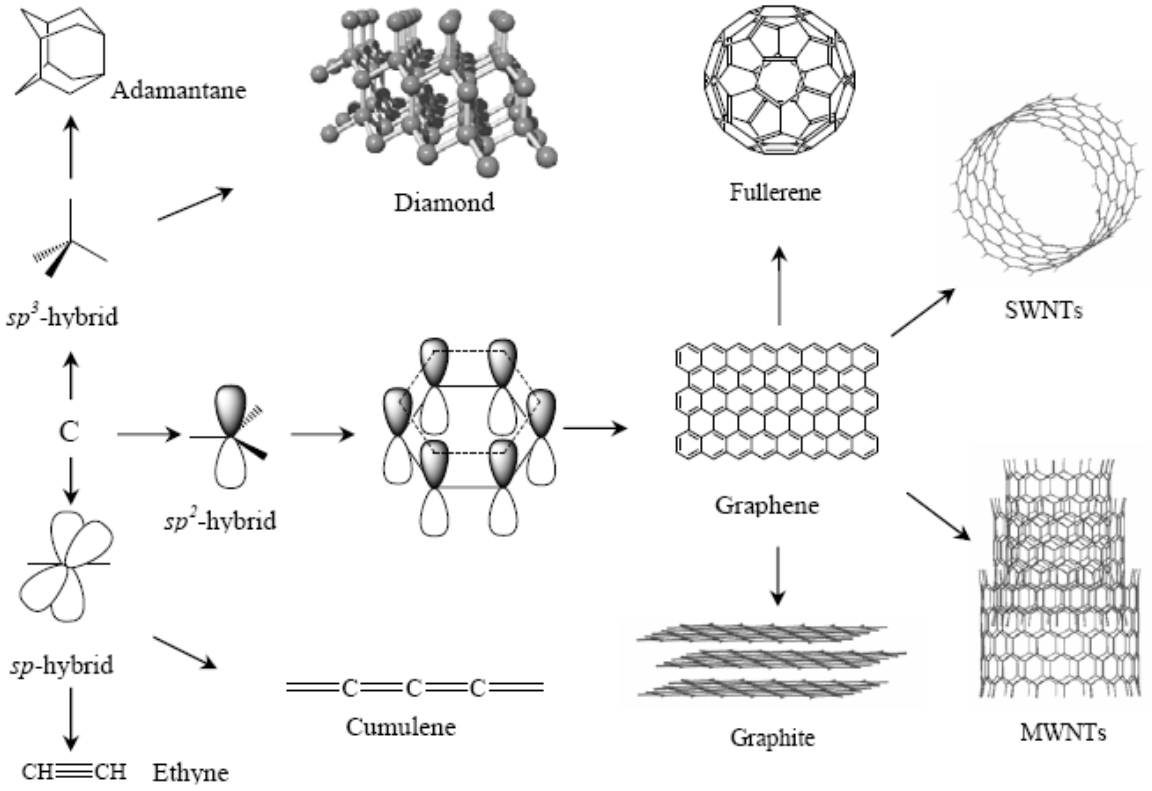

Figure 1.1 Graphene as a building material of fullerene, SWNT, MWNT and Graphite [1, 10, 11].

1.1.2 Functional groups on graphene

Graphene can be conveniently functionalized by carbonhydroxyl (-OH), carboxyl (-COOH), epoxide, carbonyl (C=O), etc. [13, 14] These oxygen-containing polar functional groups are usually introduced by oxidation of graphene sheets in chemical development or chemical vapor deposition process. It is found that functional group distribution on graphene is non-evenly. For example, both simulation results and experimental indicated that carboxyl groups on graphene is highly concentrated on edge domain of graphene sheets, which epoxide and diols is mainly on body domains [15].

It has been found that functional groups as well as defects on graphene sheets change energy level of graphene [16, 17, 18], naturally, chemical and physical properties of graphene can be significantly affected by functional groups. Usually, functional groups mainly affect graphene's properties by two effects.

On the one hand, functional groups increase solubility of graphene in polar solvents such as water, DMAc, acid solutions, NMPs. [19, 20] This is extremely important for processing graphene-based nanomaterials. Thus functionalized graphene sheets can be processed in inorganic/organic polar solvents and conveniently coated on various solid substrates, which significantly facilitates processing of graphene in large-volume preparations, further-functionalizations, and real industrial applications.

On the other hand, functional groups destroy conjugation of π-π covalent bonding among carbon atoms. In pristine graphene, carbon atoms are sp^2-hybrided and well aligned in fine lattice of a two-dimensional film-like network. In contrast, most functionalized carbon atoms on graphene are tetrahedral sp^3-hybride and tend to be out of graphene plane. Moreover, functionalization of graphene usually introduce defects on fine crystal lattice of graphene and cause high phonon scattering along graphene sheets, hence a significant reduction of thermal conductivity by 3 or 4 orders of magnitudes, compared with that of pristine graphene [21].

In summary, in current study of graphene, functional groups on graphene are so influential that the research has been highlighted and will be one of important target of effort in future study.

1.2 Properties of Graphene

1.2.1 Electronic properties

Band structure

Graphene is found to be a zero band-gap semiconductor, which makes graphene's electrical properties dramatically different form graphite, a "daughter" material built from

a large number of graphene layers. Band structure of graphene is usually described by a "tight-bonding" model [22, 23]. In the model, the wave vector (k) of electronic energy of graphene structure can be expressed in equation as follows.

$$E = \pm\sqrt{\gamma_0^2\left(1+4\cos^2\frac{k_y a}{2}+4\cos\frac{k_y a}{2}\cdot\cos\frac{k_x\sqrt{3}a}{2}\right)}$$

Where γ_0 and a represent "the nearest-neighbour hopping energy" (2.8eV) and "lattic constant" (2.46 $\mathring{A}$), respectively. Schematically plotted in a 3D graph, as shown in Figure 1.2 [22, 23], electron energy of carbon atoms in a hexagonal structure of graphene (Brillouin zone) shows a Direc structure with only two freedom degrees, which is also called as "two-spinor" structure. Therefore, electrons and holes in the band structure are usually named as Direc femins, while the six carbon atom members are called Direc points.

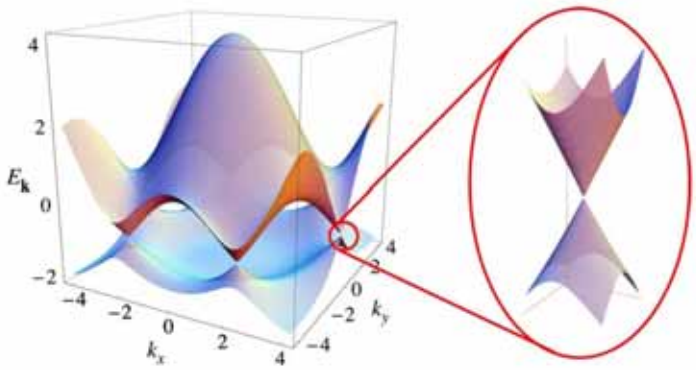

Figure 1.2 A schematic illustration of graphene's band structure from tight-binding bonding. (Castro Neto et al, *Review of Modern Physics,* 2009 [23])

Ultra-high mobility

In 2004, Novoselov, K. S and Geims A. K. measured mobility of graphene with both field effect and magnetoresistance methodologies and obtained results with high agreement [1, 2]. Although it is found that defects on graphene sheets can influent, both of the measurement indicated that mobility of graphene is not significantly depend on temperature in the measurement. Thus, mobility of graphene is found to be ultra-high

(exceeding 15, 000 cm^2 V^{-1} s^{-1} at room temperature [2]). Meanwhile, theoretically, electrical resistance of grphene calculated from the ultra-high mobility values can be as low as 10^{-6} Ω•cm, which is even lower than that of silver. However, electrical resistance of graphene in real application may not reach its theoretical value due to effect of solid substracts, phone scattering from graphene to environment, so that the mobility and electrical resistance of graphene are usually limited.

1.2.2 Thermal properties

Heat dissipation along graphene is carried out through phonon transportation. It is believed that graphene has at least three phonon mode: LA, TA, and ZA, among which LA and TA are in-plane phone mode while ZA is an out-of-plane phonon mode. Based on a phonon-dominated heat transportation model, Balandin A A et al reported a non-contact thermal conductivitity measurement carried on a Raman spectrometer and reported an ultra-high thermal conductivitity of suspended monolayer graphene at room temperature as 4.8-5.3 $\times 10^3$ W m^{-1} K^{-1} [8], which is much higher than that of HOPG (~1 $\times 10^3$ W m^{-1} K^{-1}). However, thermal conductivity graphene is highly sensitive on environmental issues. It has been found that thermal conductivity of graphene on silicon substrate can be much lower (600 W m^{-1} K^{-1} [24]) due to phonon scattering between graphene sheets and solid substrate.

Moreover， unfortunately, it is noticed that the promising thermal conductivity of graphene are limited to the lateral direction within a single nano plate region [25, 26] of an isolated graphene sheet. Moreover, compared with the phonon transport along chemical bonds in lateral direction, phonon transfer between the graphene layers is conducted by Van der Waals forces, which are much weaker than chemical bonds and can scatter phonons [27, 28].

1.2.3 Mechanical properties

Lee C et al [29] measured mechanical properties of graphene from drawing method, which were suspended on SiO_2 in 2008. In the test, an AFM tip was applied inorder to measure several important parameters of mechanical properties. Thus, graphene is found to be the strongest material in the world with a tensile strength of ~130GPa, a spring constant of 1-5N/M and a Young's modulus of 0.5TPa. These mechanical properties indicated that graphene is a strong rigid material. However, bending, crumpling and thermal fluctuations are also observed on graphene sheets, indicating is also flexiable in out-of-plane direction. It is also noticed that the ultra-high strength of graphene can be accounted for the remarkable mechanical properties of it daughter mateials such as carbon nanotubes.

1.2.4 Specific surface area

With a thin single-atomic-layer film-like structure, specific surface area of graphene is theoretically as high as $2675 m^2/g$ [4, 30], which is critically important for specifica-surface-area sensitive applications such as electrodes of energy collectors and polymer composites. Calcultion indicated that capacitiy of ultra-capacitor can be theoretically as high as 550 F/g due to the ultra-high specific surface area of graphene.

1.2.5 Optical properties

It is believed that graphene's transparency is more closely related to quantum effect than traditional material properties. The 2D nature of graphene as well as the zero-gap Dirac band structure contribute a fine-structure constant of graphene which can be expressed by following Equation:

$$a = \frac{e^2}{\hbar c} \qquad \textbf{Equation 1.1}$$

Ando T (2002) and Gusynin V.P. (2006) reported that dynamic conductivity (G) of graphene is constant ($\frac{e^2}{4\hbar}$) [31, 32]. Moreover, calculation indicated that transparency

(T) and reflectance (R) of graphene can be approximated and described in following equation [33]:

$$T \approx 1 - \pi a \qquad \textbf{Equation 1.2}$$

$$R = \frac{\pi^2 \alpha^2 T}{4} \qquad \textbf{Equation 1.3}$$

As shown in Figure 1.3, transparency of graphene is found constant within visual-light wave-length (400-740nm), as reported by Nair R. R. *et al* in 2008 [34]. It is found that each layer of graphene contributes ~2.3% ($\pi\alpha$) light absorption in the frequency region, corresponding to a "fine-structure constance" (α) of $\sim \frac{1}{137}$. The agreement between theoretical calculations and experimental results confirmed that optical properties of graphene are dominated by quantum effects.

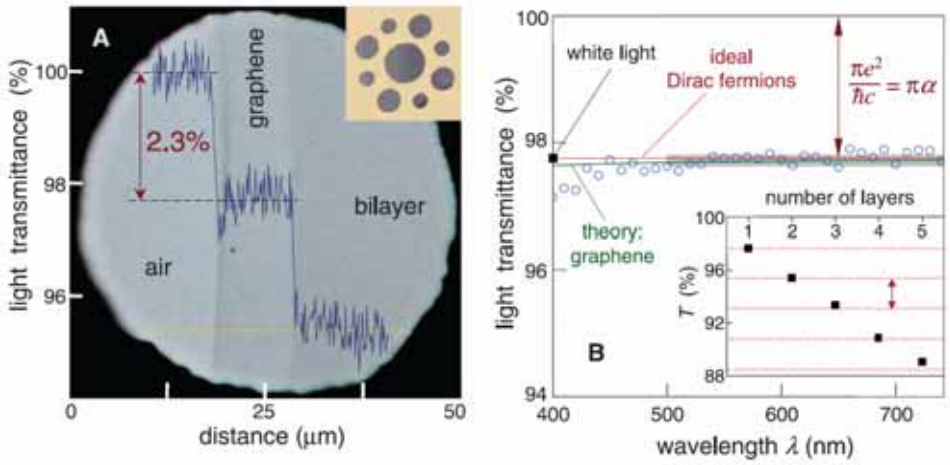

Figure 1.3 Graphene as transparent electrical conductors (Nair R. R. *et al*, 2008 [34]).

1.3 Preparation of Graphene

As a new generation material with excellent properties described above, graphene is substantially interested in various application so that convenient preparation is important and has draw remarkable attentions form researchers. Current researches indicated that graphene can be prepared in various methods such as mechanical

exfolication of HOPG, epitaxal growth on SiC substracts, chemical vapor deposition on metallic substracts, chemical development from graphite, etc [35].

1.3.1 Mechanical exfoliation of HOPG

At the forestage research of graphene, highly ordered pyrolytic graphite (HOPG) was peeled off repeatedly with a scotch tape. As shown by Figure 1.4, highly ordered pyrolytic graphite (HOPG) can be considered as fine lattice with parallel-stacked graphene, among which van der Waals force hold the stacked graphene layers together with an average layer distance of ~0.35nm. Compared with covalent chemical bonding among carbon atoms within graphene plane, van der Waals forces graphene layers are relatively weak, allowing a covenient separation of graphene layers. In 2004, Noveselov, K. S.and Geim, A. K.*et al.* split HOPG by using cohesive tapes, dispersed exfoliated graphite plates in organic solvent (acetone) and measured thickness of thus prepared graphene by AFM measurement [1, 36]. It is found that thus prepared exfolicated graphite plates are a mixture of plates with various number of layers (from monolayer to tens of layers).

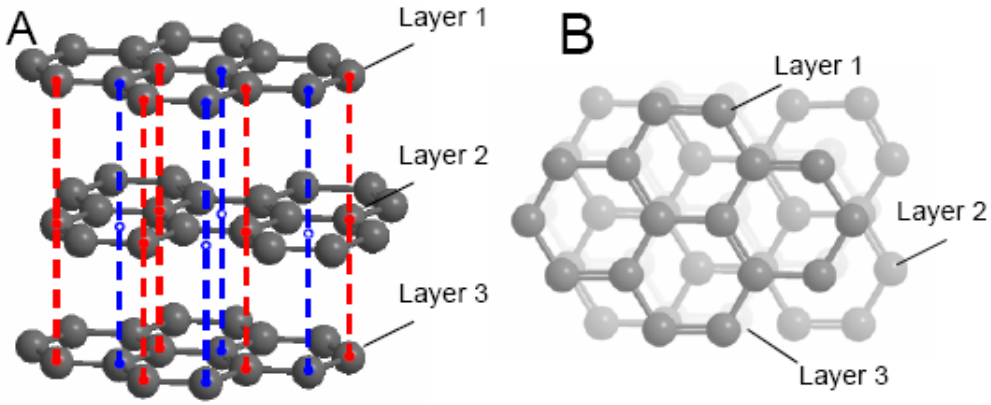

Figure 1.4 A schematic illustration of fine crystal lattice of graphite. A: A side view of graphite structure. B: A top view of graphite structure.

Although the methodology requires very primary experimental conditions in preparation, however, yields of graphene in this method are extremely low and significant

difficulty is involved in searching the substrates by AFM tips for single sheets among a huge number of multilayer graphene plates. With further understanding of graphene's optical property, the methodology is simplified thereafter by determinating thickness of exfolicated graphite plates with optical transparency. With development efforts in several years, the methodology is capable in preparing monolayer graphene with lateral dimensions of ~tens of micrometers.

1.3.2 Epitaxial growth

Almost at same time in 2004, researchers at Georgia Institute of Technology reported that ultra-thin large-scale graphite coating on SiC substracted was successfully prepared by reduction of SiC [37, 38], providing an attractive alternative methodology for high-quality mono- or few-atomic-layer graphene. It is found that both Si and C side of SiC can be applied in order to prepare graphene with the method, although electronic structure and properties of graphene from the two kind of surface is significantly different. The methodology greatly contributed to research of graphene's Dirac Cone structure, quantum Hall effects research and so on [39, 40, 41, 42], by providing a large-scale (with same size of SiC substract) continuous graphene plates.

Benefiting from the relatively large yield and fine quality, graphene from the expitaxal growth methodology can be conveniently patterned and is promising in large-scale electronics [43]. However, it is also noticed that temperatures up to 1100^{o}C and ultra-high vacuum degree are needed in the methodology, while a high temperature processing is also unlikely to be compatible with the fabrication technology used in current electrical and chemical industry.

1.3.3 CVD method

Chemcial vapor deposition can also be applied in order to prepare epitaxal grown graphene on metal substracts [44]. The method is capable in preduce single or few layer

graphene plates with area larger than 1cm^2. Various metals such as Ni, Ir, Ru, Cu, etc. has been applied as catalyst and substracts in the methodology [45, 46].

1.3.4 Chemically developement

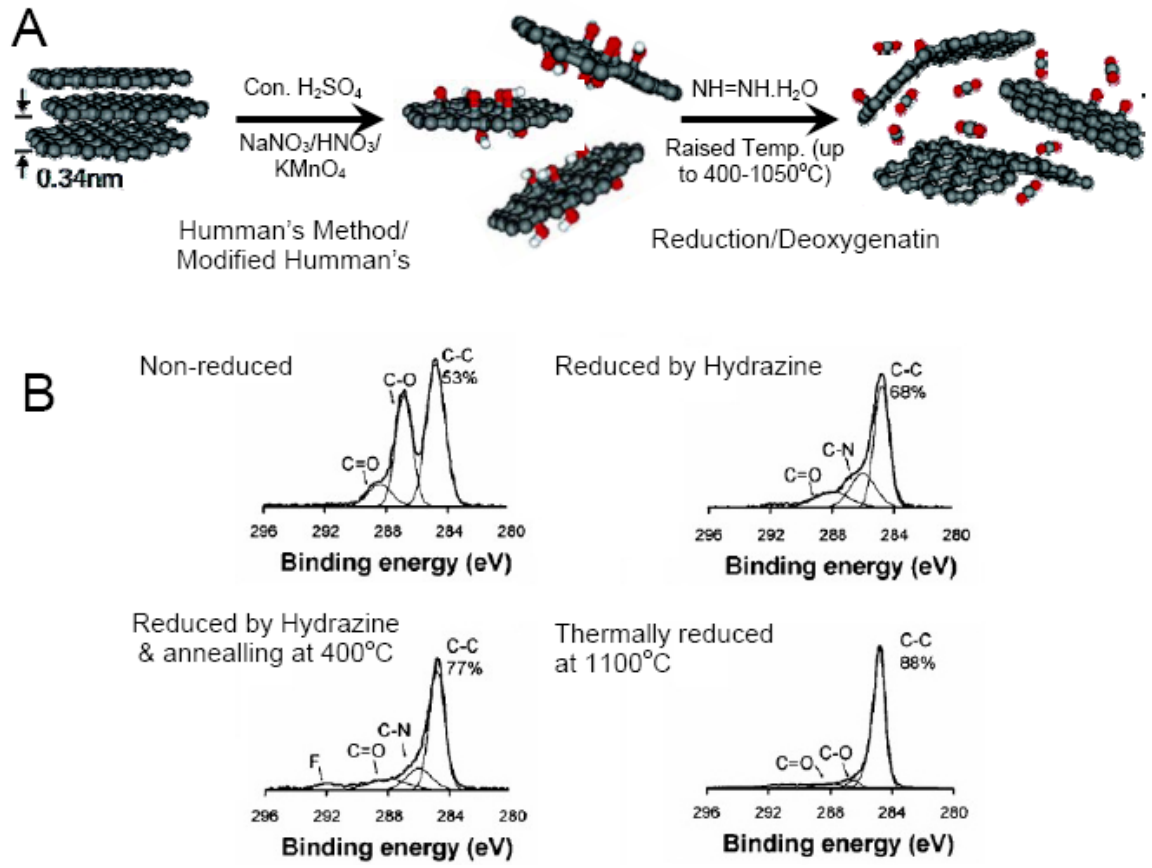

Figure 1.5 A: A schematic illustration of chemical development of graphene oxide by Humman's Medthod and consequent reduction (McAllister *et al, Chem. Mater.* 2007) [47]. B: A comparision among XPS spectra of graphene oxide and its reduction products from different reduction methodologies. (Becerri *et al, ACS Nano,* 2008) [5].

Preparation of chemically developed functionalized graphene from graphene oxide (GO) has significantly high productivity and low cost, thereby has been extensively interested. However, usually prepared by an extreme oxidation of graphite flakes, graphene oxide is highly functionalized with decorating polar groups such as carboxyls, hydroxyls, diols, *etc*, on irregular-sized graphene-like domains [13, 14], which deliver an excellent water solubility of GO [19, 20]. These polar groups on GO inevitably introduce

structural defects on fine pattern of pristine graphene, destroy conjugation among sp^2 hybridized carbon atoms as well as interconnection between of graphene-like domains, and thereby significantly reduce electrical conductance of GO. Removal of polar groups by chemical or thermal reduction can help resurgence of an interconnected graphene structure [48].

Functionalized mono- or few-layer graphene can be prepared starting from HOPGs graphite oxide (GO). GO can be prepared by oxidation and thermal expansion of graphite [47, 49, 50]. Methods were reported to produce functionalized single graphene sheets in bulk quantities through thermal expansion of graphite oxide. The introduction of oxygen containing functional groups (such as hydroxyl and epoxide) results in an increase in the *d*-spacing of GO as well as a change of hybridization of the oxidized carbon atoms from planar sp^2-hybridation to tetrahedral sp^3-hybridation. In the thermal exfoliation process, the organic functional group is thermally degraded and a volatile gas is generated, creating high pressure between graphene layers that helps graphene layers separate from each other. After the exfoliation process, the thickness of graphene nanoplates can be dramatically reduced down to few atoms.

Another benefit of the process is that the thin 2-D functionalized graphene sheets are easily suspended in water based solutions due to their low density, large surface area and are hydrophilic due to the functional group. This characteristic makes lyotropic process in the study viable. The method offers an easier route to prepare fMGs in high yielding. Functionalization of fMGs sheets hence produced can also be adjusted by treatment in acid, UV-ozone, or reacting with other chemicals. XPS, FTIR, TGA, and Raman tests can be applied to characterize the chemical structure and functionalization of graphene plates. [51, 52, 53]

1.3.5 Sonication/Functionalization

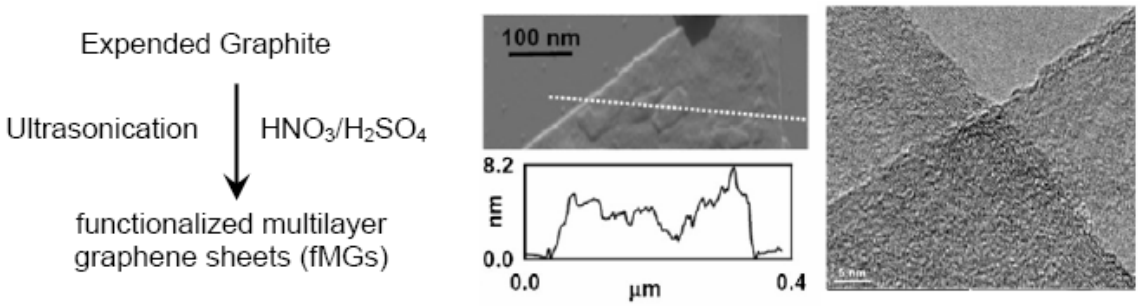

Figure 1.6 Preparation of carbon sheets and characterization of the products. (Veca et al, 2009, [54])

Veca et al in 2009 [54] reported another preparation methodology for functionalized multilayer graphene plates ("carbon nanosheets"). Yields from the method is relatively large, allowing a preparation of epoxy composite with filler loading exceeding 40wt%.

1.3.6 A brief summary and comparison between various preparation methods

As described above, significant variety exists in current preparation of graphene. Generally speaking, graphene from mechanical exfoliation method and epitaxal growth on SiC and metallic substracts has remarkable high quality and low defects level. In contrast, chemically developed graphene usually has relatively high defects level and considerable residual functional groups. It is noticed that graphene from various preparation methodologies show dramatically different 2D peak in Raman spectra, as shown in Figure 1.7. Electrical structure and defects of graphene has significant effect on 2D band (also named as G' band) of graphene Raman spectra [55].

Electrical structure and defects of graphene has significant effect on 2D band (also named as G' band) of graphene Raman spectra. It is indicated that phonon mode of a fine graphene lattice can promote large intensity of 2D band. On the contrary, extreme oxidation of graphite, as an invertible process in chemical development of graphene, can introduce defects in to the fine lattice structure of graphene. Moreover, although the reason for the broad low density 2D peak of chemically reduced graphene oxide remains

ambiguous, oxygen-containing functional groups is believed influential for the electronic structure of graphene. Also, researches indicated that properties (*e.g.* thermal conductivity) of graphene can be dramatically reduced by defects and residual functional groups.

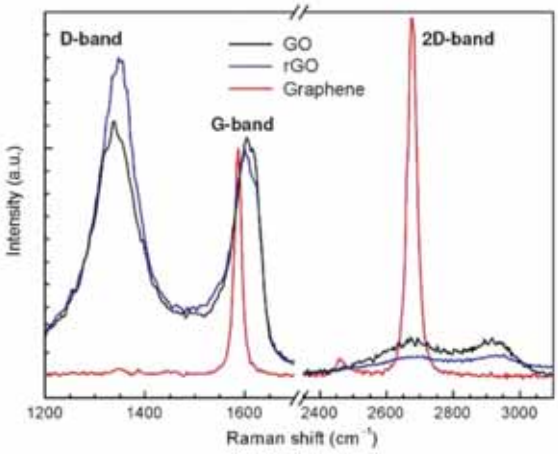

Figure 1.7 Raman spectra of graphene oxide, reduced graphene oxide and pristine graphene, reported by Eda G.et al.(*Adv. Mater.* **2010**, *22*, 2392-415) [55].

Table 1.1 A summary of current preparation methodology of graphene.

Method	*Mechanical Exfoliation*	*Epitaxial growth*	*CVD growth*	*Chemically developement*	*Ultra-Sonication /Functionalization*
Num of Layers	S[a]/F[b]/M[c]	S/F	S/F/M	S/F/M	F/M
Quality	H[d]	H	H	L	M[f]
Defects	L	L	L	H	M
Productivity	L	L[e]	L	H	H
Processability	L	L	L	H	H
Prep. difficulty	H	H	H	M	M
Cost	H	H	H	L	L

[a] Single-layer, [b] Few-layer, [c] Multiple layer, [d] High, [e] Low, [f] Moderate

However, chemical development methodology can produce functionalized graphene plates with high yield conveniently with relatively low cost. This is critically important for many applications of graphene such as electrode of energy collector, fillers in polymer composite, etc. So that, current research pays remarkable attention to them in large-scale material architectures (e.g. graphene oxide paper) from chemical development. In summary, several major preparation method of graphene is compared with quality, productivity, preparation difficulty, cost, etc. in Table 1.1.

1.4 State of the art for current application of graphene

1.4.1 Next generation electronics

Ultra-high mobility of graphene has attracted attentions from both academics and industry in applying graphene as a next generation electronic materials. As an ultra-thin membrane-like semiconductive material, electrical field is much less shielded in graphene compared with most bulky solid materials. Moreover, the two-dimensional structure facilitates patterning and processing of graphene materials on various solid substrates. Therefore, graphene has been applied as blastic field-effect transistors, as show in Figure 1.8 [2].

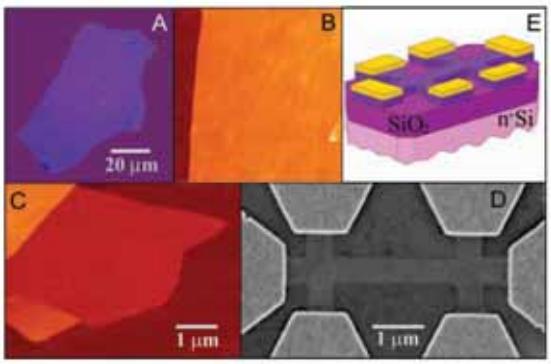

Figure 1.8 Graphene applied as field effect transistors (Novoselov et al. Science 2004 [2]).

Moreover, compared with current essential transparent conductive components of indium tin oxide (ITO), which are expensive and limited in availability, graphene-based transparent conductors are more chemically stable, less influenced by ion diffusion, and

higher transparent in near infrared region. Therefore, graphene can be good transparent electrical conductor with remarkable electrically conductivity, especially after chemical doping, and high transparency, allowing its applications in large scale flexible and stretchable electronic and photonic devices.

Electrical structure of graphene is also highly sensitive to environmental chemical vapors. Moreover, as single-atomic-layer two dimensional nanomaterial, graphene is exposed to environment with maximized surface area, facilitating physical and chemical absorption of various chemical moleculars. Thereby, graphene's electrical conductance is highly sensitive on environmental chemical vapors and can be applied as high-performance chemical sensors.

1.4.2 Electrodes for Energy-storage devices

Due to the ultra-large specific area of graphene (up to 2650 cm^2/g), graphene is promising in electrode of energy collectors. As schematically illustrated in Figure 1.9, an ultra-capacitor is usually operated with di-electronic layers with ultralarge surface area. Theoretically, graphene-based ultracapacitor is expected to have superior capacity up to ~500F/g.

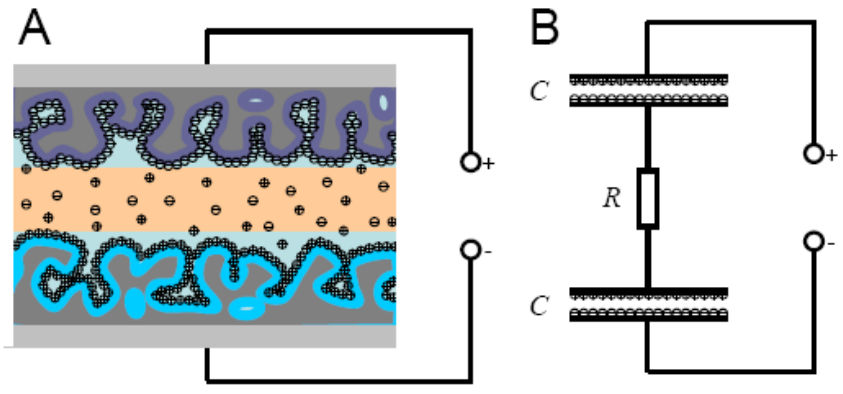

Figure 1.9 Graphene as electrodes of Ultra-capacitors. (A). A schematic illustration of ultra-capacitor. (B). A model in capacitivity calculation.

1.4.3 Fillers in polymer composite

Chemcially developed graphene plates (with various number of layers) has been applied as fillers in polymeric composites [56, 57].

1.4.4 Technical barriers and bottlenecks of application.

The extremely high values of electrical mobility and thermal conductivity of suggest that the graphene can outperform previous material, *e.g.* carbon nanotubes (CNTs) in electronic and heat conduction. However, although early-stage researches showed promising potentials of graphene in various applications, it has been unfortunately limited due to several important drawing-backs, on which more efforts must be addressed. In summery, major problems are described as follows

Limitation in large-volume graphene production

Above all, the relatively low yield of the mechanical exfoliation method can not satisfy the increasing demand of graphene volume in large-scale application such as fillers in polymer composite and electrodes, etc. Graphene hence was one of the most expensive materials in the world before invention of other preparation methodologies (e.g. CVD growth).

Moreover, epitaxal growth of graphene also has significant limitations. It is noticed that current epitaxal growth of graphene highly relies on high temperature. For instance, epitaxal growth of graphene on SiC is operated at 1100°C in vacuum environment. Also, CVD growth of graphene on metallic substrates requires operational temperature higher than 700°C. In contrast, low processing temperature is desired in real electronics devices manufacturing process in order to reduce residual thermal-mechanical stress in processes and protect temperature-sensitive materials such as low-melting-point metallic alloys and polymeric materials.

On the other hand, toxic chemical reduction agents (*e.g.* hydrazine hydrate) and raised temperature are usually necessary in GO reduction, yet not preferred in current

technologies applied in electronic and chemical industry. Therefore, low-temperature, solid-state and clean GO reduction methodologies are desired.

Scarcity of understanding on graphene-based thermal materials

Graphene is a promising candidate for thermal management materials due to its extraordinarily high thermal conductivity (~ 5300W m^{-1} K^{-1} for suspended monolayer grapheneand ~600W m^{-1} K^{-1} for supported monolayer graphene). However, due to experimental difficulties and scarcity of further understanding of graphene's thermal properties, application of graphene as thermal management materials remains challenging.

For instance, previous reported results indicated that vertically aligned CNTs and CNFs can facilitate efficient heat dissipation and electrical conductance in normal direction of solid surfaces, so that is expected to be vertically stacked between/on solid surfaces for their application in thermal interfacial materials (TIMs), electrodes of super-capacitor, *etc*. However, direct growth of vertically aligned free-standing graphene on solid substrate is difficult and rarely available in current studies, bringing significant barriers. Moreover, interaction between graphene and substrates is significantly interested in current research of carbon-based thermal interfacial materials, yet is rarely available and less studied.

Difficulty in mass processing of graphene

Due to it unique two dimensional structure, graphene is actually an anisotropic material. The excellent properties of graphene are limited in in-plane direction along graphene sheets. Therefore, mass processing of graphene plates is important for optimized properties of large-scale material architectures from graphene. For example, large-volume heat dissipation requires a joint contribution of a large number of graphene sheets. Graphene sheets must be aligned in a large scale array in order to meet the requirements for TIM application. Valuable efforts have been paid on preparation of paper-like aligned graphene oxide (GO) and thermally reduced GO. However, in-plane thermal conductivity of GO and reduced GO (1.9 W m^{-1} K^{-1} and 0.14-2.87 W m^{-1} K^{-1},

respectively) is low and unlikely able to meet demanding requirements in thermal management of current photonic and electronic devices.

Moreover, a systematic characterization and fundamental understanding on anisotropy of aligned graphene arrays is desired but not reported yet. In contrast, a huge number of publications have been focused on anisotropy of aligned carbon nano tubes in the past decade, such as coefficient of thermal expansion, electrical and thermal conductivities, and mechanical properties. A study on anisotropy of aligned functionalized multilayer graphene in the research is promising in kindling a new region of research related with graphene, which is comparable with that of aligned carbon nano tubes in history.

1.5 Other nano materials applied in the research

In the study, beside graphene, several other nano materials are also interested and applied in order to handle various requirements of different conductive materials structures. A brief introduction is given as follows:

1.5.1 Carbon nano tubes

Carbon nanotubes (CNTs) can be considered as daughter materials of graphene, which has excellent electrical and thermal conductivities as well as ultrahigh mechanical strength [58, 59, 60, 61]. Here, thermal conductivity enhancement of epoxy composite with carbon nanotubes is especially interested. Moreover, it is noticed that vertically aligned carbon nanotubes were substantially interested as thermal interfacial materials.

Zhu *et al* reported a transfer technology for vertically aligned CNT and applied contact measurement techniques, as illustrated in Figure 1.10 [62]. It is found that and obtained thermal conductivity of vertically aligned CNT array as 81 W m^{-1} K^{-1} and an interfacial thermal resistance of ~ 43 mm^2 K W^{-1} between a vertically aligned CNT array and a copper substrate.

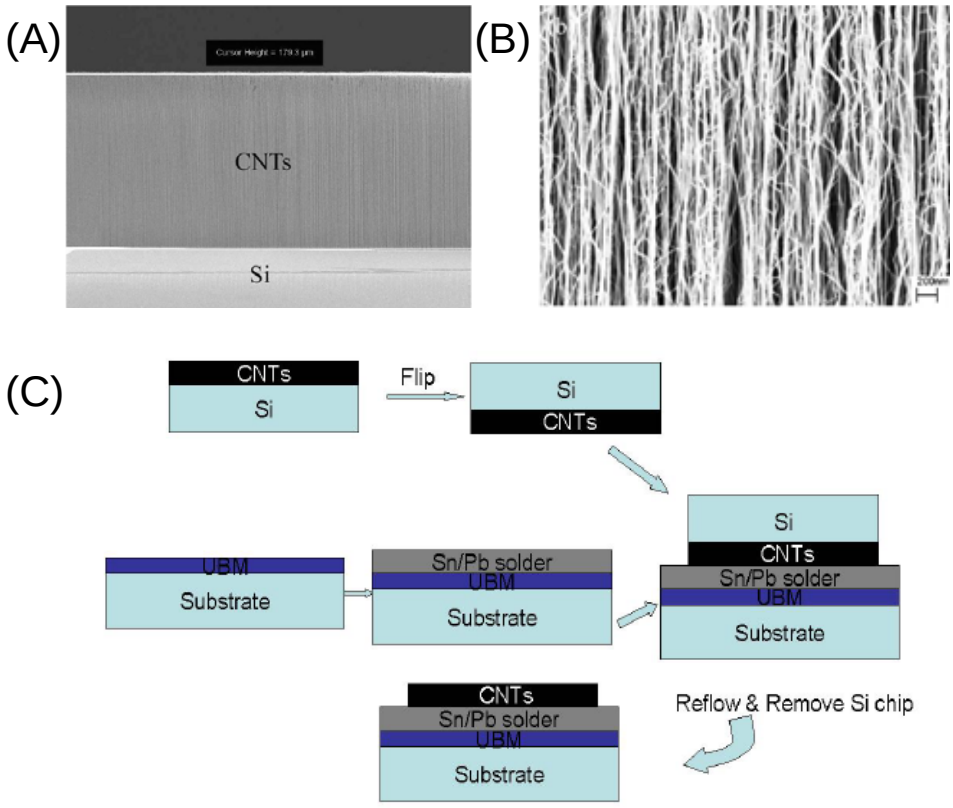

Figure 1.10 SEM images of (a) an aligned CNT film, and (b) individual CNTs at higher magnification. Schematic diagram of the "CNT transfer technology" for assembling aligned open-ended CNT films. (Zhu et al. 2007 [62])

Wang *et al* [63] used a photothermal method and obtained absolute and effective thermal conductivity of a vertically aligned CNT (VACNT) array grown on Si substrate as ~27.3 W m^{-1} K^{-1} and ~0.145 W m^{-1} K^{-1}, respectively, as well as a thermal interfacial resistance of ~16.4 mm^2 K W^{-1} across a CNT/Cr/Si multiple interface. Hu *et al* [64] applied 3-omega measurements on an as-grown VACNT structure at 100kPa pressure, and reported an effective thermal conductivity of the CNTs array and contact thermal resistance between CNTs and Si as ~74 W m^{-1} K^{-1} and ~15 mm^2 K W^{-1}, respectively. Cola *et al* [65] reported that a contact thermal resistance between VACNTs and Si scales ~15.8 mm^2 K W^{-1} by photoacoustic characterization. Lin *et al* [66] applied molecular phonon couplers between VACNTs and Si and reported that an equivalent thermal

conductivity of thus-prepared VACNT TIM structure measured by laser flash method is ~1.6 W m^{-1} K^{-1}. Therefore, VA-fMG TIMs have high thermal conductivity and low contact thermal resistance, suggesting their promising potentials in current demanding thermal management for electronic and photonic devices.

However, the tubic structure of CNTs invertibly introduces high thermal resistance. Therefore, several vertically aligned CNT TIMs architectures are compared with graphene-based TIMs in the research. Moreover, the research is an answer to Dr. R. Prasher's questions in "Graphene spread the heat" (*Science* **2010**, *328*, 185-186.) [67]: "*However, many questions remain. For example, the large thermal contact resistance of carbon nanotubes has severely limited their use as a high-thermal conductivity material. Can graphene overcome this limitation due to its flat structure? Future studies should also investigate what will happen to the in-plane thermal conductivity and contact resistance if the graphene completely conforms to the surface or is embedded in a bulk material, or if the interactions with the substrate are stronger, for example, in contact with metals.*"

1.5.2 Carbon Black

Carbon Black is an electrically-conductive amorphous carbon allotropy which usually prepared from combustion residuals of various nature macromolecular carbon hydrates *e.g.* heavy petroleum components [68]. Although not as large as that of active carbon, specific surface area of carbon black can be considerably large [69]. Thereby, carbon black particles are often graded with specific surface area. Usually, carbon black is applied as pigments, reinforcing additives in rubber tires, *etc* [70].

1.5.3 Thermally conductive ceramic nano particles (h-BN and SiC)

Inorganic/ceramic materials with high thermal conductivity have been used as fillers within the polymer matrix. These candidate fillers include alumina, boron nitride,

diamond, aluminum nitride, silicon carbide and so on. Among these candidates, hexagonal boron nitride (h-BN) and SiC has high in-plane thermal conductivity of up to 300 and 120W/m K, respectively, compared with that (1.4W/m K) of traditionally applied fused silica. Naturally, hexagonal boron nitride (h-BN) and SiC is chosen as high conductive fillers in the research for their promising application in low cost, insolating, and high thermal conductive encapsulators in Cu/low k application, as show in Table 1.2 [71, 72, 73, 74, 75, 76].

Table 1.2. Comparison of filler properties.

Properties	h-BN	SiC	Fused SiO_2
Thermal Conductivity (W/mK @ 25° C)	300+	120	1.4
Dielectric Constant	3.9	6.52-10.3	3.8
Volume Resistivity (ohm-cm)	10^{15}	10^{2}-10^{6}	10^{14}
Loss Tangent @ 1 MHz	<.0002	0.003	.0002
Knoop Hardness kg/mm^2	11	2.25-2.4	500
Coefficient of Thermal Expansion (10^{-6}/ ° C)	<1	4.0	0.5
Specific Heat (J/kgK @ 25° C)	794	750	689
Theoretical Density g/cc	2.25	3.1	2.20

1.6 Research Motivation

1.6.1 Convenient and Green preparation of graphene

Usually prepared by an extreme oxidation of graphite flakes [49], graphene oxide is highly functionalized with decorating polar groups such as carboxyls, hydroxyls, diols, etc, on irregular-sized graphene-like domains [13], which deliver an excellent water solubility of GO. Being water soluble, GO has attractive processability and can be applied as coatings conveniently [19, 20]. However, polar groups on GO inevitably

introduce structural defects on fine pattern of pristine graphene, destroy conjugation among sp^2 hybridized carbon atoms as well as interconnection between of graphene-like domains, and thereby significantly reduce electrical conductance of GO. Removal of polar groups by chemical or thermal reduction can help resurgence of an interconnected graphene structure [55]. After reduction, high electrical conductance and transparency can be obtained, therefore reduced GO (rGO) is noted as a promising candidate for large area transparent conductors [5, 6, 7].

However, toxic chemical reduction agents (*e.g.* hydrazine hydrate) and raised temperature are usually necessary in GO reduction, yet not preferred in current technologies applied in electronic and chemical industry. In real electronics devices manufacturing process, low processing temperature is desired in order to reduce residual thermal-mechanical stress in processes and protect temperature-sensitive materials such as low-melting-point metallic alloys and polymeric materials. For example, melting point of eutectic Sn/Pb alloy scales ~ 183°C. Moreover, polymers materials are often applied in flexible electronic circuits for flexible displaying devices and wearable computer, *etc* [77]. However, thermal stability of most polymer materials is relatively low, forbidding application of high reduction temperatures (up to 400 to 1100ºC) in rGO preparation [5]. Therefore, low-temperature, solid-state and clean GO reduction methodologies are desired.

Microwave (MW) can be efficiently absorbed by carbon allotropes including graphite, carbon nanotubes and fullerenes and cause positive on their physical structures. [78]. MW usually facilities chemical reactions by thermal and non-thermal effects[79]. On the one hand, MW heating can accelerate chemical reactions by reducing activation energy, selectively heat localized domains with different energy converting rate, and improve efficiency of energy usage [80]. These can exercise significant influences in a MW reduction of GO by facilitating resurgence of interconnected graphene domains, and has been applied in solvothermal GO reduction [81]. On the other hand, usually in solid

state, non-thermal MW effects exist and can facilitate diffusion and sintering of solid [82]. As an example, Lin et al (2010) reported a significant defects reduction of carbon nanotubes by MW treatment [83]. However, non-thermal effects of MW are weak in solvents, comparing with that in solid-state. Here, rather than conducting MW reduction of graphene oxide in solution, a novel low-temperature solid-state MW reduction methodology is developed to reduce graphene oxide at ~165±10°C. Significantly reduced sheet resistance as well as high transparency of reduced GO are obtained. This methodology allows GO to be coated conveniently on various substrates and reduced afterwards at low temperature without aid of toxic reduction agents and solvents. The finding can be helpful for an environment-friendly and industry-compatible application of reduced GO as transparent conductors and other applications such as ultra-capacitor, polymer composite, *etc*.

1.6.2 Lyotropic alignment of fMGs

None of the current 1-D and 2-D alignment processes is compatible with current electronic industry processes due to the high temperature (>700^{o}C) and strict requirement in catalyst preparation. In order to overcome the limitation of theses alignment methods such as, high temperatures, time-consuming catalyst preparation, low density, high defect, limited length, and high cost, the proposed research will focus on developing a novel lyotropic method to align ultra thin 2-D layers graphitic structures with high density and for unconstrained profiles. Moreover, the process is also scalable at low temperatures and is a low cost thermal dissipation solution that is compatible to current electronic technology.

A new method to align graphitic ultra thin layers is proposed and named as “lyotropic alignment“. It helps us to obtain highly oriented ultra thin graphite nanoplates with large packing density, in water-based solutions at room temperature. Compared with

the CVD methods applied in growing aligned CNTs and graphene layers, the lyotropic alignment methodology has the following advantages:

1. High thermal conductivity. The thermal conductivity can be calculated from the following equation [84] $k = \alpha \rho C_p$, thermal conductivity k is scaled proportionally with density. The 2D-structured material shows more promise in having higher apparent density (1.6-2.1g/cm^3, 80-100% of intrinsic graphite) and higher thermal conductivity, compared with the low packing density of aligned CNT (5-40% of intrinsic CNT) due to the limitation of CVD.

2. High thermal conductivity in two directions. Although aligned CNTs can drain heat from chip to heat sink (in axle direction), thermal conductivity in the other two dimensions is relatively low. Comparing with the psudo1-D structure of CNTs, well-aligned ultra low 2-D layers can generate high thermal conductivity in two lateral directions. In application such as TIMs, high conductivity in more than one direction is significantly beneficial in reducing the peak temperature of hot spots.

3. Better compatibility with a current industrial process and lower cost. Lyotropic alignment can be operated at low temperatures and does not have any requirement in preparation of catalysts and temperature control, resulting in low cost. Moreover, lyotropic alignment can be applied at large scale and is promising in high yields.

The orientation and anisotropic physical structure can be characterized by SEM, Raman, and contact angle measurements. Moreover, alignment of fMGs can bring anisotropic properties. At least three properties can be applied to confirm the alignment and orientation of aligned fMGs (A-fMGs): Coefficient of thermal expansion (CTE) , electronic conductivity, and thermal conductivity.

1.6.3 Development of approaches for graphene-based thermal management materials

Requirements for thermal dissipation by the semiconductor industry are becoming more demanding. Typically, the power dissipation in electronic devices is proportional to density of the circuit, overall capacitance and resistance, square of power supply voltage, and chip operating frequency [85, 86]: Although use of a lower supply voltage can help to reduce heat generation in operation, there are undeniable trends of increasing chip operating frequency, overall transistor and resistance, transistors number per chip follow Moore's law [87], the total power consumption continues to increase (~up to 200W). More advanced semiconductor devices generally require better heat dissipation.

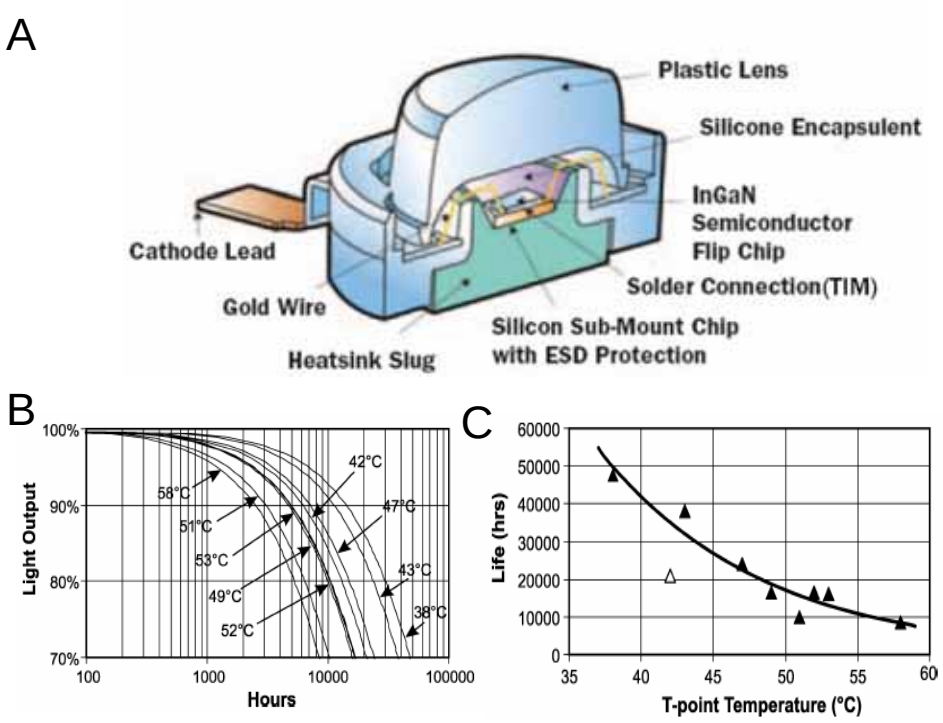

Figure 1.11 An example of TIMs applied in LED. (A). Schematics of heat spreader and heat sink mounted on the backside of LED. (B). Schematic of light output and life from a typical LED device. (C). Schematic of device life as a function of T-point temperature in a typical LED device.[87, 88, 89]

This creates a very challenging situation and necessitates advances in power dissipation technology. It has been observed that a reduction in the operation temperature of a device can correspond to an exponential increase in the performance, reliability, and life expectancy of the device [88, 89, 90], as shown by the schematics of light output and

life from a typical LED device in Figure 1.11. As shown in Figure 1.13, gaps and small voids and can cause high thermal resistances across joint solid surfaces, thereby have become bottle necks in thermal dissipation. Thermal interfacial materials (TIMs) with high thermal conductivity are expected to reduce interface thermal resistance between contacted substrates, as shown by Figure 1.12.

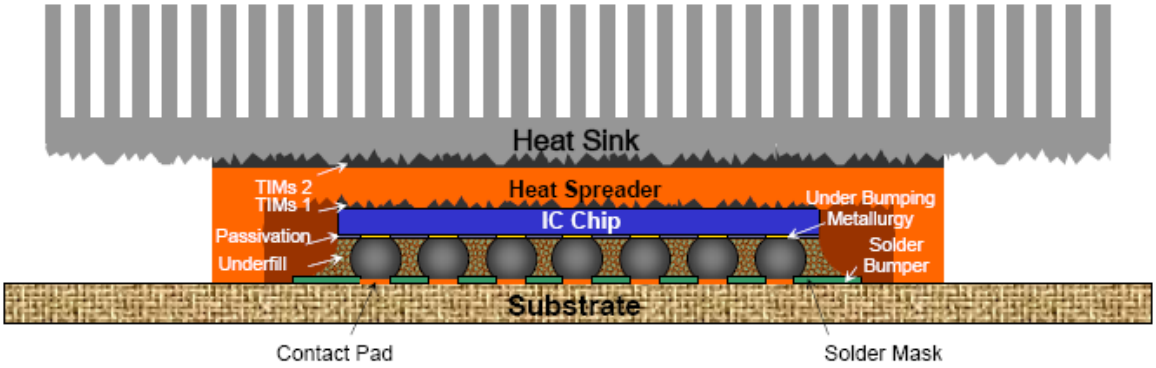

Figure 1.12 A schematic illustration of a typical flip-chip package.

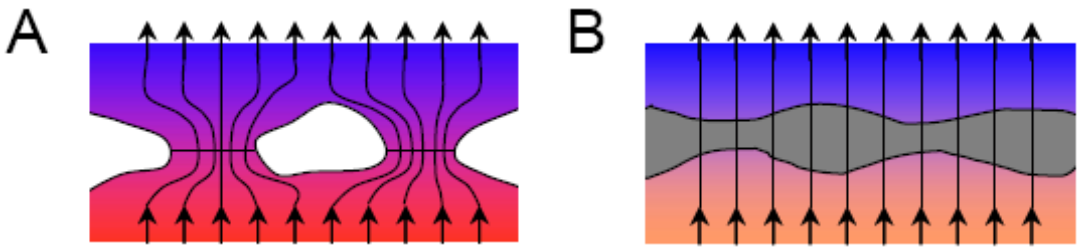

Figure 1.13 Schematics of thermal transportation through interfaces. Left: without TIMs; Right: with TIMs

Anisotropic carbon nono materials, e.g. vertically aligned CNTs arrays, have been highlighted due to their merits in well-oriented structure and high thermal conductivity along the axle direction [91, 92, 93, 94, 95, 96, 97, 98]. However, nowadays vertically aligned carbon nano tubes are grown by chemical vaporization deposit (CVD) methods and have strict requirements in catalyst preparation along with high temperature requirements, which is non-compatible with the current manufacturing technologies and applications in current electronic industry [37, 99, 100]. Furthermore, producing CNTs still yield a low packing density and usually is limited in yielding. All of these challenges

are pushing researchers to develop a new kind of carbon materials, which can be low in cost, convenient in availability and capable of handling large power heat transportation. So that new high conductive materials are desired for TIMs applications.

Graphitic 2-D low dimensional materials have attracted significant attention in mechanical properties, electrical and thermal conductivity [1, 2, 3, 29, 48, 101, 102, 103,]. Previous research indicated that thermal conductivity of single graphene sheet in lateral direction can be as high as 4.84×10^{3} to 5.30×10^{3} $Wm^{-1}K^{-1}$ [1]. However, all the promising potentials of ultra low dimensional 2-D layers are unfortunately limited in in-plane direction of single particle region. Comparing to the phonon transport along chemical bonds in in-plane direction, phonon transfer between the graphene layers is conducted by Van der Waals forces, which are relatively weaker than chemical bonds and can definitely scatter and delay the phonon transfer. Fortunately, as anisotropic thermal conductors, graphene has the potential to be well oriented and aligned. Desired alignment is the orientation of the ultra thin 2-D layers in planes parallel to each other, helping us to optimize the thermal and electronic properties in a desired direction.

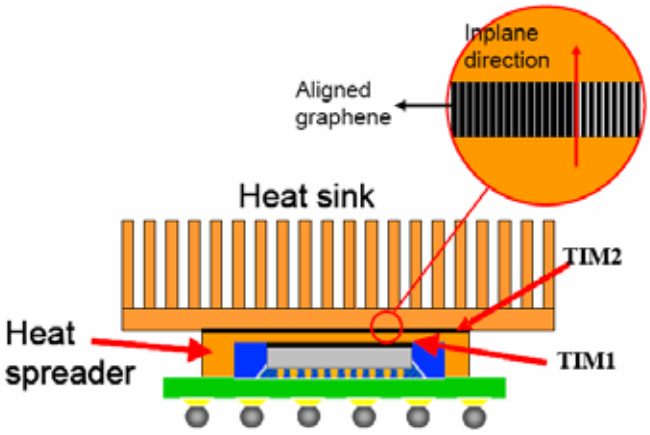

Figure 1.14 Design of A-fMGs for TIM application.

1.6.4 Further understanding of polymer composite conductivity and its application

Previous researches indicated that filler loading, morphology of fillers, and chemical bonding across filler/polymer interfaces have significant influence on

electrical/thermal conductivity of polymer composite, which is important for the application of polymer composites in polymer aging sensors, underfill materials and thermal interfacial materials etc.

First, electrical resistivity of conductive polymer composites (CPCs) is highly sensitive on volume or weight ratio (filler loading) of conductive fillers in polymer matrix, especially when filler loading is close to percolation threshold (p_c). Thermal oxidation aging usually can cause a significant weight loss of polymer matrix in a CPC system, resulting in a filler loading change which can be exhibited by a prompt alteration in electrical resistivity of CPCs. Here, the phenomena are applied as approach for *in-situ* monitoring thermal oxidation status of polymeric materials [144, 145, 146]. It is notice that aging status of polymer materials are difficult to detect and predict, however, very important for the reliability of polymeric insulation systems, which may work in various unforeseen environmental conditions including heat, light and oxygen in motors, aircrafts, and electrical generators. In order to detect ongoing failures for predictive maintains, effective monitoring methods for real-time thermal oxidation aging status of polymeric components are desired and required by standards. In this study, with an original filler loading slight smaller than percolation threshold, CPCs from carbon black (filler) and bis-phenol type epoxy (polymer matrix) are prepared and aged. Carbon black is found to chemically inert and can't be decomposed in the aging condition. In contrast, several degradation mechanisms during the aging processes are accounted for a significant weight loss of bis-phenol type epoxy. Therefore, during aging, filler loading of the carbon black filled epoxy composites is continuously increasing to approach and exceed percolation threshold consequently, resulting in a dramatic change in electrical resistivity.

Second, interfacial issues related to these thermal conductive fillers are systemically studied. On the one hand, the study focuses on relationship between morphology of h-BN particles and thermal conductivity of their epoxy composites. It is

found that spherical-agglomeration of h-BN particles can significantly enhance thermal conductivity of epoxy resin, compared with dispersed h-BN plates, by substantially reducing specific interfacial area between h-BN and epoxy resin. On the other hand, surface pre-treatement / functionalization of inorganic particles can significantly enhance adhesion of cured polymer composites to solid substrates by building solid bonding between particles and polymer matrix, which contribute to reduction of interfacial phonon scattering and thermal resistances across filler/polymer interface. Here, surface of high thermal conductive fillers such as SiC particles and MWNTs are successfully functionalized, which makes their surface reactive with bisphenol A diglycidyl ether and able to form chemical bonding between fillers and epoxy resin. By this means, thermal conductivity of polymer composites is found to be significantly enhanced compared with control samples. The research can benefit a development of high thermal conductive polymer composites by interfacial chemical bonding enhancement to meet the demanding requirements in current fine pitch and Cu/low k technology.

1.7 Brief summary

As described above, the study is focusing on several bottle-necks in the application of graphene as well as several other nanomaterials in electronics and photonics systems. In summary, the study provides:

1. A convenient, clean, and low temperature methodology for GO reduction with high efficiency, which have potentials in broadening the application of reduced GO as transparent electric conductors.
2. To study a novel alignment methodology, “lyotropic alignment”, for mass processing of fMGs at room temperature.
3. An throughout approach for graphene-based TIM assembly.

4. Knowledge of aligned graphene architectures, which may not only facilitate graphene's application in current demanding thermal management but also promote its widespread applications in electrodes of energy storage devices, conductive polymeric composites, etc.
5. A systematic kinetic study for a direct relationship between electrical resistivity of conductive polymer composite and aging conditions for its application in polymer ageing sensor based on conductive polymer composites.
6. A further understanding on influence of filler morphology/shape and surface functionalization on polymer composite thermal conductivity.

CHAPTER 2 PREPARATION AND MICROWAVE REDUCTION OF GRAPHENE OXIDE

Ever since its discovery, graphene has been successfully prepared in various methodologies such as mechanical stretching [5], epitaxal [11] and CVD growth [12], chemical developments [13], *etc*. Among these, preparation of chemically developed functionalized graphene from graphene oxide (GO) has significantly high productivity and low cost, thereby has been extensively interested.

Usually prepared by an extreme oxidation of graphite flakes [49], graphene oxide is highly functionalized with decorating polar groups such as carboxyls, hydroxyls, diols, etc, on irregular-sized graphene-like domains [13], which deliver an excellent water solubility of GO. Being water soluble, GO has attractive processability and can be applied as coatings conveniently [19, 20]. However, polar groups on GO inevitably introduce structural defects on fine pattern of pristine graphene, destroy conjugation among sp^2 hybridized carbon atoms as well as interconnection between of graphene-like domains, and thereby significantly reduce electrical conductance of GO. Removal of polar groups by chemical or thermal reduction can help resurgence of an interconnected graphene structure [55]. After reduction, high electrical conductance and transparency can be obtained, therefore reduced GO (rGO) is noted as a promising candidate for large area transparent conductors [5, 6, 7].

Compared with current essential transparent conductive components of indium tin oxide (ITO), which are expensive and limited in availability, graphene-based transparent conductors are more chemically stable, less influenced by ion diffusion, and higher transparent in near infrared region. However, toxic chemical reduction agents (*e.g.* hydrazine hydrate) and raised temperature are usually necessary in GO reduction, yet not preferred in current technologies applied in electronic and chemical industry. In real electronics devices manufacturing process, low processing temperature is desired in order

to reduce residual thermal-mechanical stress in processes and protect temperature-sensitive materials such as low-melting-point metallic alloys and polymeric materials. For example, melting point of eutectic Sn/Pb alloy scales ~ 183°C. Moreover, polymers materials are often applied in flexible electronic circuits for flexible displaying devices and wearable computer, *etc* [77]. However, thermal stability of most polymer materials is relatively low, forbidding application of high reduction temperatures (up to 400 to 1100ºC) in rGO preparation [5]. Therefore, low-temperature, solid-state and clean GO reduction methodologies are desired.

Microwave (MW) can be efficiently absorbed by carbon allotropes including graphite, carbon nanotubes and fullerenes and cause positive on their physical structures. [78, 104]. MW usually facilities chemical reactions by thermal and non-thermal effects [79]. On the one hand, MW heating can accelerate chemical reactions by reducing activation energy, selectively heat localized domains with different energy converting rate, and improve efficiency of energy usage [80, 105]. These can exercise significant influences in a MW reduction of GO by facilitating resurgence of interconnected graphene domains, and has been applied in solvothermal GO reduction [81]. On the other hand, usually in solid state, non-thermal MW effects exist and can facilitate diffusion and sintering of solid [82]. As an example, Lin et al (2010) reported a significant defects reduction of carbon nanotubes by MW treatment [83]. However, non-thermal effects of MW are weak in solvents, comparing with that in solid-state [106]. Here, rather than conducting MW reduction of graphene oxide in solution, a novel low-temperature solid-state MW reduction methodology is developed to reduce graphene oxide at ~165±10°C. Significantly reduced sheet resistance as well as high transparency of reduced GO are obtained. This methodology allows GO to be coated conveniently on various substrates and reduced afterwards at low temperature without aid of toxic reduction agents and solvents. The finding can be helpful for an environment-friendly and industry-compatible

application of reduced GO as transparent conductors and other applications such as ultra-capacitor, polymer composite, *etc*.

2.1 Experimental

2.1.1 Preparation of GO

In the study, GOs are prepared by a modified Humman's method. GO is prepared by reacting with a mixture of $KMnO_4$ and concentrated (98%) H_2SO_4. 0.1g graphite flake (Asbury 3775) is mixed with 100ml concentrated H_2SO_4 in a single-neck glass flask equipped with a cooling condenser and sonicated in water bath for 2 hours at room temperature. Subsequently, 0.5g $KMnO_4$ is added in to the reaction system and the reaction system is sonicated at room temperature for another 5 min. The reaction system is heated to 60°C in oil bath and stirred for 1 hour with a magnetic stirrer. After cooling down to room temperature, the reaction system is stopped by pouring into a mixture of 10 ml 30% H_2O_2 with 500 g ice, sealed, and set at room temperature for 12 hours. Thus-prepared GO are washed by diluting in fresh DI water and condensing with a centrifugor (at 5000 rpm) alternatively.

2.1.2 Microwave Reduction

A variable frequency microwave system (VFM, Microcure 2100 by Lambda Technologies) equipped with an infrared wave temperature sensor is applied in MW reduction. MW frequency is 6.425 GHz with a band width of 1.15 GHz and a sweeping rate of 0.1 second. The power of the MW is controlled at 500 W and substrate temperature is controlled and stabilized at 155-175°C, with aid of an infrared thermometer and a feedback controlling unit, as shown by Figure 2.1.

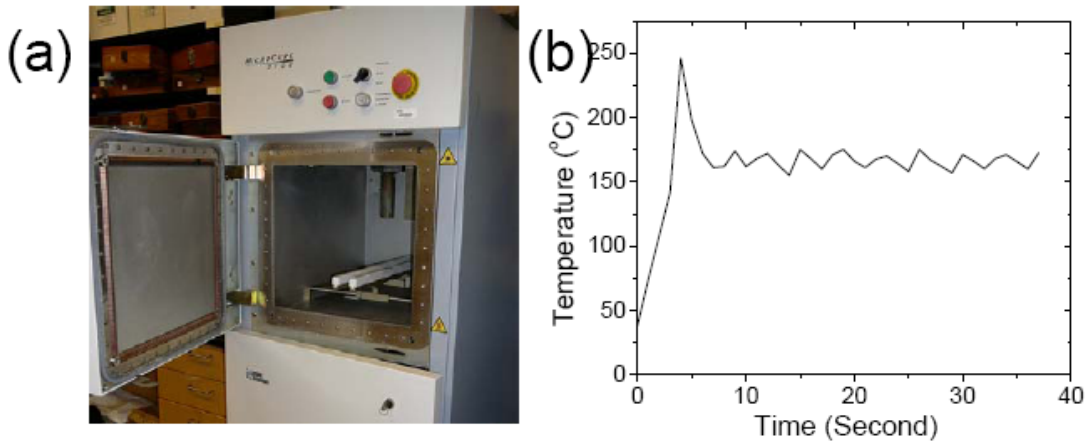

Figure 2.1 Experimental condition of microwave reduction. (a), Variable frequency microwave system applied in the work. (b), Controlled surface temperature on the Si/SO_2 substrates in the reduction process.

2.1.3 Sheet electrical resistance measurement

Electrodes composed with a layer of gold (~150nm) above 100nm thick titanium are prepared by photo lithography method on a silicon wafer with 250nm SiO_2 coating. GO is dispersed in water, deposited between electrodes, as shown by the optical image shown in Figure 2.8, and dried in a convection oven at 60ºC for 3 hours. Subsequently, GO coated on a Si/SiO_2 substrate is reduced by MW with a controlled surface temperature (~165°C) of SiO2 coated Si substrate as described above. Current-Voltage curves of MW reduced GO are obtained by a Keithley 485 Autoranging Picoammeter equipped with a HP 6353A DC power supply. Electrical resistance (R) is obtained according Ohm's law by considering current-voltage curves to be linear. Sheet resistance of MW reduced GO is calculated according to an equation as follows:

$$R_s = R\frac{W}{L}$$

Equation 2.1

2.1.4 Other characterization

Fourier-Transform Infrared (FTIR) spectra reported here are collected by a FTIR spectrometer (Nicolet, Magna IR 560) with a transmission mode with a wave number

range from 500 to 4000 cm^{-1}. A X-ray photoelectron spectroscopy (XPS) (Model 1600, by Physical Electronics) equipped with a Al K_α X-ray source (1486.8 eV) is applied in obtaining XPS scanning and high-resolution spectra with an operational vacuums pressure lower than 7×10^{-9} torr. Raman spectra of GO and MW reduced GO are taken by a Lab Aram Raman spectrometer (by Horiba Jobin Yvon) with a 532nm laser source and a 100X objective lan (MPlanN, by Olympus). A thermo gravimetric Analyzer (TGA) (Model 2050, by TA Instruments) is used to characterize weigh loss behavior of GO and MW reduced GO specimens with a temperature raising rate of 20°C/min.

2.2 Graphene oxide thickness characterization

Here, GO is prepared by a modified Hummer's method as detailed in experimental section. Briefly, graphite flakes are oxidized by a mixture of $KMnO_4$ and concentrated sulfuric acid. GO prepared by this method has ultra-smooth nature and low thickness.

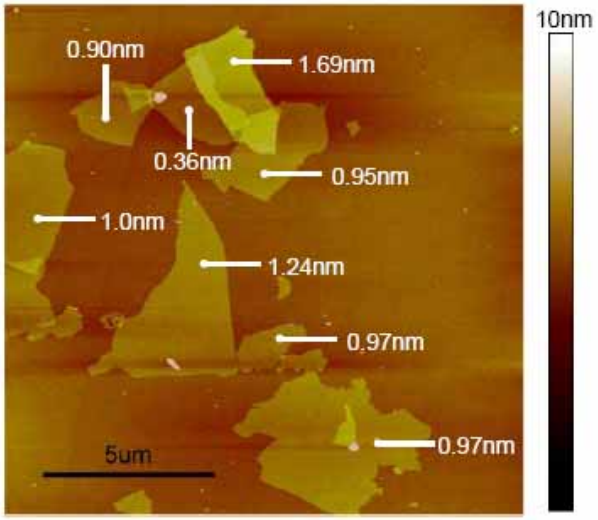

Figure 2.2 AFM image of graphene oxides applied in the research.

As shown by Figure 2.2, an AFM height image indicates the thickness of the GO sheets ranges from 0.36 nm to 1.69 nm, corresponding to 1 to 5 atomic graphene layers.Thus-prepared GO is well dispersed in water, drop-coated on a silica (250nm) coated silicon wafer and consequently dried under a relatively low temperature (60°C)

and reduced by MW at a well-controlled temperature (~165±10°C), as described in experimental.

2.3 Deoxygenation of GO by Microwave

It is noticed that removal of oxygen containing functional groups such as carboxyls, hydroxyls and carbonyls is essential in GO's reduction. In previously reported thermal and chemical reduction methodologies of GO, concentration of functionalized groups as well as oxygen atoms on GO is reduced. So that GO reduction can be concluded as a "deoxygenating" process of GO chemical structure. Here, deoxygenation of GO in the microwave-induced reduction process is systematically studied with aid of a Fourier-Transform Infrared (FTIR) spectrometer and an X-ray photoelectron spectroscopy (XPS).

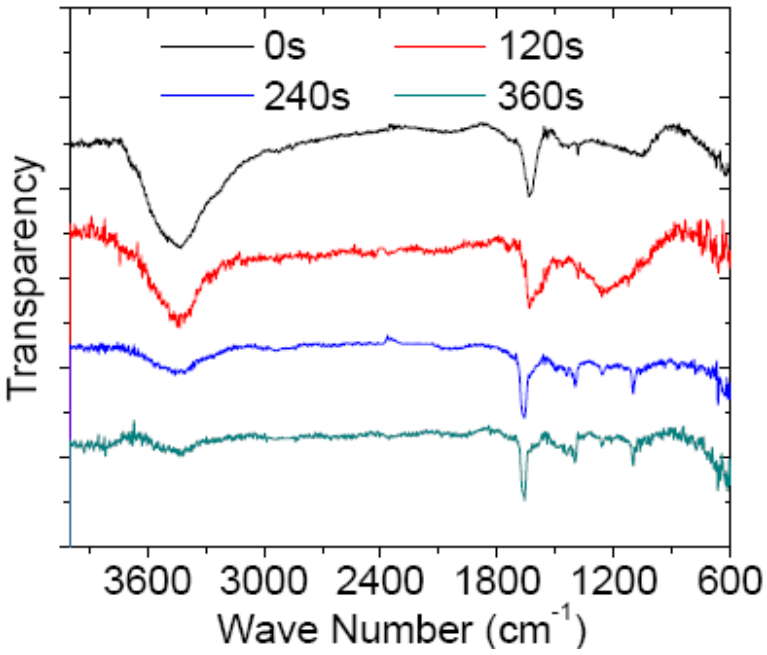

Figure 2.3 FTIR spectra of reduced graphene oxides.

FTIR spectra in Figure 2.3 shows that a broad intensive peak around ~3450 cm^{-1} of as-prepared GO, which is corresponding to high concentration of hydroxyl and carboxyl groups on GO, fades out as reduction time increases, and almost disappears

after 360 seconds, indicating decomposition of oxygen-containing groups on GO and a significant reduction of oxygen atom concentration.

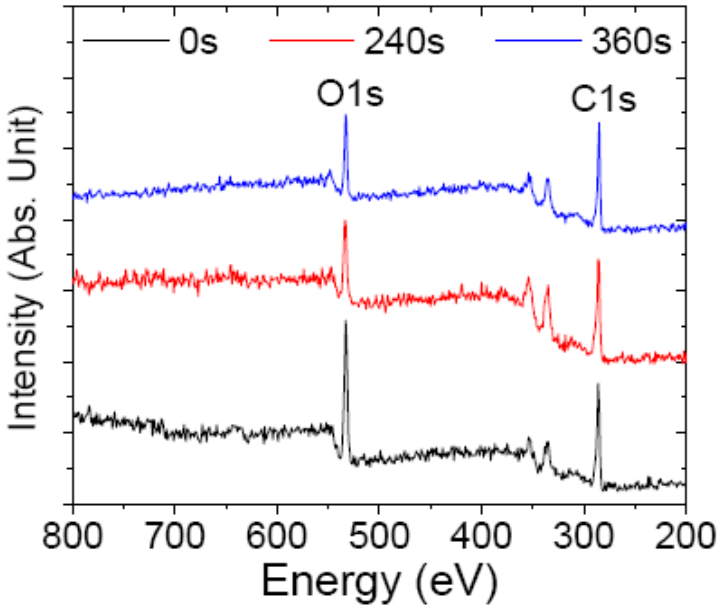

Figure 2.4 XPS spectra of reduced graphene oxides.

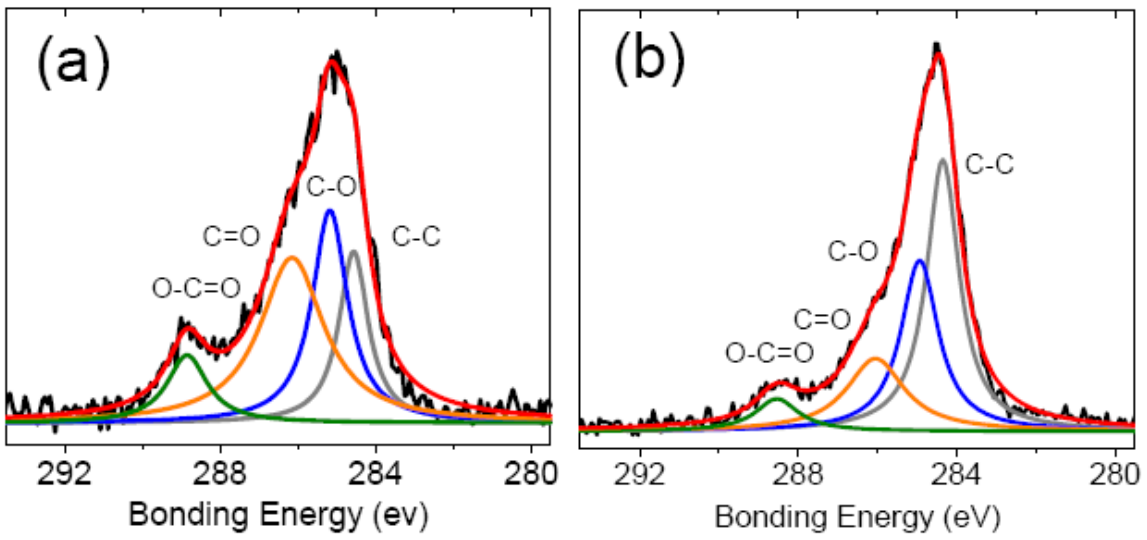

Figure 2.5 Functional group distribution analysis of reduced graphene oxide. (a), High resolution XPS spectrum of pristine graphene oxide; (b), High resolution XPS spectra of reduced graphene oxide in MW for 360 seconds.

Low-resolution scanning X-ray Photoelectron Spectra (XPS) in Figure 2.4 confirm efficient deoxygenating of GO by giving reduced ratio between integrated area of O1s and C1s peaks after MW reduction. Empirical atomic sensitivity factor of C1s and

O1s peaks is traditionally considered as 0.25 and 0.66 [27], respectively. According to an empirical equation for atom concentration calculation based on XPS spectra [10, 28], concentration of O atoms on GO and MW reduced GO can be expressed by an equation as follows.

$$C_{Oxygen} = \frac{\frac{P_{O1s}}{S_{O1s}}}{\frac{P_{O1s}}{S_{O1s}} + \frac{P_{C1s}}{S_{C1s}}} \times 100\% \qquad \textbf{Equation 2.2}$$

Where C_{Oxygen}, P_{O1s}, P_{C1s}, S_{O1s}, *and* S_{C1s} present oxygen concentration on GO, integrated area of O1s peak, integrated area of C1s peak, empirical atomic sensitivity factor (0.25) of C1s and empirical atomic sensitivity factor (0.66) of O1s peaks, respectively.

Table 2.1 A data list for oxygen concentration and functional group distribution calculation based on XPS spetra.

Sample	Low Res. XPS Scanning		High Res. XPS of C1s peak			
			Functional group distribution (%)			
	P_{O1s}/P_{C1s}	C_{Oxygen}(%)	C-C	C-O	C=O	O-C=O
GO	1.385	34.4	20.0	30.3	40.9	8.8
rGO (240s)	0.886	25.1	38.7	29.6	25.4	6.3
rGO (360s)	0.738	21.8	44.6	30.8	19.0	5.6

As shown by Table 2.1, ratio between integrated area of O_{1s} peaks and C_{1s} peaks in XPS of GO can be reduced from 1.385 for as-prepared GO to 0.886 for MW reduced GO (after 240 seconds) and 0.738 for MW reduced GO (after 360 seconds), corresponding to oxygen concentration of 34.4%, 25.1% and 21.8%, respectively. High-resolution X-ray Photoelectron Spectra (XPS) of MW reduced GO also evidence a significant deoxygenation of GO under MW by measuring functional group distribution based on C1s peak. As shown by Figure 2.5, after exposure under MW for 360 second,

reduced GO show a ratio of 44.6:30.8:19.0:5.6 among C-C (bonding energy=284.4eV), C-O (285.1 eV) and C=O (286.1eV), O-C=O (288.7eV) compared with that (20.0:30.3:40.9:8.8) of as-prepared GO (before MW reduction).

2.4 Defect Level Reduction

Reduced concentration of oxygen atoms on GO is essential in GO reduction, however, defect level of rGO is also important for recovery of fine graphene lattice structure, which significantly contribute to conductive chemical structure from conjugated sp^2 carbon atoms. Raman spectroscopy has been widely accepted as an efficient method to evaluate defect level of carbon nanomaterials [29, 30]. Usually, a lower D/G band intensity ratio in a Raman spectrum is an index of fewer defects on graphitic structures.

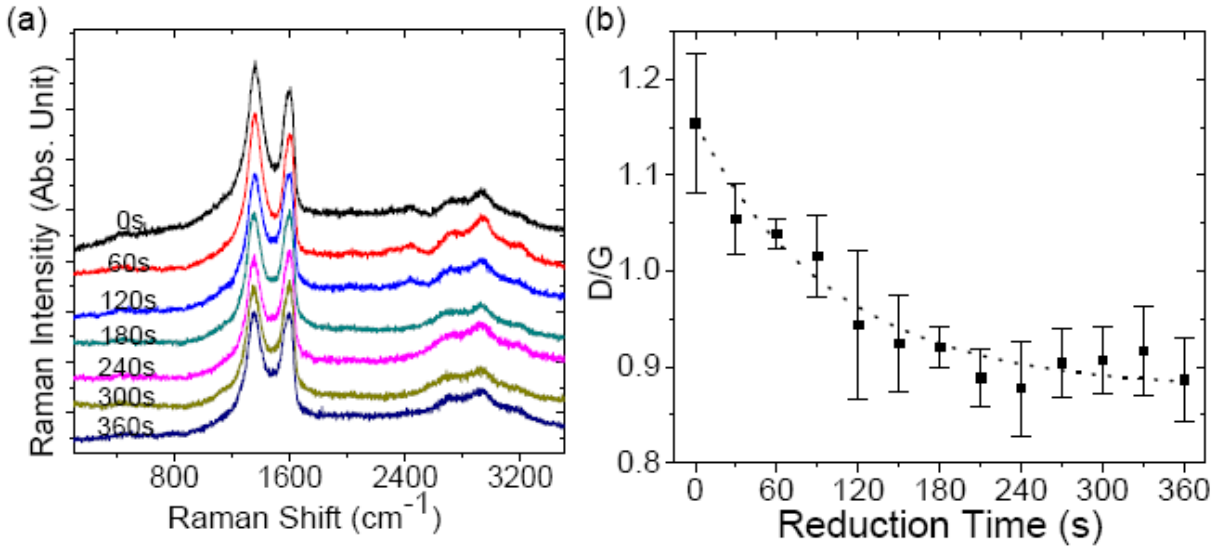

Figure 2.6 Defect level characterization based on Raman Spectra. (a), Raman spectra of reduced GO; (b), Raman intensity ratio of D and G bands of reduced graphene oxide as a function of reduction time.

In our study, as can be seen from Figure 2.6, D/G intensity ratios of MW reduced GO are measured and plotted as a function of reduction time. As MW reduction time increases, D/G ratio in Raman spectra is decreased smoothly from 1.16 (before reduction)

to 0.87 (reduced in VFM for 360s), indicating a decreased defect concentration on MW reduced GO and a recovery of graphene lattice structure from sp^2 carbon bonds. Moreover, significantly increased thermal stability shown by thermal gravimetric analysis (TGA) measurement in Figure 2.7 also suggests the successful removal of decorating groups as well as a reduced level of defects on the GO sheets. The onset point ($T_{d,onset}$) of thermal degradation of materials obtained from TGA measurement is usually considered as index of thermal stability of their chemical structures. Comparing as-prepared GO ($T_{d,onset}$ =184°C), GO reduced by MW at solid state here show significantly increased $T_{d,onset}$ (629°C after 240 second and 686°C after 360 seconds, respectively), indicating a successful re-construction of a fine network from conjugated sp^2 carbon atoms, which has lower defects level and higher thermal stability.

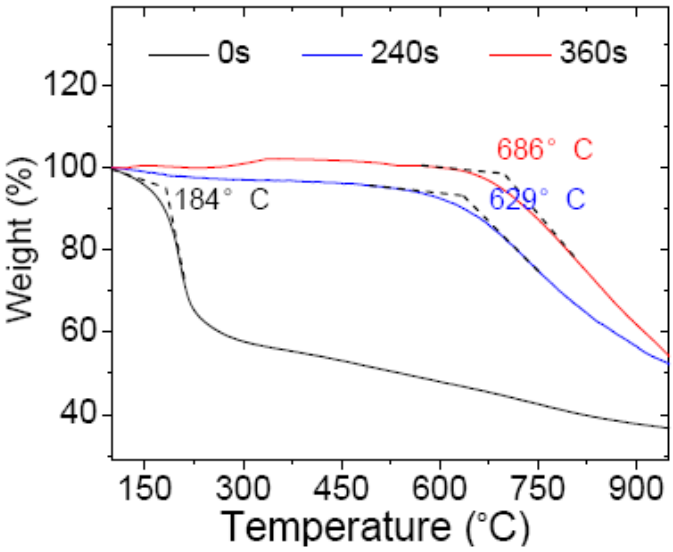

Figure 2.7 Thermogravimetric Analysis of reduced graphene oxide.

2.5 Transparency

In order to study the electronic conductance as well as optical transparency of MW reduced GO, gold electrodes are prepared by photo lithography method on a silicon wafer with 250nm SiO_2 coating. GO is deposited between electrodes as shown by the optical image shown in Figure 2.8. After drying in a vacuum oven at 60ºC for 3 hours,

GO coated on a Si/SiO_2 substrate is reduced by MW with a controlled surface temperature (~165°C) of SiO_2 coated Si substrate. Transparency of the MW reduced GO sample is measured by a reflection mode on a Raman spectrometer with 532nm laser. Raman intensity of Si substrate coated with SiO_2 (as represented by blue cycle inset in Figure 2.8A) and reduced GO on Si/SiO_2 substrate (as represented by red cycle inset in Figure 2.8A) are measured, as shown by Figure 2.8B. SiO_2 coated Si substrate is responsible for peaks at $523cm^{-1}$ Raman shift (corresponding to 547nm in a Raman spectrometry system with 532nm laser).

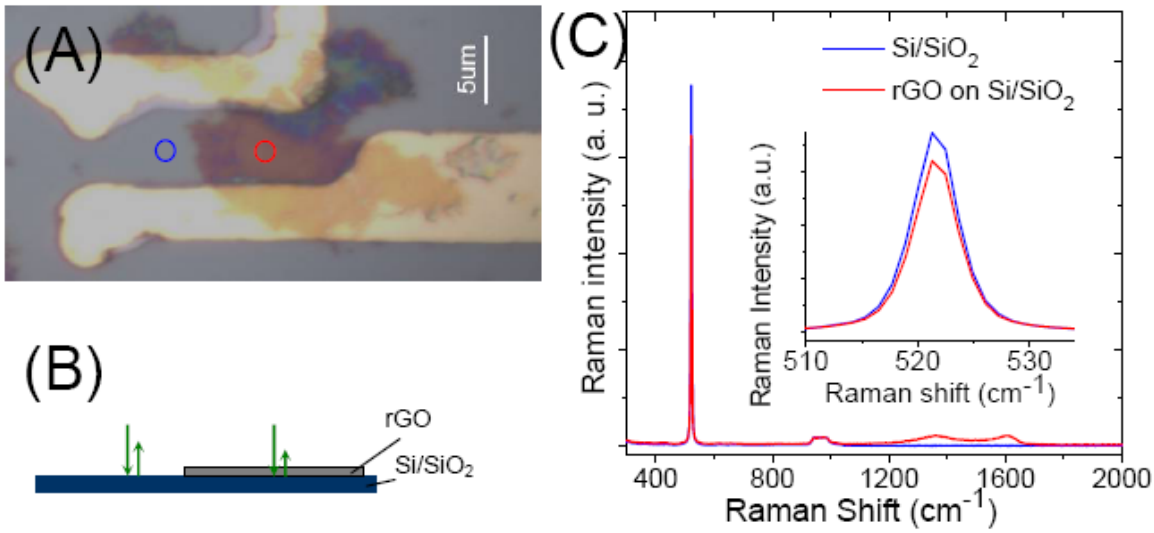

Figure 2.8 Electrode pattern in transparency and electrical resistance measurement. (A), An optical image of graphene oxide deposited between electrodes, with inset cycles representing the domains tested by Raman for transparency calculating; (B), a schematic illustration of transparency measurement; (C), Raman spectra of 250nm SiO_2 coated Si substrate and reduced GO on the SiO_2 coated Si substrate. Inset is the specific Raman intensity around ~$523cm^{-1}$ and a schematic illustration of transparency measurement.

In Raman tests of reduced GO on the Si/SiO_2 substrate, incidental laser passes through the MW reduced GO twice before being detected, as shown by inset of Figure 2.8C, which can cause inevitable decrease of measured Raman intensity at $523cm^{-1}$ (547nm). The Raman spectra indicate that the Raman intensity at $523cm^{-1}$ (547nm) of MW reduced GO sample is diminished by 14%, which is attributed to 92.7% transparency of the MW reduced GO according to Beer-Lambert Law.

$$A = \log_{10}\left(\frac{1}{T}\right) = \alpha' l$$

Equation 2.3

Where A, T, α', and l represent absorption, transparency, and absorption coefficient, and rGO thickness.

2.6 Electrical Conductivity

Recovery of hexagon-like conjugated sp^2 carbon structures and low defect level facilitates electrical conductivity improvement of rGO. Current-Voltage curves of the reduced GO sample are obtained by a Keithley 485 Autoranging Picoammeter equipped with a HP 6353A DC power supply. Sheet resistance of reduced GO is calculated according to the Current-Voltage curves and plotted as a function of reduction time with, as shown in Figure 2.9A. Error bars are applied to describe deflections of sheet resistance due to shape irregularity of GO. A linear shape of the current-voltage curve of the MW reduced GO sample showed a metallic nature and Ohmic contact between it and the electrodes.

Confirming reported ultrahigh electrical resistance, it is found that sheet resistance of GO before reduction is as high as ~1×10^{11}Ω/square, which is almost out of the range of the applied instruments. In contrast, sheet resistance of MW reduced GO is significantly decreased as reduction time increases. As can be seen from Figure 2.9B, sheet resistance of the MW reduced individual GO sheet levels off at ~7.9×10^{4}Ω/square after ~240 seconds.

Comparing with reported values of hydrazine reduced GO (~1×10^{8}Ω/square, with transparency of 90% at 550nm) and hydrazine reduced GO with thermal reduction at 400°C (~1×10^{5}Ω/square, with transparency of 90% at 550nm) by Becerril et al [5], the individual MW reduced GO specimen shows comparable conductivity with an optical transparency of 92.7% at similar frequency after 360 seconds in MW reduction. However, a much lower temperature (~165±10°C) is applied, indicating ultrahigh

efficiency of MW in GO's deoxygenation and resurgence of interconnected graphene-like domains.

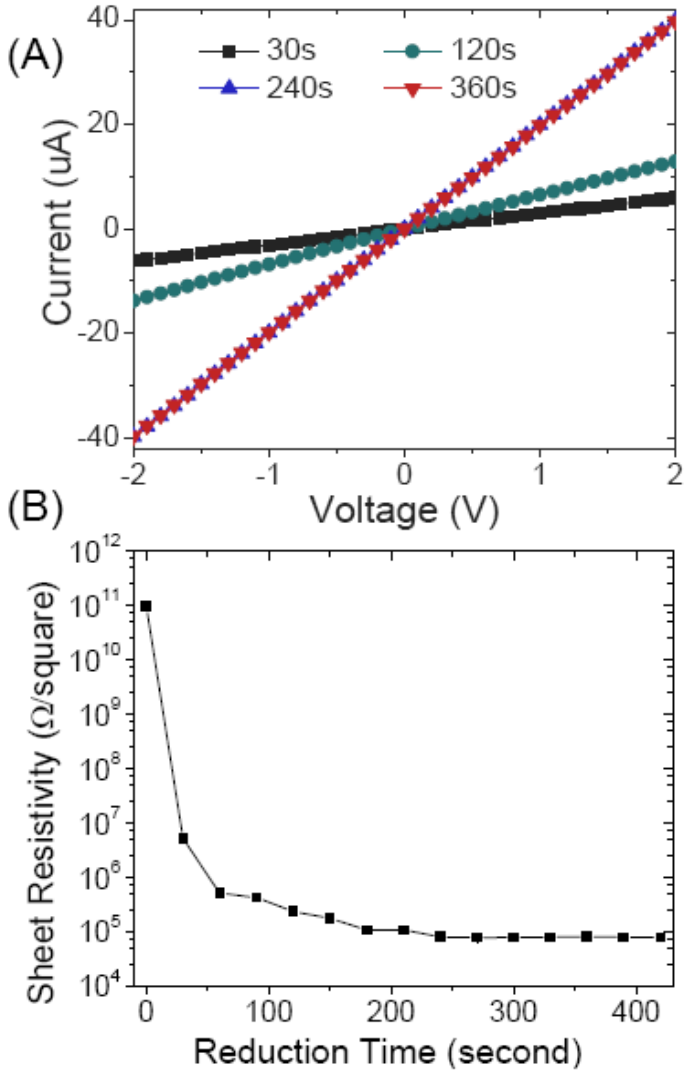

Figure 2.9 Sheet electrical resistance of MW reduced GO. (A), Current-Voltage curves of reduced graphene oxides; (B), Sheet resistance of reduced graphene oxide.

Although the influence of microwave on carbon nanomaterials remain ambiguous, a remarkably strong influence of MW on polar groups on GO should be responsible for the high efficiency. Both thermal and non-thermal microwave effects may account for the high efficiency of microwave reduction found in our research. First, selective microwave heating of decorating groups is possible due to their polar nature in structure. Second, enhanced non-thermal effects in solid-state MW reduction can facilitate sintering of GO

and resurgence of interconnected graphene domains by increasing the diffusion in GO and reducing defects by fast re-arrange defective domains on GO into cyclohexene structures.

2.7 Conclusion

In summary, GO reduction by MW was studied and provides a relatively lower temperature process without aid of chemical agents. FTIR, XPS and Raman tests indicate the high efficiency of deoxygenation and removal of decorating groups on GO. Electrical and optical measurements suggest the resurgence of interconnected graphene-like domains by showing attractively low sheet resistance of the reduced graphene oxide sample with high transparency. The finding provides a convenient methodology for GO reduction with high efficiency, which have potentials in broadening the application of reduced GO as transparent electric conductors.

CHAPTER 3 PREPARATION AND ANISOTROPY OF LARGE-SCALE LYOTROPICALLY ALIGNED MULTILAYER GRAPHENE

Graphene is an anisotropic material noted as a "building material" for other carbon allotropies such as fullerenes, carbon nanotubes, and graphite [1]. Comparing with ballistic electron and phonon transport along graphene sheets, phonon and electron transferring traversing stacked graphene layers are conducted by Van der Waals forces and hopping conduction, which are much weaker and inevitably debate mechanical, electrical and thermal properties in "out-of-plane" direction [27, 28, 107 , 108]. Alignment of graphene sheets can orient covalent chemical bonds in these parallel planes, resulting in a strong anisotropy of the large-scale materials from various graphitic forms with optimized mechanical, electrical and thermal properties. As an example, graphene oxide papers prepared by filtration of water-based solutions have shown excellent mechanical properties due to their highly oriented structures [56, 109]. However, chemical or electrical reduction of graphene oxide is mandatory for high electrical and thermal conductivities. Moreover, systematic characterizations of the anisotropy of the ordered structures are rarely available due to their low profile in thickness directions. Further understanding on anisotropy of aligned graphene layers is critical and currently desired for synthesis and assembly of all graphitic forms.

Here, conductors with highly ordered lamellar structure in large scale are prepared at room temperature from functionalized multilayer graphene (fMGs) by a lyotropical alignment methodology. Distinct difference in mechanical, electronic and thermal properties between lateral (in-plane) and thickness (out-of-plane) directions of the aligned fMGs indicates a strong anisotropy. Benefiting from the anisotropy, ultrahigh electrical and thermal conductivities (~386 S/cm and ~120W/m·K, respectively) in lateral direction are obtained, without aid of any chemical or thermal reduction. The finding facilitates the

potential large-scale preparation and application of multilayer graphenes in photonic and electronic components [7], electrodes for energy collectors [4,110], conductive polymeric adhesives and composites [56].

3.1 Experimental

3.1.1 Preparation of fMGs

fMGs are synthesized according to a method reported by Veca *et al* [54] . 1 g of expanded graphite (Asbury Carbons, grade 3775) is mixed with 160ml ethanol and 100ml DI water. The mixture is sonicated for 24hours, vacuum filtrated with a nylon filtration paper (Magna, 47mm in diameter, 0.1micron pore size), and dried. The sample is then dispersed in a mixture of sulfuric and nitric acid (3:1v/v ratio, 100ml) and sonicated for 36hours. The reaction is stopped by 1L DI water. The mixture is concentrated with centrifugor (IEC Multi, Thermal Electron Co.) at 3000rpm. Solid on the bottom of centrifuge tubes are removed. Supernatant is kept for alignment procedure.

3.1.2 Alignment

0.8g of thus-prepared fMGs is dispersed in 1 L deionized water and vacuum-filtrated with a 47 mm vacuum filtration system equipped with an anodic aluminum oxide (AAO) filtration paper (0.1 micron pore size, Anodisc 47, Whatman International Ltd.). The obtained filtration cake is carefully washed by DI water, removed from filtration paper, and dried at 105ºC for 3 hours.

3.1.3 Polarized Raman Spectroscopy.

A HoloLab series 5000 modular Raman spectroscope (Kaiser Optical Systems Inc) equipped with 785nm (1.58eV) laser is applied. In the tests, polarization of the incident light is fixed. As shown by Figure 3.10, a rotatable stage is set perpendicular to the incidental light. An aligned functionalized multilayer graphene (A-fMG) sample is

vertically stood on the stage in a way that the stage is perpendicular to the planes in which fMGs are aligned. In order to detect the backscattering light intensity, a polarized analyzer is set in directions parallel or perpendicular to the polarization of the incident light, which are named as "*VV*" and "*VH*" configurations, where the letters "*V*" and "*H*" represent "vertical" and "horizontal", respectively.

3.1.4 Electrical conductivity measurement

The current-voltage response of the a A-fMG sample was measured on a Keithley 2000 multi-meter equipped with a 2-point probe testing stage: in lateral direction, with a sample size of 1.10mm × 2.04mm× 6.84mm (width × thickness × length); in thickness direction, with a sample size of 3.30mm × 2.08 mm×0.52mm (width × thickness × length). Electrical conductivities are calculated from resistances and dimensions.

3.1.5 Thermal conductivity measurement

Values of thermal conductivities are calculated from the equation: $k=\alpha\rho C_p$, where k, α, ρ, and C_p reprensent thermal conductivity, thermal diffusivity, material density, and the heat capacity. Anisotropic thermal diffusivities of the A-fMG sample are measured by a Light Flash Apparatus (LFA 447 NanoFlash, Netzsch Thermal Analysis). Density of the A-fMG samples is calculated from the weight and dimension of the sample. Heat capacitor of A-fMGs samples tested by a differential scanning calorimeter (TA Instruments, 2920) with a temperature raising rate of 5ºC/min from room temperature to 150ºC.

3.1.6 Coefficient of thermal expension measurement

In-plane ($\alpha_{//}$) and cross-plane ($\alpha_{\perp}$) coefficient of thermal expansion (CTE) of A-fMGs are tested by a thermo-mechanical Analyzer (TA Instruments, 2940) with a temperature raising rate of 5ºC min^{-1} from room temperature to 250ºC and a force of 0.1

Newton. A software (TA instrument Advantage 2004) is applied to estimate CTE of A-fMGs with following equation:

$$\alpha = \frac{1}{L}\frac{\partial L}{\partial T} \qquad \textbf{Equation 3.1}$$

where L and T represent dimension and temperature. In the test, as shown by Figure 3.1, A-fMG samples are set vertically or recumbently on a quartz stage, corresponding to their in-plane ($\alpha_{//}$) and cross-plane ($\alpha_{\perp}$) coefficient of thermal expansion (CTE), respectively.

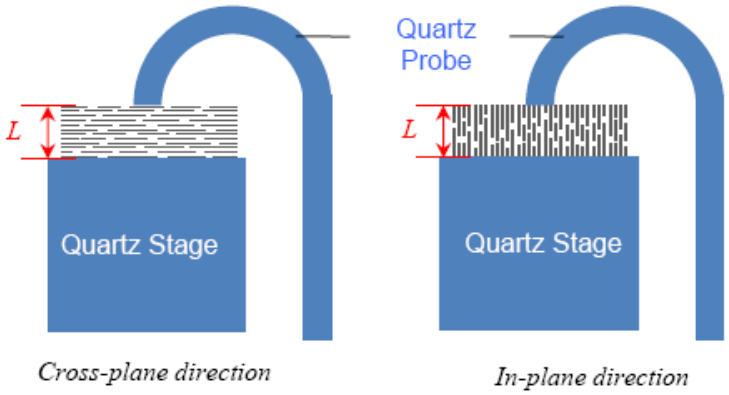

Figure 3.1 A schematic illustration of CTE estimation.

3.2 Preparation and characterization of functionalized multilayer graphene (fMG)

Preparation of paper-like aligned GO by water-filtration method exists . Usually prepared by extreme oxidation of graphite, GO is highly functionalized and soluble in water, facilitating its alignment in water. However, although GO can be electrically conductive after reduction, structural defect level of reduced GO is still high due to permanent damages on fine lattice structure of graphene, which are introduced by extreme oxidation condition in GO preparation but can not be fully recovered by reduction, inevitably debating its thermal conductivity by 3 to 4 orders of magnitude. In order to obtain a high thermally conductive array, we align reduction-free thermally conductive surface functionalized multilayer graphene sheets (fMGs). According to a method reported by

Veca *et al* [54], fMGs are prepared in a moderate oxidation environment (mixed sulfuric and nitric acid) with aid of sonication, in contrast with the extreme oxidation conditions in GO preparation [20].

3.2.1 Thickness characterization by AFM

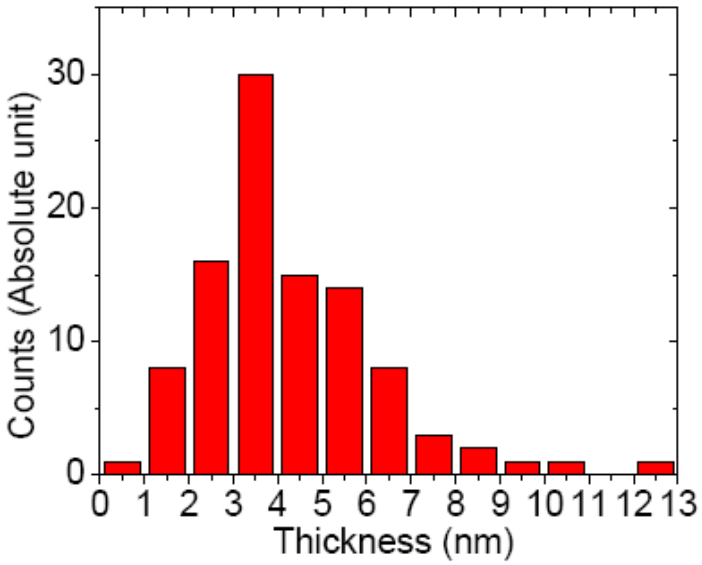

Figure 3.2 AFM measurement of fMGs: A. Image of a typical fMG (left: a 2-D height image of a typical fMG on Si wafer, right: altitude of geometry along the white line in left figure); B. Thickness distribution of fMGs.

Thickness of thus-prepared fMGs is mainly centered between 2 and 10 nm, as evidenced by an AFM height image in Figure 3.2. AFM height images show that thickness of fMGs is relatively low distributed with an average thickness value of 4.28nm, corresponding to 12.8 graphene layers.

3.2.2 Raman characterization of fMGs

In order to further explore the true situation of Raman spectra of fMGs, tens of spectra of fMGs are taken. It is found that the intensity of the 2D peaks is highly concentrated within a range between 1/3 and 1/2 of G band peaks. Moreover, conforming what we reported in the previous manuscripts, shape of thus obtained 2D peaks always shown obvious difference from that of graphite.

Raman spectra in this work are obtained from A-fMGs sample with functional groups [], which is different from pristine graphene sheets described by Ferrari's work. Electrical structure of graphene may also influenced by defects and functional groups, e.g. carboxyls. Previous research indicated that graphene oxide, which is highly functionalized with oxygen-containing groups and has a high defect level, has much lower 2D peak intensity, as reported by Eda *et al* [55]. Here, it is believed that influence of functional groups and defects on Raman spectra of fMGs is essential.

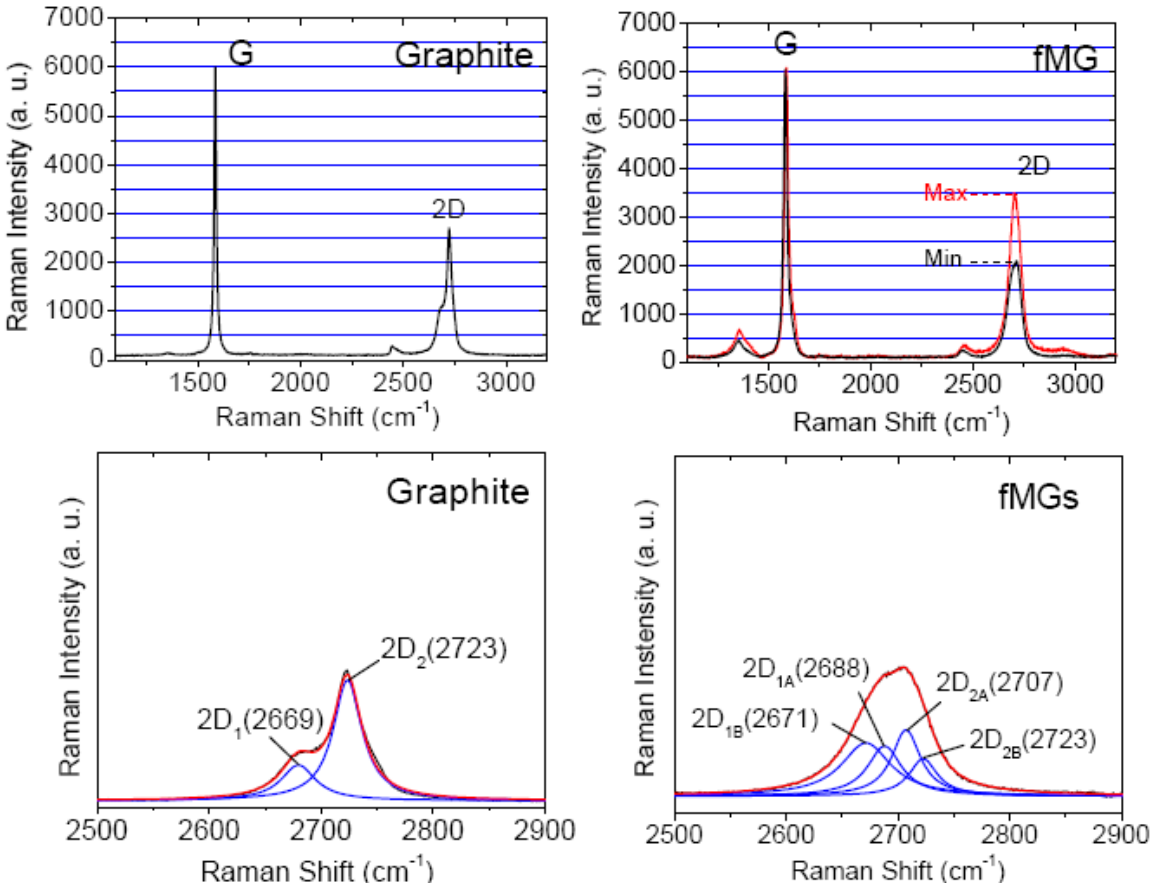

Figure 3.3 A comparison of Raman spectra between graphite and fMGs.

Here, Raman spectrum of fMGs in Figure 3.3 shows 2D peak at ~2701±6 cm^{-1} with an intensity ranging from 1/3 ("Min" in Figure 3.3) to half ("Max" in Figure 3.3) of G band peak intensity. In contrast to an asymmetric 2D peak of graphite at ~2723 cm^{-1}, 2D peak of fMGs is symmetric. Further analysis also indicates that 2D peak in a typical

Raman spectrum of fMGs can be corresponded to four peaks such as $2D_{1B}$ (~2671cm^{-1}), $2D_{1A}$ (~2688cm^{-1}), $2D_{2A}$ (~2707cm^{-1}), and $2D_{2B}$ (~2723cm^{-1}).

3.2.3 XPS characterization

Functionalization of the fMGs is characterized by X-ray Photoelectron Spectroscopy (XPS). In Figure 3.4, fMGs show an O1s peak and an asymmetric C1s peak corresponding to carboxylic groups (288.4eV), carbon-hydroxyl bonding (285.3eV), and conjugated carbon (284.3eV), comparing with the symmetric C1s peaks (284.4eV) of pristine graphite.

According to Wagner *et al*'s work [111], the empirical atomic sensitivity factors for O1s and C1s are 0.66 and 0.25, respectively. Here, an empirical equation is applied in calculating concentration of oxygen on pristine graphite, side-wall surface (surface A) and cross-section surface (surface B) of A-fMGs.

$$C_O = \frac{\frac{P_O}{S_O}}{\frac{P_O}{S_O} + \frac{P_C}{S_C}} = \frac{\frac{P_O}{P_C}\frac{S_C}{S_O}}{\frac{P_O}{P_C}\frac{S_C}{S_O} + 1} \qquad \textbf{Equation 3.2}$$

Where C_O, P_O, P_C, S_O, and S_C present concentration of O atoms, integrated peak area of O1s from XPS spectra, integrated peak area of C1s from XPS spectra, atomic sensitivity factors for O1s, atomic sensitivity factors for C1s, respectively. Thus calculated concentrations of O atoms for prinstine graphite, sidewall of A-fMGs (surface A) and cross-section surface of A-fMGs (surface B) are ~2.5%, 17.7% and 33.8%, respectively, as listed in Table 3.1.

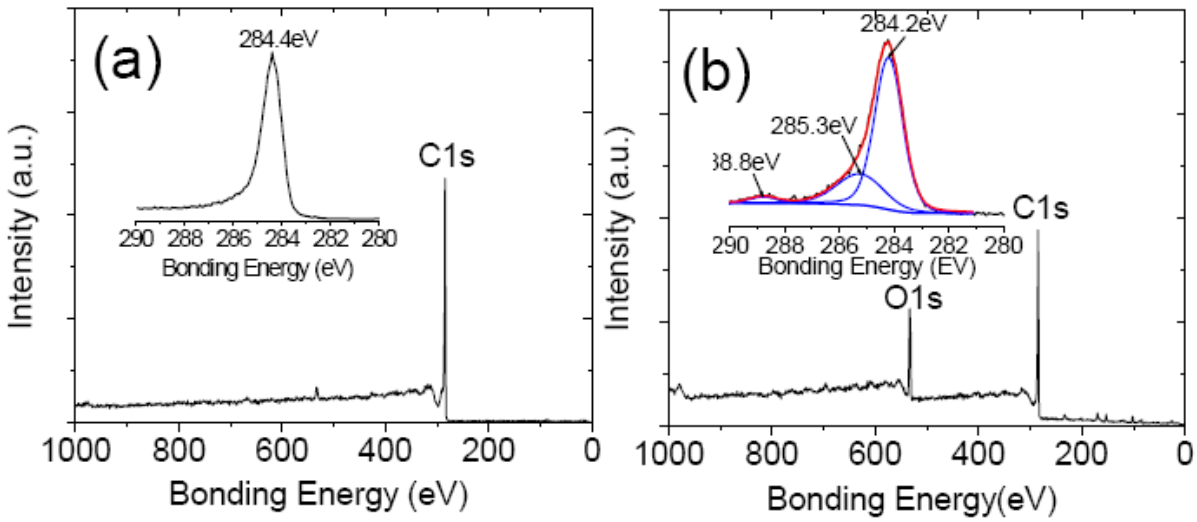

Figure 3.4 A comparison of XPS spectra between (a) pristine graphite and (b) fMGs. Inserted are related high resolution C1s spectra. The XPS spectra of fMGs shown here are identical with that of surface A in Figure 4.5.

Table 3.1 A data list of oxygen concentration calculation based on low resolution XPS.

Sample	$\frac{P_O}{P_C}$	$C_O(\%)$
Prinstine graphite	0.069	2.5
A-fMGs (surface A)	0.571	17.7
A-fMGs (surface B)	1.347	33.8

3.2.4 FTIR

FTIR spectra in Figure 3.5 also confirmed the functionalization by showing peaks at 3448 cm^{-1} (-OH), 1380 and 1727 cm^{-1} (C=O).

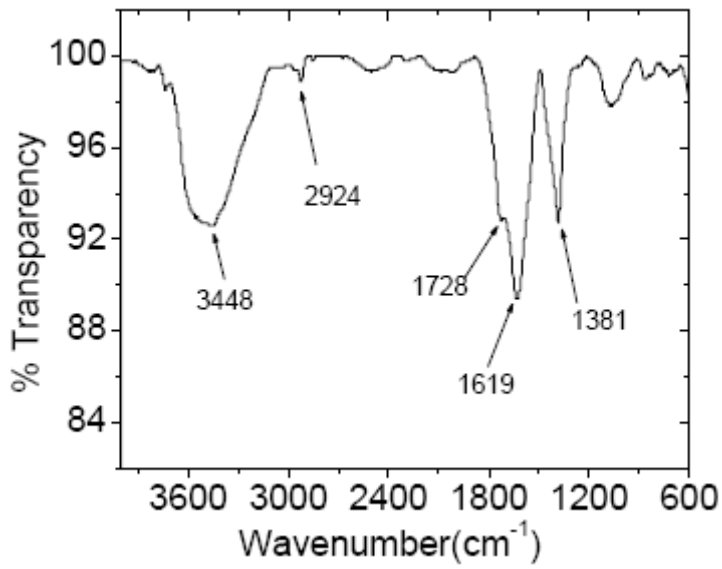

Figure 3.5 FTIR spectrum of fMGs

3.3 Alignment of fMGs

3.3.1 Alignment

Carboxyl groups on fMGs surface can be ionized by water molecules, shown in Figure 3.6. Thus generated negative charges on the surface of fMGs provide strong electronic repulsion forces, efficiently improving the dispersion of fMGs in water [20]. In the following vacuum filtration process, a piece of anodic aluminum oxide (AAO) filtration paper with a pore size of 100nm holds fMGs conformally on its surface, resulting in fMGs' orientation. As water flows down through gaps between oriented fMGs, the following fMGs confirm the orientation of previously oriented fMG layers, resulting in the fMGs' conformal orientation along the filtration paper. A filtration cake of aligned fMGs with a density of ~1.6 g cm^{-3}, a diameter of ~32 mm, and a thickness up to 1.05 mm is obtained, as shown by Figure 3.7.

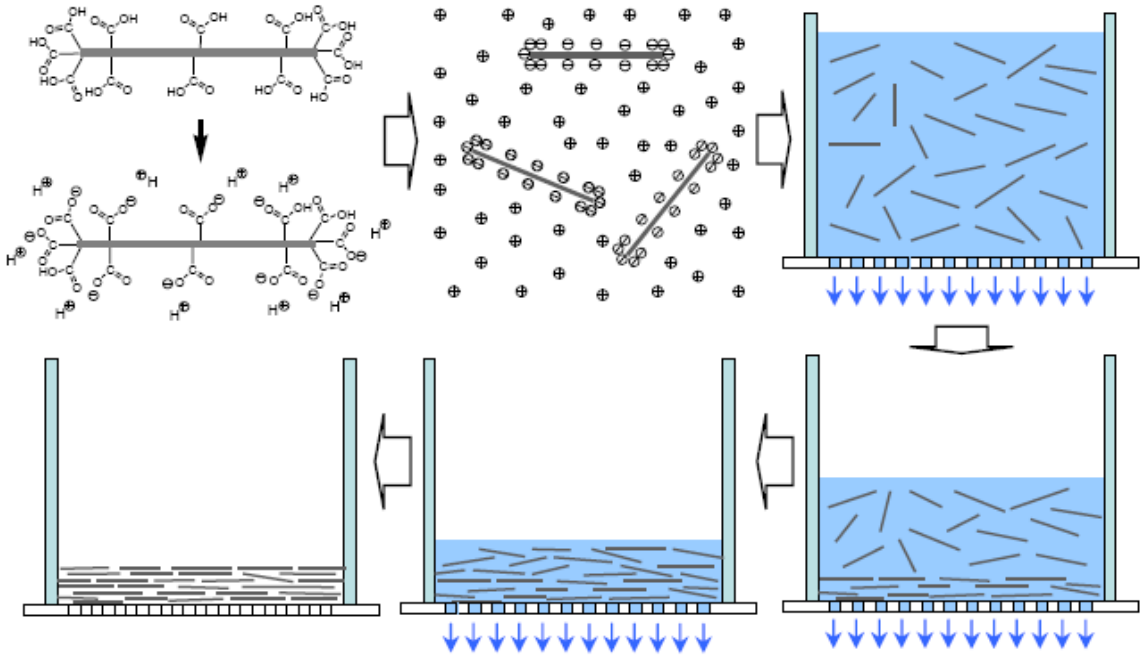

Figure 3.6 Schematic illustrations of lyotropic alignment for fMGs.

Figure 3.7 (A) Well-dispersed fMGs in water. (B) A-fMG sample with a diameter of ～32 mm. (C) A-fMG sample with a thickness of 1.05 mm.

3.3.2 AFM of aligned fMGs

An AFM image of thus-prepared A-fMGs is shown in Figure 3.8. It is found that thickness of fMGs in the tested region mainly centered between 2 and 10 nm with an average of 7.35nm, which is compatible with result of individual fMGs shown in Section 3.2.1 and Figure 3.2, reflecting the true situation of fMGs. This result is also compatible with that reported by Veca and Sun et al [54].

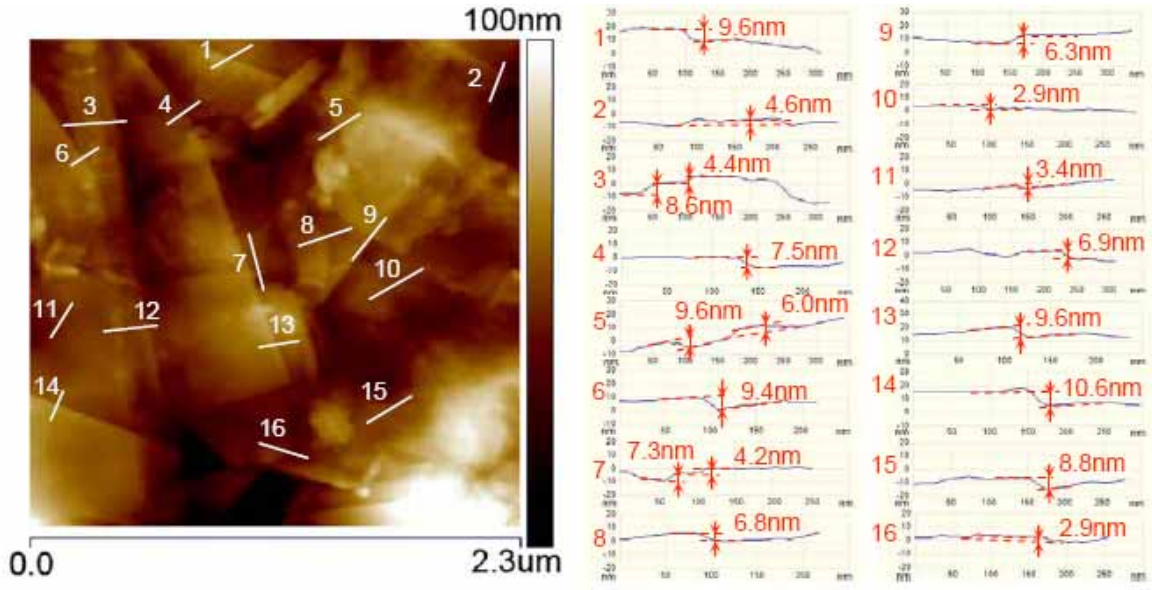

Figure 3.8 An AFM height image of A-fMGs surface and corresponding thickness information.

3.3.3 SEM

SEM images in Figure 3.9, show a laminated structure of the aligned fMGs, reflecting the high efficiency of lyotropic alignment within the throughout thickness of ~0.7mm.

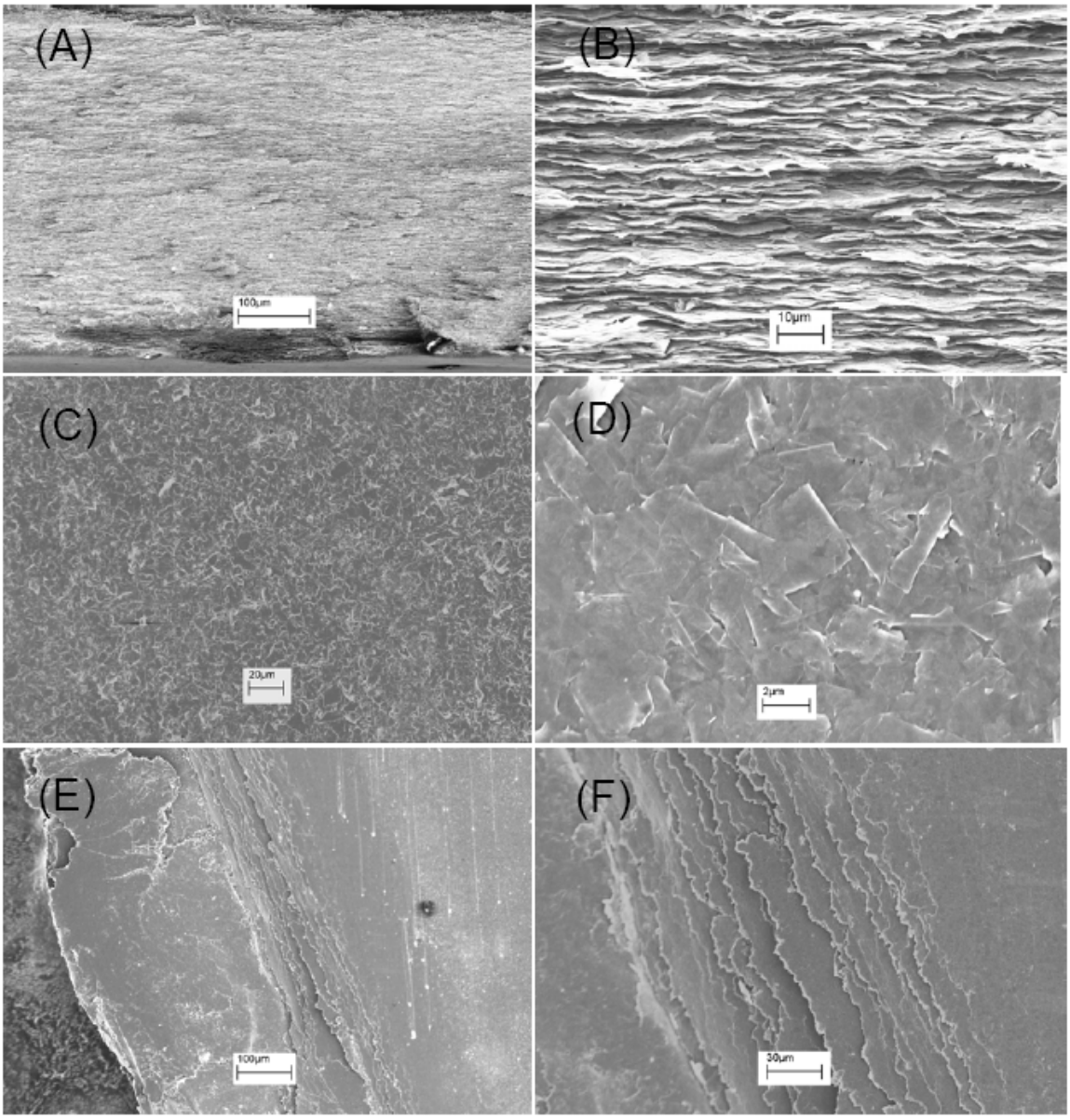

Figure 3.9 (A) A SEM image of A-fMGs cross-section view. (B) A SEM image of a magnified cross-section view of A-fMGs samples. (C) A SEM image of a top view of A-fMGs. (D) A SEM image of a magnified top view of A-fMGs. (E). A SEM image of an A-fMGs sample broken with gradient. (E). A SEM image of a magnified view of A-fMGs sample broken with gradient.

3.3.4 Polarized Raman Spectroscopy

Thermal transport along graphene sheets has been proven to be dominated by phonon transferring [8]. Raman measurement has been widely accepted as a powerful methodology in characterizing phonon modes of graphitic forms. Moreover, previous

researches indicated that polarized Raman spectra are able to characterize anisotropy due to the sensitivity of Raman intensity on polarization geometries [28, 112, 113, 114, 115].

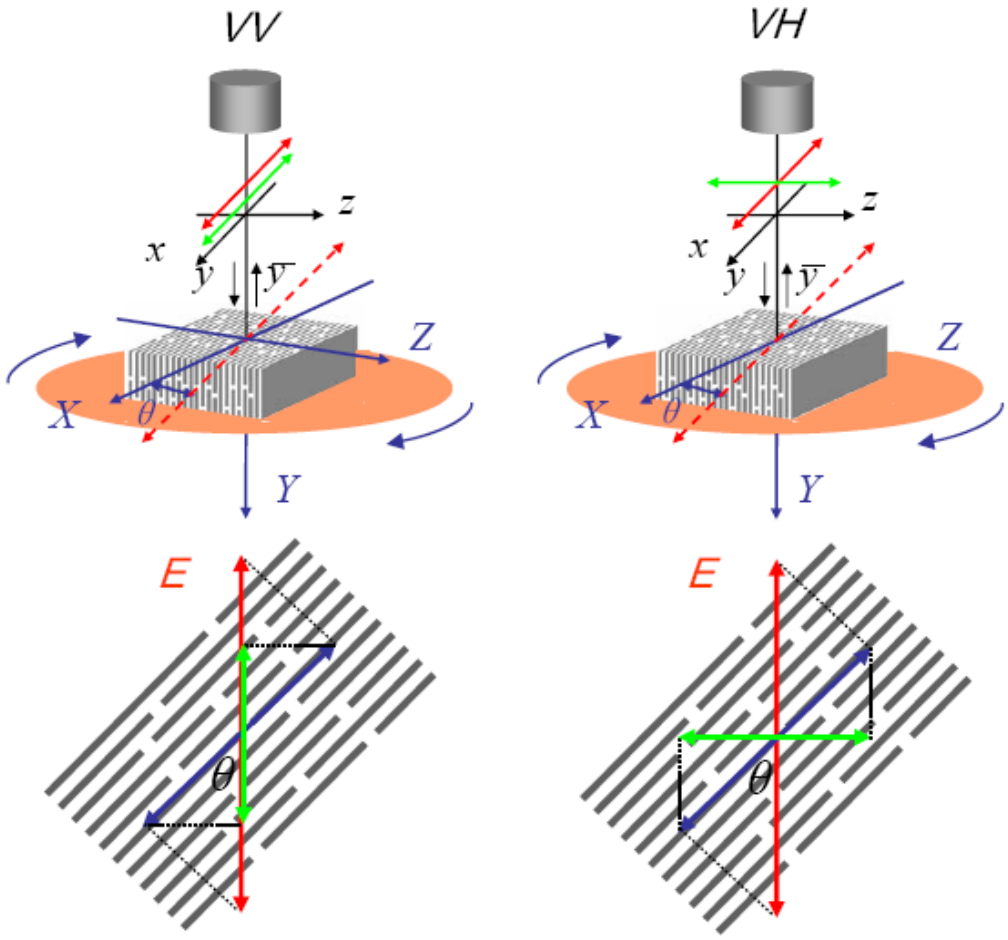

Figure 3.10 Schematic illustrations of "*VV*" and "*VH*" configurations. Orientation of fMGs, polarization directions of incidental light and analyzer are shown by the blue, red and green doube-arrows, respectively. Black arrows (*x,y,z*) denote the 3 axles in absolute coordinate system, while the blue arrows show 2 in-plane directions (*X* and *Y*) and cross-plane direction (*Z*) of A-fMGs, respectively. θ is the angle between polarization of incident light and fMGs orientation.

However, in contrast, a systematic characterization and fundamental understanding on anisotropy of aligned graphene arrays is desired but not reported yet. A study on anisotropy of aligned functionalized multilayer graphene in the research will be promising in kindling a new region of research related with graphene, which is comparable with that of aligned carbon nano tubes in history. Here, for the first time according to our knowledge, polarized Raman spectroscopy is applied in characterizing

orientation uniformity of graphene sheets in an array, which is closely related to thermal and electrical conductions.

As detailed in Figure 3.10 and Methods, a polarized analyzer is applied to detect backscattering light intensity and set in directions parallel or perpendicular to polarization of incident laser, which are usually named as "*VV*" (vertical/vertical) and "*VH*" (vertical/horizontal) configurations. Angle (θ) between polarization of incident laser and orientation of A-fMGs is applied to describe the polarization geometries. The sensitivity of measured G band intensity on angle θ is studied by an analysis of polarized Raman spectra obtained with different θ (every 10^o from 0 to 360^o) in both of the configurations. In Figure 3.11, measured Raman intensities of G band in "*VV"* configuration show periodical alternations between peaks and valleys every 90^o, which are not prominent in "*VH"* configuration.

During the excitation process of the Raman scattering, energy is absorbed by "interband optical transitions" from electric vector of incident light to the phonons vector along the conjugated carbon sheets. According to the depolarization effect reported by Ajiki et al [116], the "interband optical transitions" can happen only along the vector component parallel to the orientation of polarized phonon carriers. Here, A-fMGs can be considered as polarized phonon carriers. Naturally, in excitation process, projection of incident electric vector E on the orientation direction of A-fMGs is scaled proportionally to $\cos\theta$, resulting in the proportional dependence of absorption intensity (I_A) upon $\cos^2\theta$. Intensity of backscattering light, I_S, can be considered as proportional to I_A to confirm conversion of energy in an equilibrium state, as shown by Equation 3.3.

$$I_s \propto I_A \propto \left(|E|\cos\theta\right)^2 \propto \cos^2\theta \qquad \textbf{Equation 3.3}$$

Measured Raman intensity scales proportional to the squared projection of backscattering electric vector in the polarization direction of analyzer. Theoretically,

Raman intensities for "VV" and "VH" configuration "$I_{VV}(\theta)$" and "$I_{VH}(\theta)$" should obey Equation 3.4 as follows.

$$\frac{I_{VV}(\theta)}{I_{VH}(\theta)} = \frac{\left(\sqrt{I_S}\cos\theta\right)^2}{\left(\sqrt{I_S}\sin\theta\right)^2} = \frac{\left(|E|\cos\theta\cos\theta\right)^2}{\left(|E|\cos\theta\sin\theta\right)^2} = \frac{\cos^4\theta}{\cos^2\theta\sin^2\theta} \qquad \textbf{Equation 3.4}$$

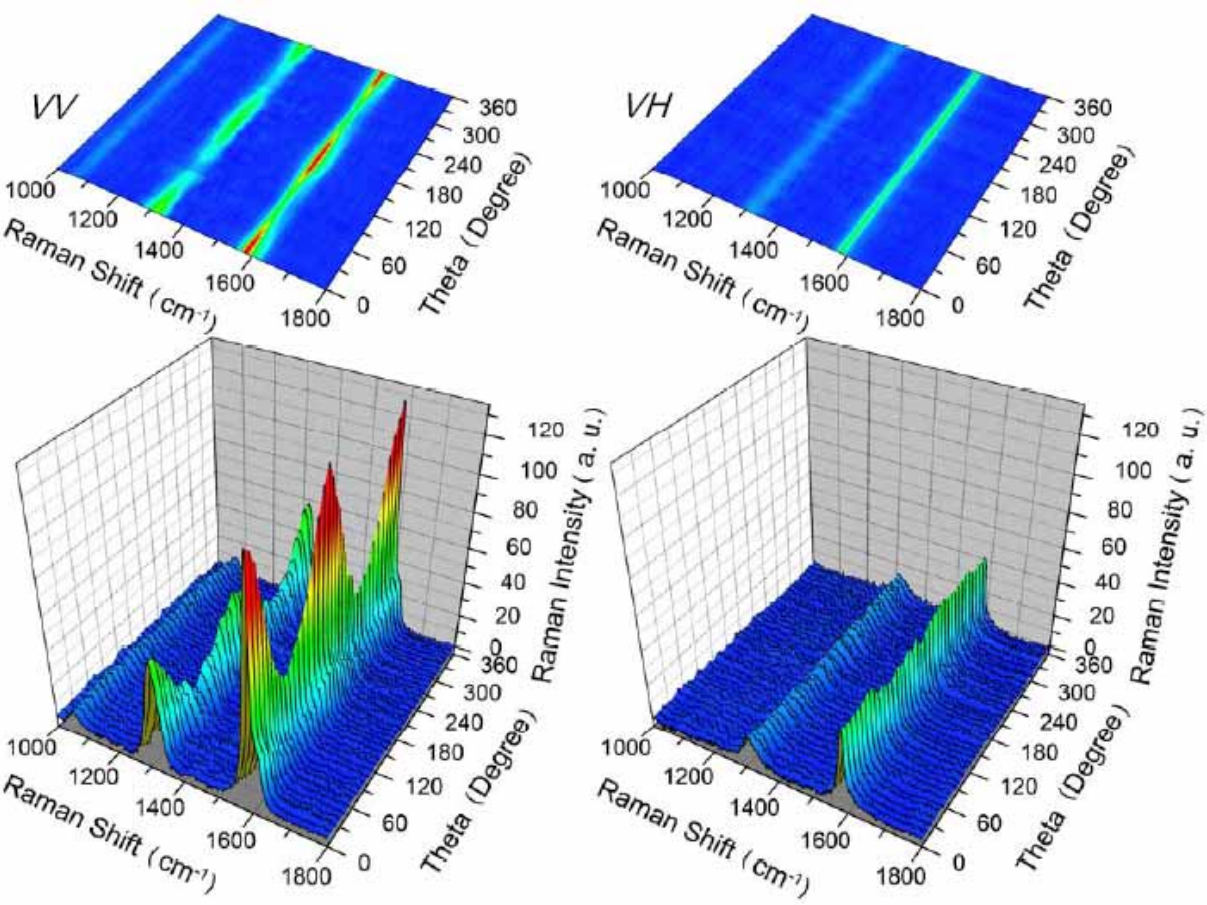

Figure 3.11 A 3-D illustration of measured Raman intensity for "*VV*" and *"VH"* polarization configurations

Thus, applying the G band intensity when θ is equal to 0° in "*VV*"configuration, $I_{VV}(0^\circ)$, as a reference, relative Raman intensities for "*VV*" and "*VH*" configurations at G band, $I_{R,VV}(\theta)$ and $I_{R,VH}(\theta)$ are theoretically equal to $\cos^4\theta$ and $\cos^2\theta\sin^2\theta$, respectively. The dependence of $I_{R,VV}(\theta)$ on $\cos^4\theta$ explains its significant reducing trend as angle θ

changes from 0 to 90° in Figure 3.12. In contrast, measured $I_{R,VH}(\theta)$ showed a much smoother value changing from 0.276 to 0.313, with a broad peak at ~50° within a range from 0 to 90°, showing a much weaker fluctuation corresponding to its theoretical value of $\cos^2\theta\sin^2\theta$. Depolarization ratio ($I_{VV}(90°)/I_{VV}(0°)$) of G band intensity in "*VV*" configuration is 0.276±0.06, comparable to 0.204 (calculated from $I_{VV}(0°)/I_{VV}(90°)$=4.9) for a fiber from aligned single walled carbon nanotubes [113] , suggesting an efficient alignment of fMGs. [112, 117, 118].

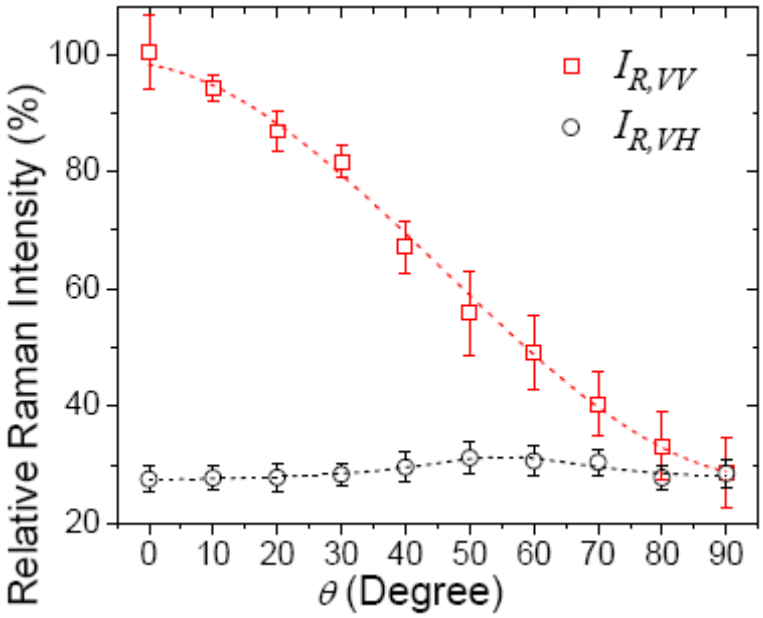

Figure 3.12 Measured relative density of at 1581cm^{-1} of A-fMGs for "VV" and "VH" configurations as a functional of angle θ.

3.4 Anisotropic Properties of A-fMGs

In our A-fMGs, ultra low dimensional 2-D carbon sheets are aligned layer by layer, with unavoidable ultra thin gap between the adjunct layers. The structure generates micro-channels on the cross-section surfaces along orientation directions of A-fMGs sample.

Anisotropy of A-fMGs induced by lyotropic alignment is also confirmed by unique anisotropic physical properties. Thermal-mechanical, electrical and thermal

property measurement are are carried out in different directions. In-plane and out-of plane coefficient of thermal expansion (CTE), electrical and thermal conductivity of are defined and shown in by Figure 3.13, reflecting the unique physical structure of the A-fMGs sample.

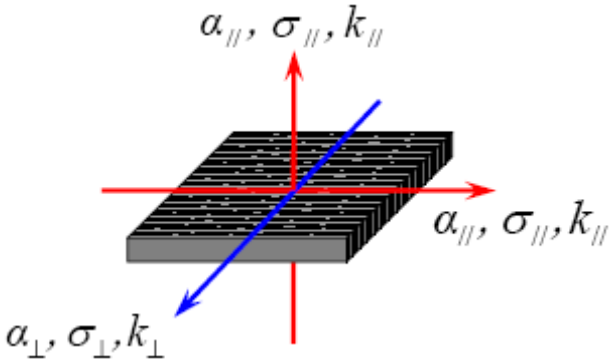

Figure 3.13 A schematic illustration of in-plane and cross-plane CTE, electrical and thermal conductivity of A-fMGs.

3.4.1 Coefficient of thermal expansion (CTE)

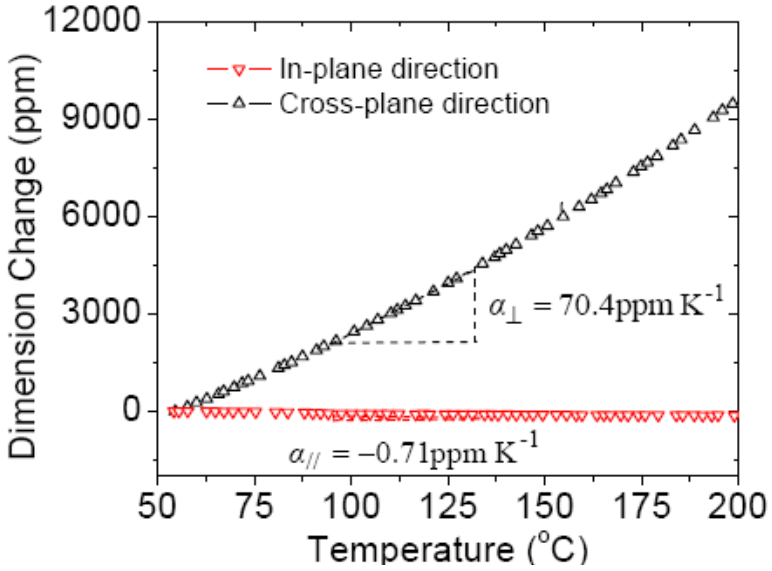

Figure 3.14 Thermal Mechanical Analysis of A-fMGs. Slopes of the curves are in-plane and cross-plane coefficients of thermal expansion (CTEs), respectively.

Distinguish difference of coefficient of thermal expansion (α) between lateral (-0.71 ppm/ºC) and thickness direction (70.4ppm/ºC) directions also reflects high anisotropy of our A-fMGs, as shown in Figure 3.14. It has been well known that the

covalent bondings along conjugated carbon sheets result low CTE values, as has been observed in CNTs and graphite [119, 120, 121, 122]. Meanwhile, the loose Van der Waals forces and absence of covalent bonding contributes to the relatively large CTE values along cross-plane direction. Here, although cross-plane CTE of A-fMGs is found to be larger than that of "*c*" axe in a fine graphite lattice at room temperature (~28 ppm K^{-1})[33] due to a relatively loose packing of A-fMGs, the result is compatible with reported low in-plane CTE values (~ -2 ppm K^{-1}) along "*a*" axe of graphite crystallite and axle direction of carbon nanotubes.[33, 34]

3.4.2 Electrical conductivity

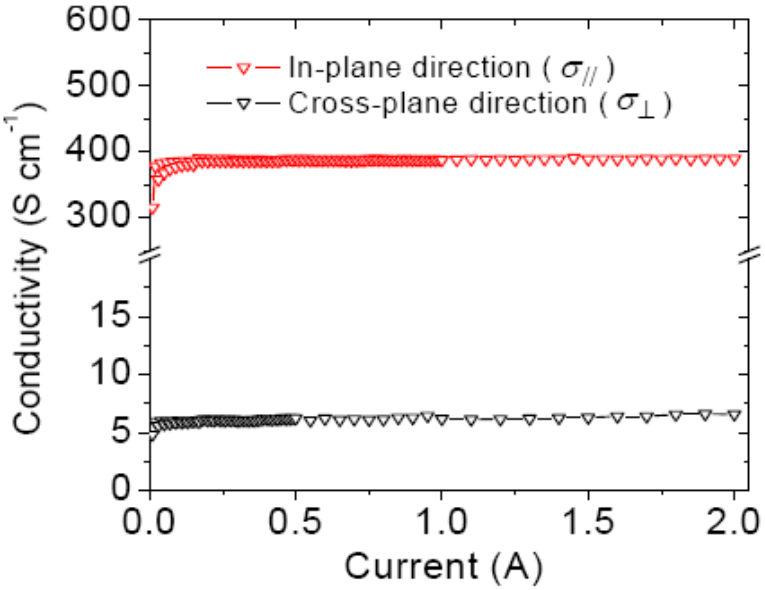

Figure 3.15 In-plane and cross-plane electronic conductivity of A-fMGs measured at room temperature.

Electrical conductivity (σ) at room temperature in both lateral (in-plane) and thickness (out-of-plane) directions are measured and plotted in Figure 3.15. By showing stable values at 386S/cm^{-1} (with a standard deviation value of 7.68S/cm^{-1}) lateral direction and 6.1/cm^{-1} (with a standard deviation value of 0.23S/cm^{-1}) thickness direction, the A-fMGs sample shows Ohmic electrical contacts in both of lateral and thickness directions. Moreover, anisotropic thermal conductivities of the A-fMGs sample are observed. A-

fMGs show an even stronger anisotropy ($\sigma_{//}/\sigma_{\perp} = 63.3$ at 25°C) of electrical conductivity than that of vertical aligned carbon nanotube arrays ($\rho_{\perp}/\rho_{//}$ is smaller than 10 at room temperature [94]).

3.4.3 Thermal conductivity

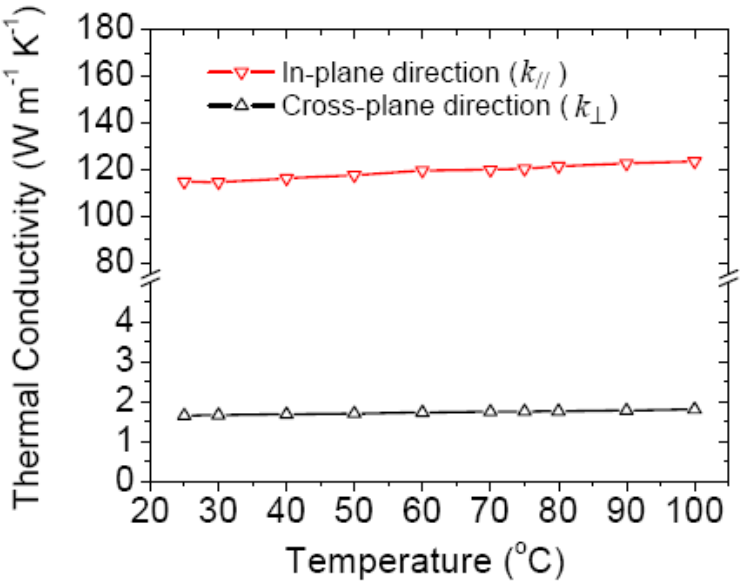

Figure 3.16 In-plane and cross-plane thermal conductivity of A-fMGs.

In Figure 3.16, the thermal conductivity of A-fMGs in lateral (in-plane) and thickness (out-of-plane) directions at temperature from 25-100ºC are plotted by two curves. Comparing with thermal conductivity (from 1.66 to 1.81 W/m·K) in thickness direction, lateral thermal conductivity shows distinguished higher values between 114.7 and 123.5W/m·K. The distinct difference in thermal conductivities between the two perpendicular directions suggests the highly anisotropic nature in A-fMGs physical structure. Rapid phonon transfer through the rigid carbon-carbon covalent bonds accounts for the ballistic thermal conductance along honeycomb-like graphene sheets. Here, an efficient alignment can optimize in-plane thermal conductivity of aligned fMGs to a remarkable degree ($k_{//}/k_{\perp}$ =69.3 at 25°C). In-plane sketching phonon mode E_{2g}, which is

usually corresponded to G band in Raman spectra, has a dominating function in thermal transfer along graphene [28, 112, 113, 114]. A high sensitivity of G band on angle θ in "*VV*" configuration in Polarized Raman spectra indicates that orientation of fMGs is statistically narrow-distributed, facilitating a ballistic phonon transport and a high thermal conductivity in in-plane direction of A-fMGs.

The statistical uniformity in orientation of graphene sheets obviously influents the thermal conductivity of their bulky samples. As shown by Polarized Raman tests in our study, orientation of the strong E_{2g} phonon mode ("in-plane") is statically uniform and responsible for the high thermal conductivity of the A-fMG materials in the lateral direction, while the much weaker A_{1g} phonon mode ("out-of-plane") and loose Van der Waals forces along the normal direction of A-fMG sheets should be accounted for the low thermal conductivity in thickness direction. Lyotropic alignment method provides a convenient method to prepare arrays of parallelly packed fMGs with high anisotropy and large-scale cross section area of thermal pass, suggesting their promising potentials as thermal conductors.

3.5 Conclusion

Here, we summarize the work as a convenient approach to align functionalized multilayer graphene in water-based solutions at room temperature. The high efficiency of "lyotropic alignment" is confirmed by the experimental results from SEM, polarized Raman, contact angle test, TMA, electronic and thermal conductivity measurements. Based on the detailed discussion on polarized Raman test results, the strong sensitivity of Raman intensity on polarization geometry is further understood and corresponded to the oriented layer structure of our A-fMGs. The dramatic differences of electronic and thermal conductivity between lateral and thickness directions are obtained by the lyotropic alignment method, suggesting a strong anisotropy.

CHAPTER 4 A THREE-DIMENSIONAL VERTICALLY ALIGNED MULTILAYER GRAPHENE STRUCTURE: AN APPROACH FOR GRAPHENE-BASED THERMAL INTERFACIAL MATERIALS

Low operation temperature and efficient heat dissipation are important for device life and speed in current electronic and photonic technologies. However, gaps between contact solid surfaces such as silicon dies, metallic heat spreaders and heat sinks, *etc*, cause high interfacial thermal resistance, resulting in a major bottleneck of heat dissipation in various devices [85, 86, 123, 124]. Gap-filling thermal interfacial materials (TIMs) based on carbon nanomaterials, *e.g.* carbon nanotubes and carbon nanofibers, were substantially studied in order to handle the bottleneck, however, are still limited by large contact thermal resistance [67, 125]. Graphene, a ultra-thin flat membrane from sp^2 carbon atoms, is a novel promising candidate for TIMs in nowadays electronic and photonic devices [8].

Graphene has extraordinarily high in-plane electrical mobility [1], thermal conductivity [8], mechanical strength [29] and ultra large specific surface area [4]. Due to these unique properties, within several years since its discovery, graphene has been widely applied in microelectronic devices [2], chemical sensors [9], transparent electrically conductive films [5], electrodes of energy storage devices,[11] and fillers in conductive polymeric composites [56], *etc*. It is noticed that relative arrangements of graphene in devices are crucial for their multiplex applications. For example, graphene recumbent on solid substrates can be patterned and interconnected for field effect transistor application [3, 37, 126.] In contrast, graphene must be stacked in a 3-D porous

structure in electrodes of electrical storage devices to facilitate rapid ion dissipation and make full use of its large specific surface area. Therefore, particular arrangements of graphene in various devices are necessary for their diverse functions. For TIM application, efficient heat dissipation and reduced interfacial thermal resistance in normal direction of contact solid surfaces are desired, so that graphene is expected to be vertically stacked between contact solid surfaces. However, as an ultra-thin membrane-like material, graphene is susceptible to Van der Waals forces and usually tends to be recumbent on substrates. Thereby, direct growth of vertically aligned free-standing graphene on solid substrates in large scale is difficult and rarely available in current studies, bringing significant barriers in applying graphene as TIMs.

In this work, it is found that if aligned and densely packed in an array, multilayer graphene sheets can be self-supported, conveniently rearranged and vertically assembled between solid surfaces thereafter, circumventing the significant difficulty in direct growth of vertically aligned graphene arrays. In addition, large-volume heat dissipation requires a joint contribution of a large number of graphene sheets. Alignment is crucial in bulk processing of graphene because it orients graphene sheets and optimizes properties of large-scale graphene arrays in their orientation direction. Although direct alignment of pristine graphene in a large scale array is still absent, previous researches on graphene oxide (GO) and reduced GO indicate that alignment can make best use of their extraordinary in-plane properties. Stankovich *et al* first prepared paper-like aligned GO with notably high mechanical strength [56]. Chen *et al* reported a high electrical conductivity of thermally-reduced GO paper [127]. However, in-plane thermal conductivity of both GO and reduced GO (1.9 W m^{-1} K^{-1} and 0.14-2.87 W m^{-1} K^{-1},

respectively) is 3 to 4 orders of magnitude lower than pristine graphene [21, 128].Thereby, further efforts on preparation of high thermally conductive graphene-based nanomaterials in large-scale arrays must be addressed.

Here, thermally conductive functionalized multilayer graphene sheets (fMGs) are prepared according to method reported by Veca *et al* [54]. Thus prepared fMGs are aligned with a vacuum filtration method at room temperature. An efficient alignment of fMGs is evidenced by SEM images and quantified by polarized Raman spectroscopy according to a "depolarization effect" [116]. Strong anisotropies in properties of aligned fMGs (A-fMG) are founded. Remarkably high electrical and thermal conductivity as well as ultra low coefficient of thermal expansion (CTE) in in-plane direction of A-fMGs are obtained without aid of any reduction process. Moreover, a three-dimensional vertically aligned fMG TIM (VA-fMG TIM) architecture is constructed between contacted Silicon/Silicon surfaces with pure Indium as a metallic medium. Significantly higher equivalent thermal conductivity and lower contact thermal resistance of VA-fMG TIMs are obtained, compared with their counterpart from recumbent A-fMGs. This finding provide a throughout approach for a graphene-based TIM assembly as well as knowledge of vertically aligned graphene architectures, which may not only facilitate current demanding thermal management but also promote graphene's widespread applications such as electrodes for energy storage devices, polymeric anisotropic conductive adhesives, *etc*.

4.1 Methods

4.1.1 TIM assembly.

Si wafers (1mm*1mm) are coated with melt pure Indium at 180 ºC. Thickness of the Indium coating is ~10um after careful polishing at room temperature. A-fMG sample are sliced and sandwiched between thus prepared Si wafers with an orientation of fMGs parallel or perpendicular to the contacted Si surfaces, corresponding to RA-fMG and VA-fMG TIM assemblies, respectively. The sandwiched samples are clamped with small pressure (~0.02 MPa) and placed in a convection oven at 200ºC for 20 min and cooled to room temperature. No pressure is applied in equivalent thermal conductivity measurements of thus-prepared TIMs.

4.1.2 Contact angle tests.

As shown by Figure 4.1, contact angle tests are conducted on A-fMGs in three geometries. **A**). A water droplet (1 uL) is dropped on a sample surface which is parallel to both X and Y axles but perpendicular to Z axle, then contact angle is measured from a view angle parallel to X axle (or Y, which is identical with X axle in this case). **B**) A water droplet (1 uL) is dropped on a cross-section surface of A-fMGs. Then contact angle is measured from a view angle parallel to X axle. **C**) A water droplet (1 uL) is dropped on a same surface as geometry **B**, but contact angle is measured from a view angle parallel to Z axle.

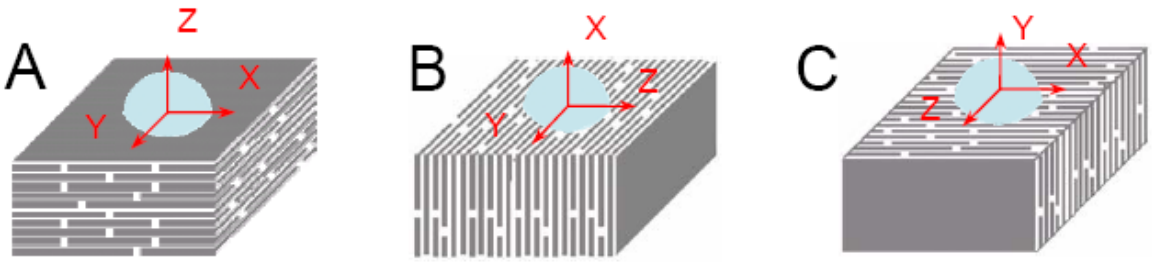

Figure 4.1 A schematic illustration of geometries applied in contact angle tests.

4.1.3 Thermal conductivity measurement.

A light flash apparatus (LFA 447 NanoFlash, Netszch Thermal Analysis) and a sophisticated analysis software (Proteus LFA Analysis, Netszch Thermal Analysis) with a mathematical model designed for triple layer sandwich samples are applied in measuring equivalent thermal diffusivities of A-fMG TIMs (α_{TIM}) by experimentally collecting and mathematically fitting non-linear regression of data signal with consideration of heat loss. Here, as shown in Figure 4.2, measured α_{TIM} includes effects of interfacical thermal resistance across A-fMGs/In/Si interface ($R_{A\text{-}fMGs/In/Si}$) and intrinsic thermal resistance of A-fMGs. Two configurations of A-fMGs in TIMs layer are measured and compared. In one of the configurations, an A-fMG sample is recumbent between Si surfaces. Bond line thickness (*BLT*) of the sandwiched recumbent A-fMG TIMs is 0.71 mm. In contrast, in the other configurations, A-fMGs are sliced and vertically stacked between Si wafers with a *BLT* of 2.3mm. As shown in Table 4.1, measured equivalent thermal conductivity (k_{TIM}, calculated from $k_{TIM} = \alpha_{TIM}\rho_{TIM}C_{p,TIM}$) of the described recumbent A-fMG TIMs (RA-fMG TIMs) and vertically stacked A-fMG TIMs (VA-fMG TIMs) are 1.39 and 75.5 W m^{-1} K^{-1}, respectively. Thermal resistance (R_{TIM}) of the RA-fMG TIMs and VA-fMG TIMs are calculated from following equation:

$$R_{TIM} = \frac{BLT}{k_{TIM}} = 2R_{A-fMGs/In/Si} + \frac{T}{k} \qquad \textbf{Equation 4.1}$$

It is notice that R_{TIM} includes effects of interfacial thermal resistance across A-fMGs/In/Si multiple interface (*RA-fMGs/In/Si*) and intrinsic thermal resistance of A-fMGs ($\frac{T}{k}$), as shown in the following equation. Uncertainty of $R_{A\text{-}fMGs/In/Si}$ shown in Figure 4.4 is valued according to an error transfer function as follows.

$$\delta R_{A-fMG/In/Si} = \frac{1}{2}\sqrt{\left(\frac{L\delta k_{TIM}}{k_{TIM}^2}\right)^2 + \left(\frac{T\delta k}{k^2}\right)^2} \qquad \textbf{Equation 4.2}$$

where $\delta R_{A-fMGs/In/Si}$, δk_{TIM}, δk_{A-fMGs} are uncertainties of $R_{A\text{-}fMGs/In/Si}$, k_{TIM}, and k, respectively.

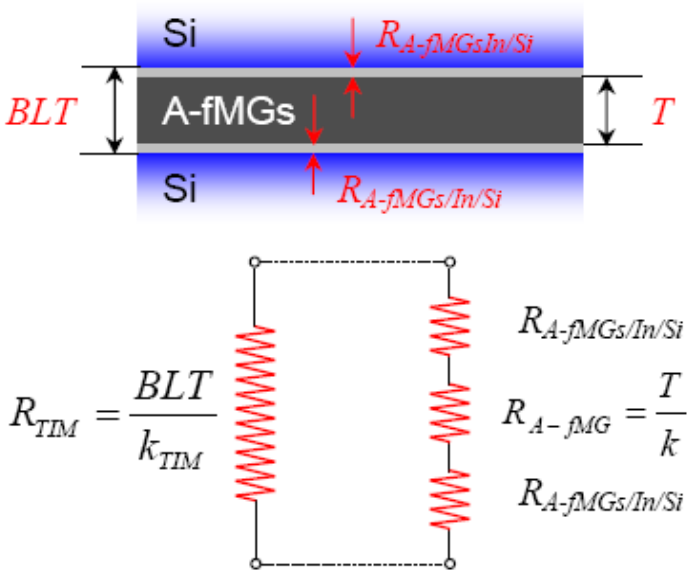

Figure 4.2 A schematic illustration of thermal conductivity measurement of assembled A-fMGs TIMs.

4.2 Assembly of A-fMG TIM Architectures

Three dimensional TIM architectures are constructed by assembling A-fMGs between Si/Si joint surfaces with a thin layer (~10um) of pure Indium as a metal medium. As illustrated in Methods and Figure 4.3, A-fMG samples are carefully sliced, rearranged and sandwiched between thus-prepared Si wafers with orientation of fMGs parallel or perpendicular to Si surfaces, corresponding to RA-fMG and VA-fMG TIM assemblies, respectively. RA-fMG TIM assembly is found vulnerable to mechanical shake and fails in standard drop test of reliability, while VA-fMG TIM assembly passes the tests without detachment, indicating a significantly better interfacial adhesion between VA-fMGs and Si substrates.

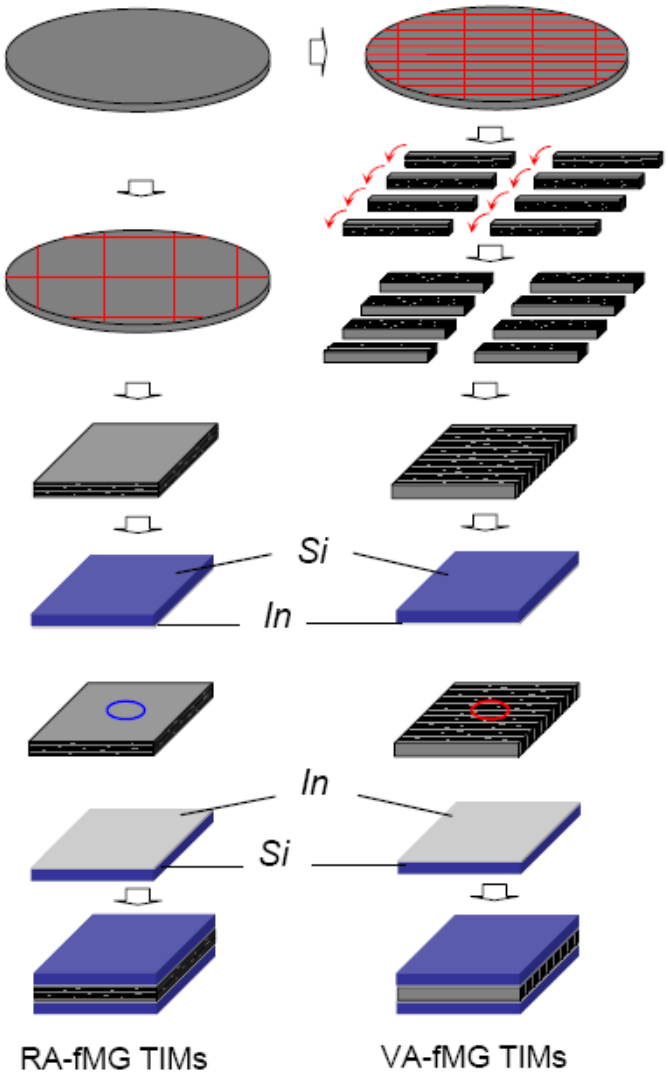

Figure 4.3 A schematic illustration of RA-fMG and VA-fMG TIM assemblies.

4.3 Thermal Conductivity of TIMs Assemblies

As detailed in Methods, equivalent thermal diffusivity (α_{TIM}) of both TIM assemblies is measured by a light flash apparatus (LFA 447 NanoFlash, Netzsch Thermal Analysis). A sophisticated analysis software (Proteus LFA Analysis, Netzsch Thermal Analysis) with a mathematical model designed for triple layer sandwich samples are applied in measuring equivalent thermal diffusivities of A-fMG TIMs (α_{TIM}) by experimentally

collecting and mathematically fitting non-linear regression of data signal with consideration of heat loss.

Table 4.1A data list of thermal measurement of assembled A-fMGs TIMs.

Configuration	VA-fMG TIMs	RA-fMG TIMs
BLT (mm)	2.30	0.71
T(mm)	2.28	0.69
$\rho_{A\text{-}fMGs}\ (g\ cm^{-3})$	1.6	1.6
$C_{p,\ A\text{-}fMGs}\ (J\ g^{-1}K^{-1})$	0.73	0.73
$\alpha_{A\text{-}fMGs}\ (mm^2\ s^{-1})$	96.1	1.38
k [a] $(W\ m^{-1}\ K^{-1})$	112.2	1.62
$R_{A\text{-}fMGs}$ [b] $(mm^2\ K\ W^{-1})$	20.3	426
$\alpha_{TIM}\ (mm^2\ s^{-1})$	64.6	1.19
$\rho_{TIM}\ (g\ cm^{-3})$	1.6	1.6
$C_{p,\ TIM}(J\ g^{-1}K^{-1})$	0.73	0.73
k_{TIM} [a] $(W\ m^{-1}\ K^{-1})$	75.5	1.39
R_{TIM} [b] $(mm^2\ K\ W^{-1})$	30.5	511
$R_{AfMG/In/Si}$ [c] $(mm^2\ K\ W^{-1})$	5.1	42.5

[a] Thermal conductivity of A-fMGs calculated according to an equation of $k = \alpha_{A-fMGs}\rho_{A-fMGs}C_{p,A-fMGs}$ **Equation 4.3**

[b] Thermal resistance caused by A-fMGs, calculated by $R_{A-fMG} = \frac{T}{k}$ **Equation 4.4**

[c] Calculated according to an equation of $R_{TIM} = \frac{L}{k_{TIM}} = 2R_{A-fMG/In/Si} + \frac{T}{k}$ **Equation 4.5**

Equivalent thermal conductivity of the described RA-fMG TIMs and VA-fMG TIMs are 1.39 and 75.5 W m^{-1} K^{-1}, respectively. In a comparison shown in Figure 4.4 and Table 4.1, it is noticed that equivalent thermal conductivity of VA-fMG TIMs is almost two

orders of magnitude higher than that of RA-fMG TIMs. Moreover, thermal resistance ($R_{AfMGs/In/Si}$) across A-fMGs/In/Si multiple interfaces in RA-fMG and VA-fMG TIMs are 42.5 and 5.1 mm^2 K W^{-1}, respectively.

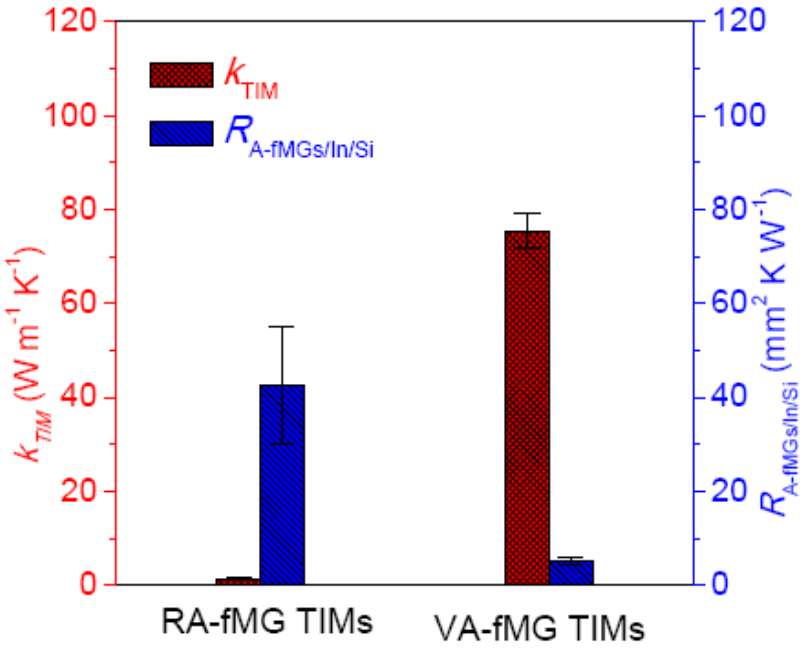

Figure 4.4 A contrast of equivalent thermal conductivity (k_{TIM}) and interfacial thermal resistance across A-fMGs/In/Si interface ($R_{A\text{-}fMGs/In/Si}$) between RA-fMG and VA-fMG TIM assemblies.

4.4 Advantage of VA-fMG TIMs

At least two reasons should be counted in for better adhesion and lower $R_{AfMGs/In/Si}$ of VA-fMG TIMs. First, interfacial thermal conductance between substrates and graphitic nanomaterials (*e.g.* carbon nanotubes) can be significantly improved by molecular-level interfacial chemical bonding [66]. Indium is capable to form relatively stable chemical bonds with carboxyls, as demonstrated by an affinity between indium and various carboxylic acids in Indium extraction [129 , 130].Both simulation studies and experimental results indicate that carboxyls on graphene are concentrated on edge domains [131, 132, 133].Compatible with the reported, a relatively higher concentration

of carboxyls on A-fMGs cross-section surface is evidenced. Here, Raman spectra in Figure 4.5 indicated a higher defect level of cross-section surface (surface B) of A-fMGs than that on a side-wall surface (surface A), corresponding to concentrating of fMG edges.

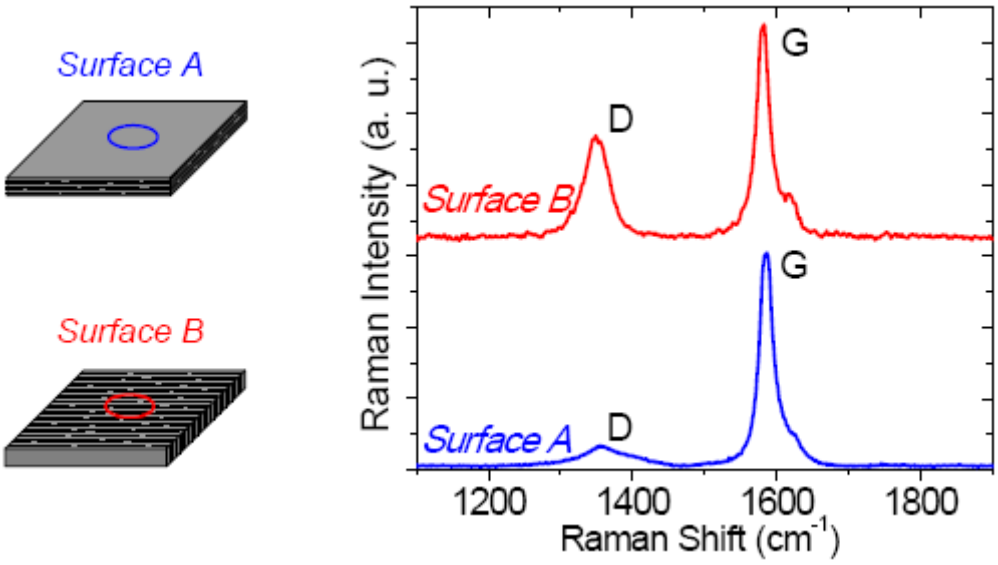

Figure 4.5 A comparison between Raman spectra of sidewall (surface A) and cross-section surface (surface B) of A-fMGs.

Low-resolution scanning XPS spectra in Figure 4.6 show a significantly higher concentration (~33.8%) of oxygen atoms on surface B than that (~17.7%) on surface A, as shown by a calculation in supporting materials according to the empirical atomic sensitivity factors for O1s and C1s (0.66 and 0.25, respectively) reported by Wagner *et al*.[111]. Moreover, high-resolution XPS spectra confirms a higher concentration of carboxyl on surface B, by giving a integrated area ratio (49:41:10) among conjugated carbon-carbon bonds (284.3 eV), carbon-hydroxyl bonds (285.3 eV), and carbonyl bonds (~288.4 eV) of surface B, compared with that (71:27:2) of surface A. Arrangement of VA-fMG TIMs can make a best use of carboxyls' aggregation on cross-section surface in

the joint between VA-fMGs and Indium as illustrated in Figure 4.7, resulting in reduced $R_{A-fMGs/In/Si}$ and improved adhesion to indium-coated Si substrates.

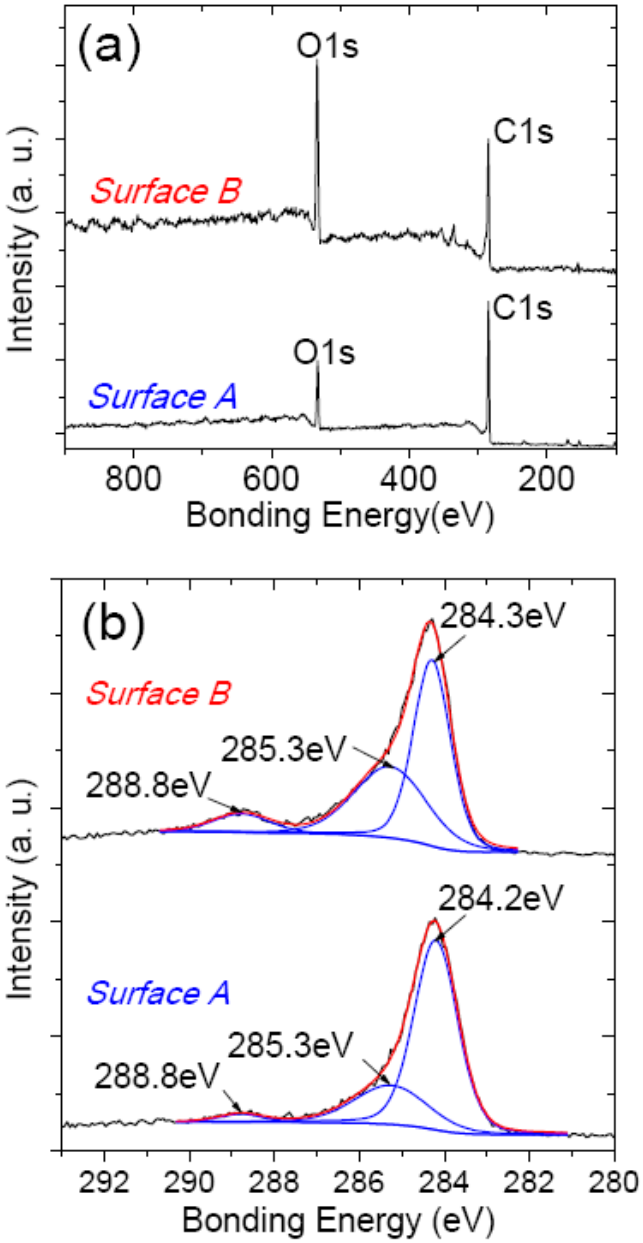

Figure 4.6 a) A comparison between low resolution scanning XPS spectra of surface A and B. b) A comparison of high resolution XPS spectra between surface A and B.

Second, it is noticed that metal's filling can dramatically increase contact surface area between metal and carbon nanomaterials and significantly contribute to an enhanced

adhesion. For example, filling open-ended carbon nanotubes with metals (*e.g.* Pd) has been substantially reported [134, 135, 136]. Zhu *et al* [137] reported that adhesion between metallic solder and carbon nanotubes is significantly improved by opening ends of vertically aligned carbon nanotubes. Here, compliant with a laminated structure shown in SEM images in Figure 3.9, a unique anisotropic wetting phenomenon of water indicates existence of micro-channels on cross-section surface of A-fMGs. As shown by Figure 4.7 and Methods, contact angle of deionated water on A-fMGs are measured in 3 geometries. Comparing to geometry **A** (contact angle is equal to 85.7º), geometries **B** and **C** give significant different contact angle values of 104.1º and 67.5º, respectively. In order to show the phenomena, water droplets must be influenced by two physical effects due to micro-channels on cross-section surface of A-fMGs along fMGs' orientation (X and Y directions in Figure 4.7a). On the one hand, existence of micro-channels increases surface roughness along Z direction, resulting in enlarged contact angle of water in geometry **B** by a "lotus effect", which has been observed on a super-hydrophobic surface from a patterned vertically aligned CNTs [138, 139].

On the other hand, capillary forces along thin micro-channels among A-fMGs and hydrophilic functionalizations on fMGs are responsible for a reduced contact angle in geometry **C**. In VA-fMG TIMs, cross-section surfaces of A-fMGs with micro-channels is right faced to Indium coated silicon substrates, facilitating filling of melt indium as shown schematically in Figure 4.7b. This can efficiently increase contact surface area between Indium and A-fMGs, resulting in an improved adhesion and reduced contact thermal resistance in VA-fMG TIM assembly.

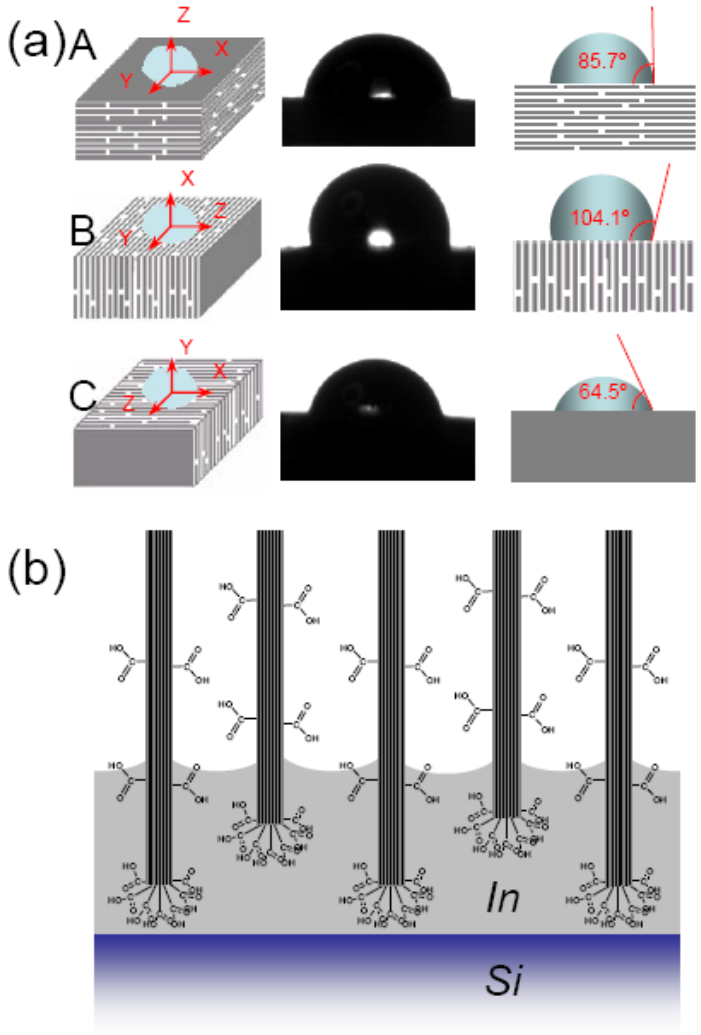

Figure 4.7 A VA-fMG TIM architecture facilitates a significant reduction of $R_{A\text{-}fMGs/In/Si}$. a) Contact angle measurements in 3 different three-dimensional geometries, as detailed in Methods. b) A schematic illustration of VA-fMGs/In/Si multiple interface junction.

4.5 Comparison with reported results

Graphene is a promising candidate in TIM application due to its extraordinarily high thermal conductivity (~ 5300W m^{-1} K^{-1} for suspended monolayer graphene [8] and ~600W m^{-1} K^{-1} for supported monolayer graphene [24]). However, large-volume heat dissipation requires a joint contribution of a large number of graphene sheets. Graphene sheets must be aligned in a large scale array in order to meet the requirements for TIM

applications. Valuable efforts have been paid on preparation of aligned graphene oxide (GO) by thermally reduced GO paper. However, in-plane thermal conductivity of GO and reduced GO (1.9 W m^{-1} K^{-1} and 0.14-2.87 W m^{-1} K^{-1}, respectively) is relatively low and unlikely able to meet demanding requirements in thermal management of current photonic and electronic devices. Moreover, toxic reduction agents (*e.g.* hydrazine) and high temperatures (400 to 1100^{o}C) applied in chemical or thermal reduction of graphene oxide are not preferred in real industrial applications. This work is an approach for alignment of reduction-free thermally conductive functionalized multilayer graphene in large scale. High electrical ($\sigma_{//}$, ~386 S cm^{-1}) and thermal conductivity ($k_{//}$, between 112 and 123 W m^{-1} K^{-1}) as well as ultra low CTE ($\alpha_{//}$, ~ -0.71 ppm K^{-1}) in in-plane direction of A-fMGs are obtained without aid of reduction process.

Moreover, graphene is usually recumbent on solid substrates, while vertically aligned graphene architecture on solid substrate is rarely available and less studied. However, for TIMs, electrodes of ultracapacitors, *etc*, efficient heat dissipation and electrical conductance in normal direction of solid surfaces is strongly desired [140].Significant advantages of a 3D vertically aligned fMG architecture in TIM application are demonstrated here. Equivalent thermal conductivity of VA-fMG TIMs can be almost two orders of magnitude higher than that of RA-fMG TIMs. Contact thermal resistance ($R_{AfMGs/In/Si}$) across A-fMGs/In/Si multiple interface in VA-fMG TIMs (5.1 mm^2 K W^{-1}) is significantly lower than that of RA-fMG TIMs (42.5 mm^2 K W^{-1}).

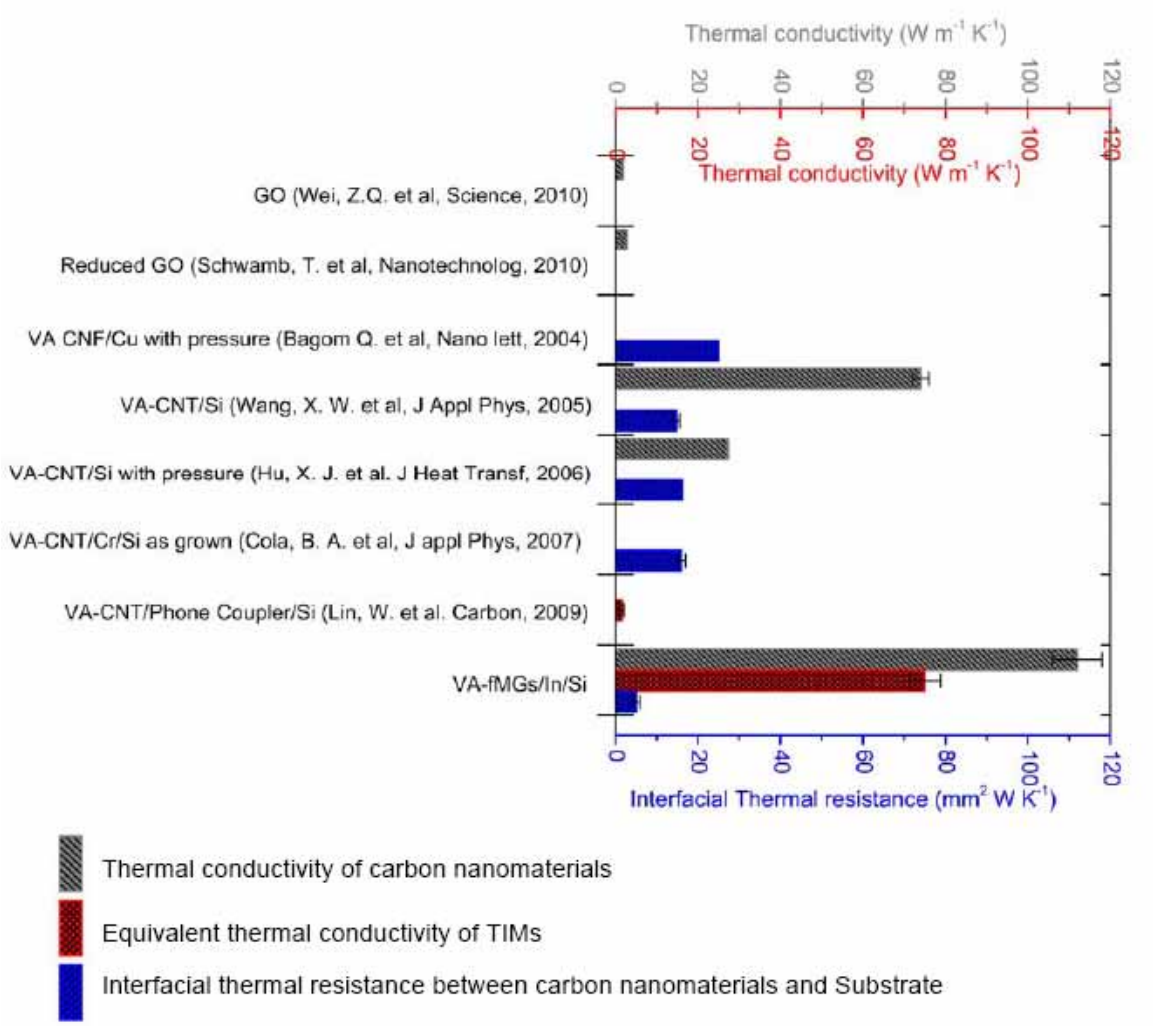

Figure 4.8A comparison of thermal conductivity of carbon nanomaterials, effective (equivalent) thermal conductivity of their TIMs, and contact (interfacial) thermal resistance between carbon nanomaterials and substrates in reported structures (ref.128, 21, 125, 63, 64, and 65) with results in this work.

Nevertheless, it is noticed that equivalent thermal conductivity of TIMs based on vertically aligned carbon nanotubes (CNTs) and carbon nanofibers (CNFs) is relatively low due to a high contact thermal resistance between CNTs/CNFs and substrates. Ngo *et al* [125] applied contact measurement techniques and obtained an interfacial thermal resistance of ~ 25 mm^2 K W^{-1} between a vertically aligned carbon nanofiber array and a copper substrate at an assembling pressure of 60 psi. Wang *et al* [63] used a photothermal

method and obtained absolute and effective thermal conductivity of a vertically aligned CNT (VACNT) array grown on Si substrate as ~27.3 W m^{-1} K^{-1} and ~0.145 W m^{-1} K^{-1}, respectively, as well as a thermal interfacial resistance of ~16.4 mm^2 K W^{-1} across a CNT/Cr/Si multiple interface. Hu *et al* [64] applied 3-omega measurements on an as-grown VACNT structure at 100kPa pressure, and reported an effective thermal conductivity of the CNTs array and contact thermal resistance between CNTs and Si as ~74 W m^{-1} K^{-1} and ~15 mm^2 K W^{-1}, respectively. Cola *et al* [65] reported that a contact thermal resistance between VACNTs and Si scales ~15.8 mm^2 K W^{-1} by photoacoustic characterization. Lin *et al* [66] applied molecular phonon couplers between VACNTs and Si and reported that an equivalent thermal conductivity of thus-prepared VACNT TIM structure measured by laser flash method is ~1.6 W m^{-1} K^{-1}. As illustrated in Figure 4.8, VA-fMG TIMs have high thermal conductivity and low contact thermal resistance, suggesting their promising potentials in current demanding thermal management for electronic and photonic devices.

4.6 Conclusions

Here, the novelty of the paper is exhibited by a breakthrough in handling a problem, which remains unresolved in previous studies for long time. For thermal interfacial materials (TIMs), electrodes of super-capacitor, *etc*, graphene is expected to be vertically stacked between/on solid surfaces for efficient heat dissipation and electrical conductance in normal direction of solid surfaces, as proven by results on vertically aligned CNTs and CNFs. However, direct growth of vertically aligned free-standing graphene on solid substrate is difficult and rarely available in current studies, bringing significant barriers in graphene's application. Here, we demonstrate a successful

preparation and great advantages in TIM application of vertically aligned fMGs over that are recumbent on solid substrates.

Moreover, interaction between graphene and substrates, e.g. Indium coated silicon wafer in the study, is significantly interested in current research of carbon-based thermal interfacial materials, as previous results indicated that adhesion between carbon-based material and metallic substrates is weak. Our study on vertically aligned fMG TIMs provide an approach to optimize adhesion to metal coated silicon wafer, which efficiently reduces thermal resistance across the graphene/metal/Si multiple interface. Based on all above, we believe the research is an answer to Dr. R. Prasher's questions in "Graphene spread the heat" (*Science* **2010**, *328*, 185-186.), as mentioned in Chapter 1.

The work hence can be summarized as efforts to prepare a 3D vertically aligned functionalized multilayer graphene architecture between silicon surfaces and an exploration of their application as TIMs. As show in former charpter, a high alignment efficiency of "reduction-free" conductive fMGs as evidenced by SEM and polarized Raman spectroscopy induces highly strong anisotropic CTE, electrical and thermal conductivity of A-fMGs. Vertically aligned fMG TIMs combined the benefit of fMGs of ultra-low CTEs, superior electrical and thermal conductivities of A-fMGs in normal direction of contacted solid surfaces. The measured high equivalent thermal conductivity up to 75.5 W m^{-1} K^{-1} and low thermal resistance cross VA-fMGs/In/Si interface (5.1 mm^2 K W^{-1}) of VA-fMG TIMs suggest their promising potentials not only in thermal management of electronic and photonic applications but also for other important applications of graphene such as electrode of ultra-capacitors and conductive fillers in polymer composites.

CHAPTER 5 DYNAMIC STUDY ON THERMAL OXIDATION DEGRADATION AND ELECTRICAL RESISTIVITY OF IN-SITU POLYMER AGEING SENSORS BASED ON CARBON BLACK FILLED EPOXY COMPOSITES

Previous researches indicated that polymeric insulation system breakdowns account for up to 40% failures of motors, aircrafts, and electrical generators. Environmental conditions including heat, light and oxygen usually facilitate thermal oxidation of polymeric materials. In addition, operational considerations may further increase temperature winding from unforeseen conditions including excessive load and reduced/blocked cooling [141]. In order to detect ongoing failures for predictive maintains, effective monitoring methods for real-time thermal oxidation aging status of polymeric components are desired and required by standards (*e.g*., ANSI/IEEE Std. 1974, 383, 1974).

However, aging status of polymer materials are difficult to detect and predict. Traditional approaches for the purpose include mechanical property measurements and chemical tests. However, these tests are destructive and retardant, preventing them from convenient *in-situ* monitoring actual aging status [142, 143] and usually resulting in inaccurate estimation of ongoing failures. This may cause either premature replacement of insulation materials and higher maintenance costs or unplanned shutdowns and worse reliability. Compared with these approaches, *in-situ* monitoring aging status of polymeric insulating materials by electrical methods has significant advantages such as convenient operations, accurate real-time data collections, low costs, *etc*. In former researches, we provided an approach for *in-situ* monitoring thermal oxidation status of polymeric materials [144,145, 146]. by electrical sensors based on conductive polymeric composites (CPCs). However, due to the absence of a systematic kinetic study, a direct relationship

between electrical resistivity of the sensors and aging conditions (*e.g.* aging temperature and aging time) remains unavailable, bringing significant barriers in their industrial application.

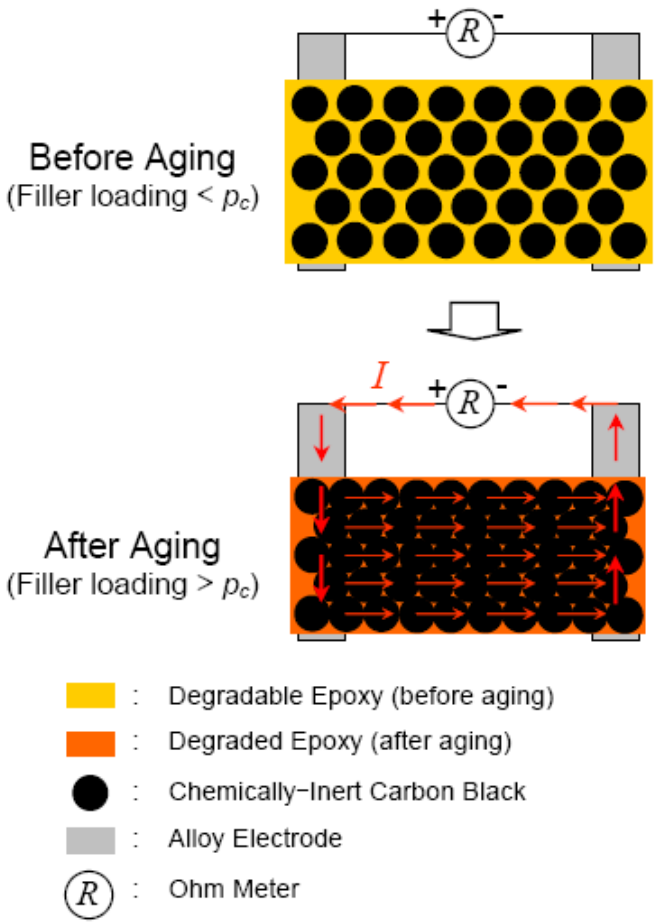

Figure 5.1 A schematic illustration of mechanism of *in-situ* polymeric aging sensor based on carbon black filled epoxy CPCs.

Electrical resistivity of CPCs is highly sensitive on volume or weight ratio (filler loading) of conductive fillers in polymer matrix, especially when filler loading is close to percolation threshold (p_c). Thermal oxidation aging usually can cause a significant weight loss of polymer matrix in a CPC system, resulting in a filler loading change which can be exhibited by a prompt alteration in electrical resistivity of CPCs, as illustrated in Figure 5.1. In this study, with an original filler loading slight smaller than percolation threshold, CPCs from carbon black (filler) and bis-phenol A type epoxy (polymer matrix) are

prepared and aged in air at temperature ranging from 180 to 280°C. Carbon black is found to chemically inert and can't be decomposed in the aging condition. In contrast, several degradation mechanisms during the aging processes such as chain scission, loss of volatile fractions, and oxidation reactions, are accounted for a significant weight loss of bis-phenol A type epoxy [147, 148, 149, 150]. Therefore, during aging, filler loading of the carbon black filled epoxy composites is continuously increasing to approach and exceed percolation threshold consequently, resulting in a dramatic change in electrical resistivity. Here, weight loss of bis-phenol A type epoxy is analyzed by Thermogravimetric Analysis (TGA) in order to quantify influence of thermal oxidation aging temperature and time. Moreover, it is found that electrical resistivity of sensors from the CPCs as a function of aging time at constant aging temperature is in a good agreement with a Boltzmann-Sigmoidal equation. Based on the finding, the sensors show their capability of *in-situ* in-situ monitor and estimate aging status of polymeric components by a fast and convenient electrical resistance measurement.

5.1 Experimental

5.1.1 Materials

A commercial grade Bis-phenol type epoxy (EMD Chemical Inc.) is applied as a matrix resin in the polymer-base carbon black composite materials. Thermogravimetric analysis (TGA) tests showed that 5% and 10% weight loss temperature in air of the applied epoxy are 288ºC and 348ºC, with a temperature raising rate of 10 ºC /min, respectively. Carbon black XC-72R is obtained from Cabot Corp. USA. Adsorption numbers of dibutyl phthalate (DBP) of the carbon black is 143 m^2/g. TGA test showed 5% weight loss temperature in air of the carbon black sample is 603.8ºC with a temperature raising rate of 10 ºC /min.

5.1.2 Preparation of Epoxy/Carbon black composites

A mixture of carbon black (8 wt%) and epoxy resin was mixed. 3 Different mixing procedures are applied in obtaining 3 batches of sample with different mixing: (A) The mixture of carbon black and epoxy resin is mixed at room temperture. Then, the mixture is heated to 140 ºC for 1hours, cured at 160 ºC for 8hours, and postcured at 200 ºC for another 4 hours. (B) The mixture of carbon black and epoxy resin is mixed at room temperture. Then, the mixture is heated at 130 ºC for 3.2hours, cured at 160 ºC for 8hours, and postcured at 200 ºC for another 4 hours. (C) The mixture of carbon black and epoxy resin is mixed at room temperture. Then, the mixture is heated at 140 ºC for 0.75 hours, cured at 160 ºC for 8hours, and postcured at 200 ºC for another 4 hours.

5.1.3 Fourier-Transform Infrared (FTIR) measurement

Fourier-Transform Infrared (FTIR) Spectroscope (Nicolet, Magna IR 560) was used to study chemical structure changes with ageing time. Epoxy resin is coated on a silicon wafer and cured at 160 ºC. After being aged at 260 ºC in a convection oven, the coated silicon substrate was tested at a transmittance mode in FTIR spectroscope with wave numbers ranging from 600 to 4000cm^{-1}.

5.1.4 Thermogravimetric analysis (TGA) measurement

A thermogravimetric analyzer (TA Instruments, Model 2050) was applied to characterize the thermal stability of the aged sensor specimens. In a typical isothermal TGA test, a 10 mg specimen is placed into a platinum pan, heated up with a ramp rate of 30ºC/min from ambient temperature to aim temperature, and isothermally weighted for 20hour in air atmosphere. In a typical dynamic test, temperature of specimen is raised with a ramp rate of 10ºC/min from ambient temperature to 800 ºC in air atmosphere.

5.1.5 Thermal Mechanical Analysis

Shrinkage behavior of the epoxy/carbon black composite sample was studied on a thermo-mechanical analyzer (TMA, TA Instruments, Model 2940). The composite samples were aged in the TMA furnace in air atmosphere at 210, 220, 240 and 260 ºC, respectively.

5.1.6 Electrical Resistivity measurement

Alloy electrodes were embedded into samples of a geometric dimension of 20mm×6mm×0.25mm (length×wildth×thickness). Electrical resistances of CPCs are tested by a Keithley 485 picoammeter with a HP 6353A DC power supply. Electrical resistivities are obtained by calculation with the measured electrical resistance and dimensions. Electrical resistance is also directly measured by a multi-meter (Fluck 289).

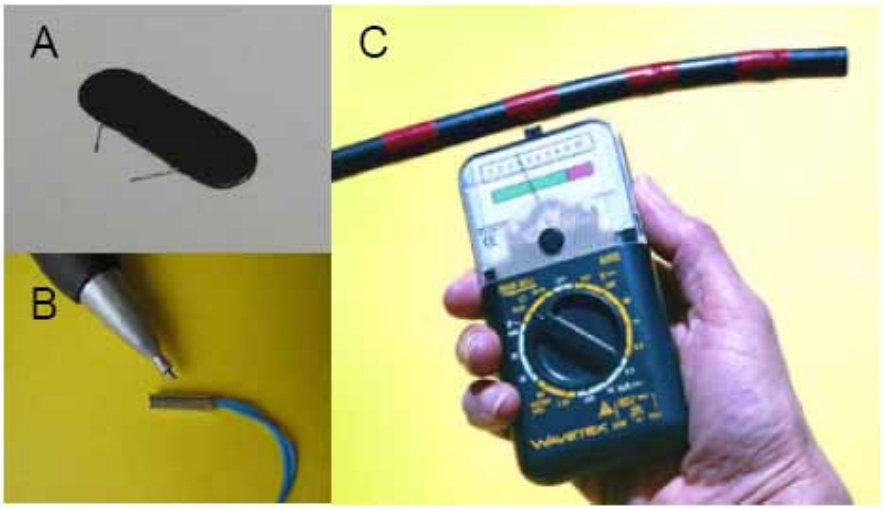

Figure 5.2 In-situ polymeric aging sensor based on carbon black filled epoxy CPCs. (A). CPCs from carbon black filled bisphenol A type epoxy with electrode. (B). A packed sensor based on the CPCs with a low profile. (C). A convenient electrical measurement of sensors imbedded in polymeric insulation coating of cords.

5.2 Results and discussion

5.2.1 NMR measurement

NMR measurements were operated on a Mercury 300 NMR. The solvent in the measurement were chose as Chloroform-d with 0.05% Tetra-methyl silicone (TMS). In

the measurement, the mixture of epoxy resin used in the study was solved in chloroform-d, and the spectra were shown by Appendix A and Table 5.1.

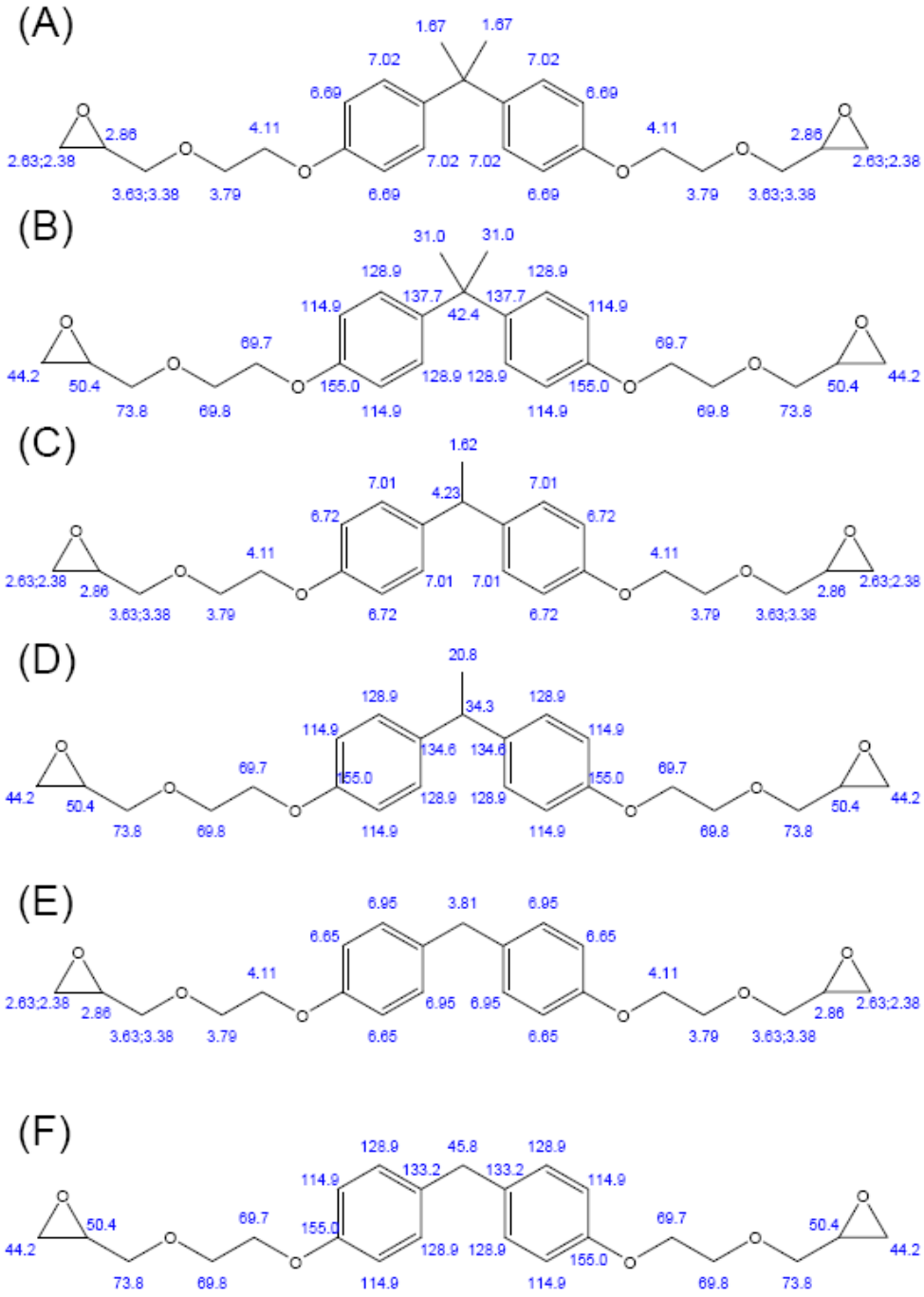

Figure 5.3 A schematic illustration of chemical shift of H and C atoms in ^{1}H-NMR and ^{13}C-NMR of bisphenol type epoxy. (A) ^{1}H-NMR of Bisphenol A epoxy. (B) ^{13}C-NMR of Bisphenol A epoxy. (C) ^{1}H-NMR of Bisphenol E epoxy. (D) ^{13}C-NMR of Bisphenol E epoxy. (E) ^{1}H-NMR of Bisphenol F epoxy. (F) ^{13}C-NMR of Bisphenol F epoxy. (by Chemoffice 2003/ChemNMR estimation)

Table 5.1 Protocol of ^{1}H-NMR measurement of epoxy resin before aging.

Chemical shift (ppm) from ^{1}H-NMR	Character
7.09	Double peak (d), 2H
6.75	Double peak (d), 2H
5.90	Multi peak (m), 3H
5.45	Multi peak (m), 2H
4.10	Multi peak (m), 6H
3.59-3.20	Multipeak(m), ~20H
2.89	Multipeak(m), 2H
2.73-2.58	Multipeak(m), 8H
2.14	Single peak(s), 30H
1.61-1.77	Double peak(d), 10H
1.38	Double peak(d), 3H
0.88	Double peak(d), 8H

As can be seen from Figure 5.3 and Table 5.1, actual measured peaks corresponded to the protocol of Bisphenol type epoxy very well. The single peak around 2.14ppm showed obvious sign that Ar–C$(CH_3)_2$-Ar group exists. According this, the NMR measurement can tell us that Bis-phenol A type epoxy resin may exist. More details also was discovered when the epoxy resin mixture is separated and NMR tests of separated parts are finished.

5.2.2 Molecular structure degradation

Fourier Transform Infra-Red (FTIR) spectra

In order to study chemical structure changes of epoxy resin during ageing process, FTIR measurements were conducted on epoxy resin specimens aged at 260 ºC in air atmosphere for 0, 2, 4, 27, 42, 250 and 500 hours, respectively. As it can be seen from

Figure 5.4, in the spectra of the epoxy resin before ageing process (0h), peaks at ~3469 (bonded –OH), ~2957 and 2865 cm^{-1}(C-H), 1605 and 1506 cm^{-1} (benzene ring), and 827 cm^{-1} (residual epoxide groups) are corresponded to the original chemical structures of bis-phenol A type epoxy resin. As the ageing time increases, the peaks at 3469, 2957, and 2865 cm^{-1} became weaker and almost disappeared after 42 hours, indicating hydroxyl groups and C-H bonds degraded at the early stage of the ageing process. These can be accounted for weak thermal stabilities of the hydroxyl groups and C-H bonds.

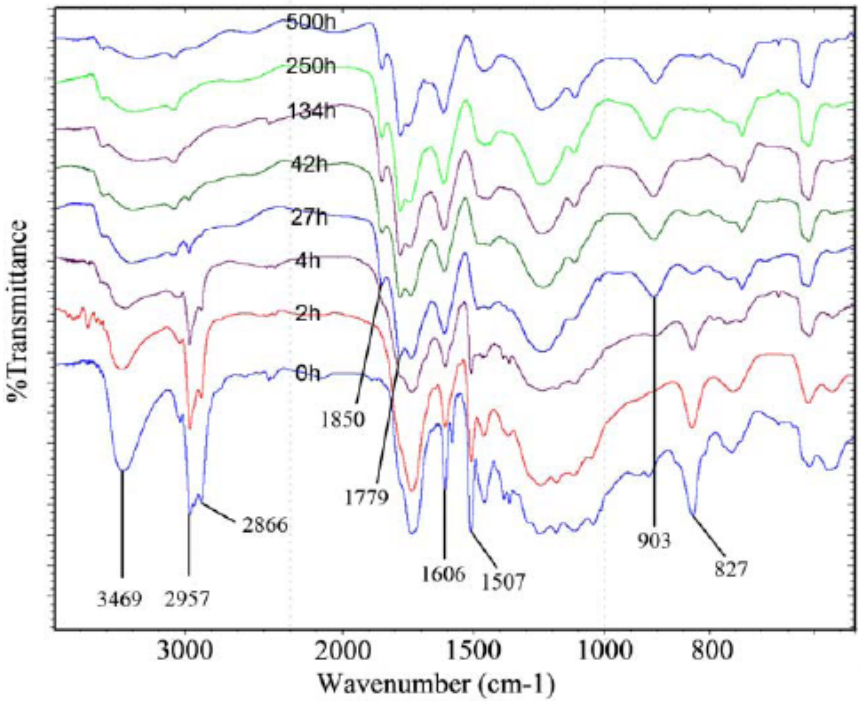

Figure 5.4 FTIR spectra of samples with different ageing time at 260 ^{o}C for 0, 2, 4, 27, 42, 250 and 500 hours.

In contrast, residual epoxide groups in the epoxy resin can react with a nearby hydroxyl group, confirmed by the disappearance of peaks at 827 cm^{-1}. Moreover, it can also be found that new peaks appeared at 905 cm^{-1}(C=C) at 260 ºC for 27 hours during ageing. This phenomenon is due to the fact that more unsaturated carbon atoms (sp^2 carbon) generated in the main chain of epoxy resin after the degradation of the hydroxyl groups and C-H bonds.The rigidity of an epoxy molecular structure can be increased in due to more sp^2 carbons in the main chain.

Thermogravimetric analysis (TGA)

Thermal-oxidation ageing significantly affects the molecular structures of the polymer matrix. These can also result in changes in their thermal stability, which can be characterized by TGA dynamic tests. In the study, epoxy resin samples were aged at 260ºC in air for 0, 2, 5, 8, 28, 56, 79 and 720h, and tested afterwards by a TGA dynamics measurement at a temperature raising rate of 10 ºC /min from room temperature to 800ºC. As can be seen in Figure 5.5, the epoxy-based polymer matrix shows a significant increase in thermal stability with extended ageing time. After ageing, the higher rigidity due to more sp^2 carbon on the main chain can bring higher thermal stability [151]. Although moiety in the main chain can be broken due to the weak thermal stability, resulting in the reduction in the thermal stability, however, for epoxy resin, which is a well known amorphous cross-linking polymer materials, the local breakage of net-work only have limited impacts on the thermal stability, comparing to linear polymer structure.

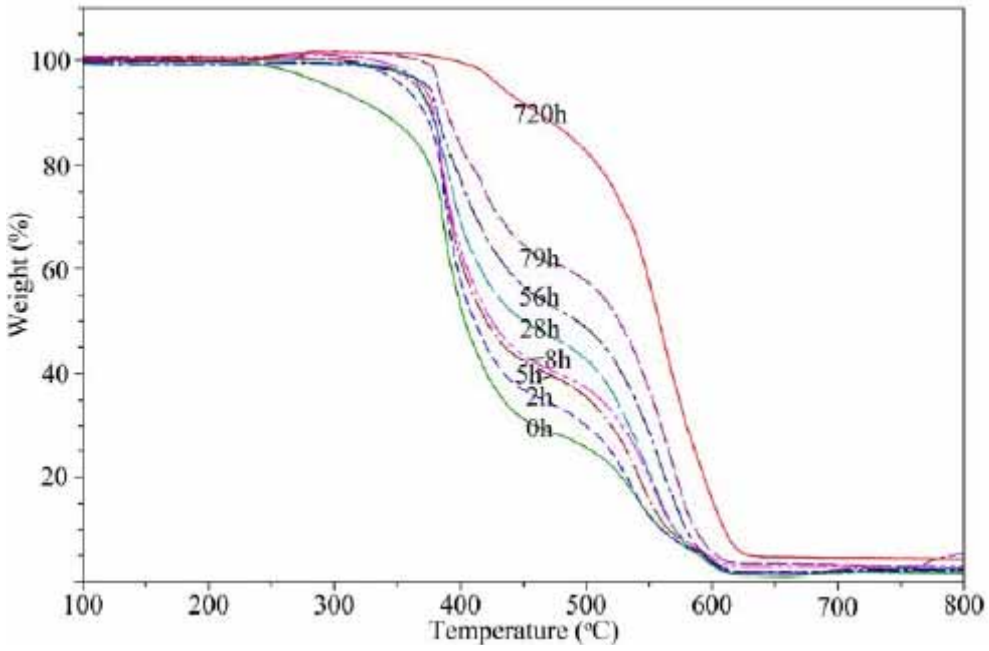

Figure 5.5 TGA measurements of samples aged at 260 °C in air for 0, 2, 5, 8, 28, 56, 79 and 720h.

In contrast, carbon black is very stable in the applied aging environment (temperature <300 ºC in air). In Figure 5.6 (inset), a dynamic TGA test showed 5% weight loss temperature in air of the carbon black sample is 603.8ºC. Moreover, an isothermal TGA test is carried out in air at 280 ºC for 720min, results in Figure 5.6 indicates the no significant weigh loss in the process. This indicates that carbon black does not decompose at temperatures (180-280ºC) applied in the thermal oxidation.

The results confirm that chosen materials satisfy the presupposition of our design that epoxy matrix of composite should be thermally degradable which conductive filler is chemically stable.

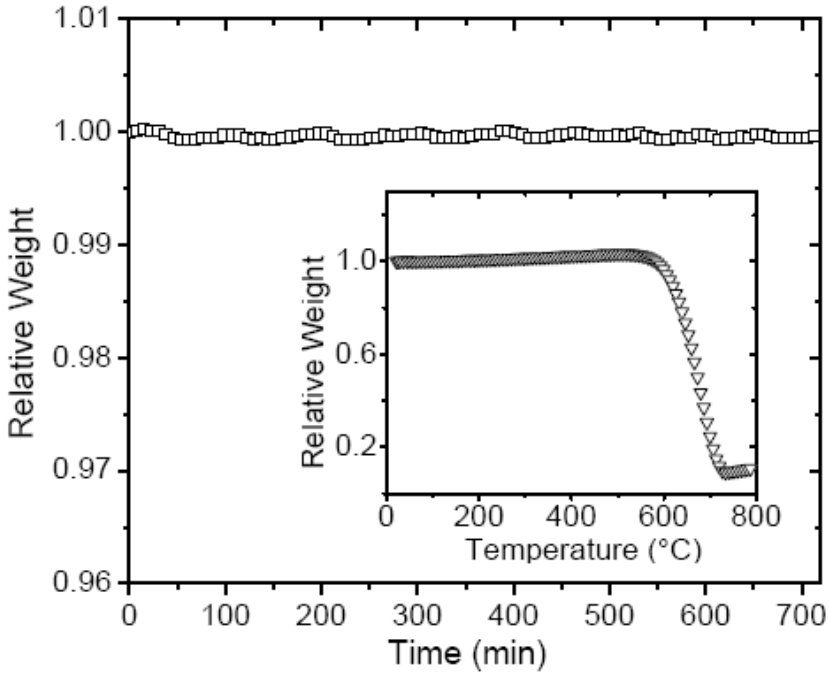

Figure 5.6 TGA measurement of Carbon black, isothermal at 280 ºC for 720min, inset is a dynamic scanning TGA measurement of Carbon black with a ramp rate of 10ºC/min from ambient temperature to 800 ºC in air atmosphere

5.2.3 TGA-MS measurement

A Q500 thermogravimetric Analyzer made by TA Instruments and a mass spectrometer were applied in TGA-MS measurement. In the test, furnace temperature

was raised at a constant rate of 10 ºC /min, and the volatiles generated in the process were transported by environment gas to mass spectrometer. Mass spectrometers consist of three basic parts: an ion source, a mass analyzer, and a detector system. The stages within the mass spectrometer are production of ions from the sample, separation of ions with different masses, detection of the number of ions of each mass produced and collection of data to generate the mass spectrum, as show below.

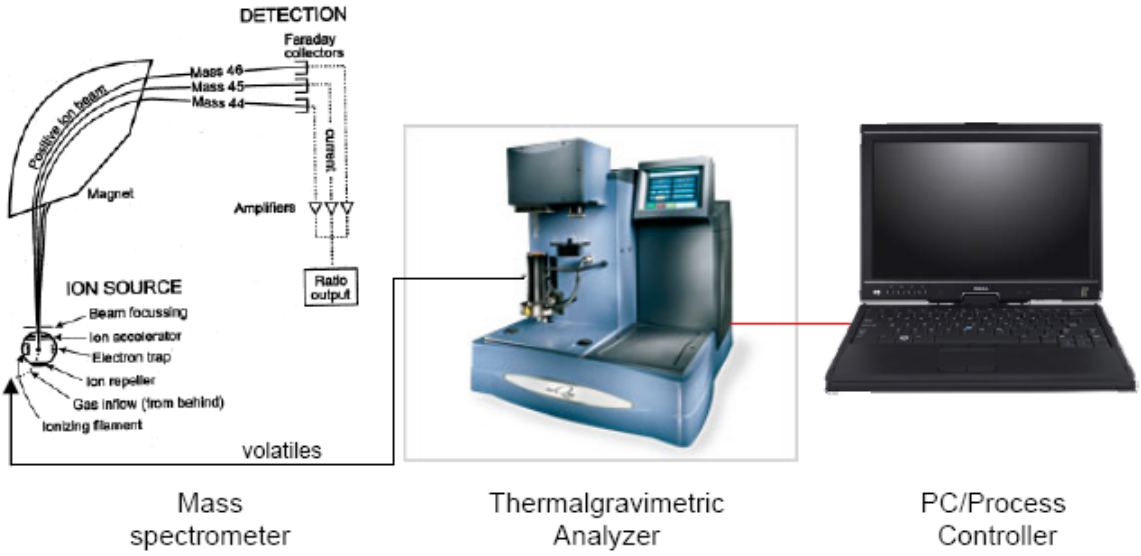

Figure 5.7 A schematic illustration of TGA-MS measurement

The mass spectrometer tested the composition of volatiles cycle by cycle. In this study, the temperature region and number of cycle were chose as 30 ºC -900 ºC and 68, respectively. Both TGA and MS data are obtained from TGA-MS measurement carried on an instrumental system shown in Figure 5.7. In the measurement, charged particles with different m/z values were identified by points with different color and shape. The intensity of ion current and number of cycle were corresponded to the amount ratio of charged particle and test time (or temperature), respectively.

Moreover, gives TGA data from TGA-MS measurement, respectively. It can be seen that the weight residue vs temperature curve drop rapidly in the temperature region from 330 ºC to 430 ºC. This also means that significant degradation behavior happened in

this region. Naturally, mass spectra from the 26th and 27th cycle, which are corresponded to 339.3 and 352 ºC, were mostly interested and shown by Figure 5.9.

In these spectra, peaks with m/e values of 14, 28 are believed to be corresponded to N_2, which widely exists in air. And peaks with m/e values of 32, 42 and 44 can be corresponded to O_2, CH_2CO and CO_2. The possible chemical structure of peaks with m/e values of 91 and 108 can be $C_7H_7^+$ (or C_6H_5N) and HO- $C_7H_7^+$(or HO-C_6H_5N). The result will be considered systematically with other measurement such as NMR and FTIR.

Thereby, molecular structure characterization of the epoxy resin can be summarized as follows.

a. TGA-MS measurement showed that CH_2CO, $C_7H_7^+$ (or C_6H_5N) and HO-$C_7H_7^+$(or HO-C_6H_5N).

b. NMR measurement showed that Bis-phenol type epoxy stucture

c. Q-DSC and TGA results indicated that chemical structure in the resin become more rigid after aging.

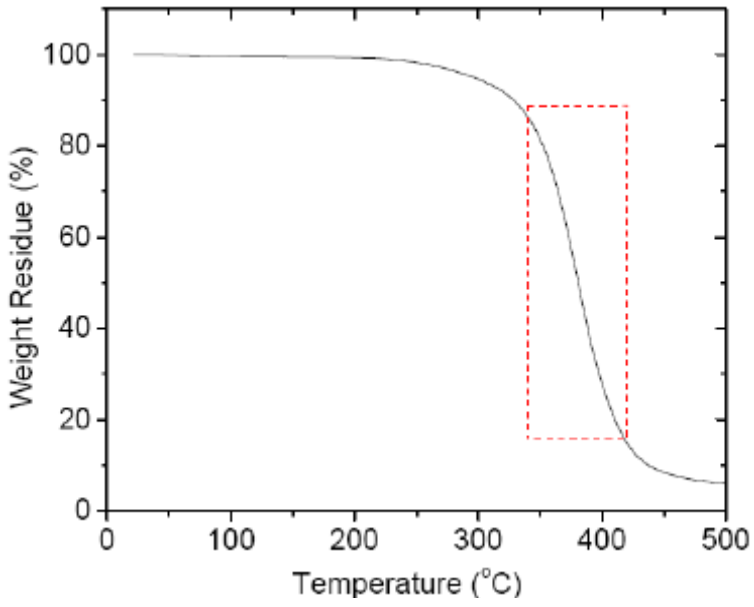

Figure 5.8 TGA data from TGA-MS measurement.

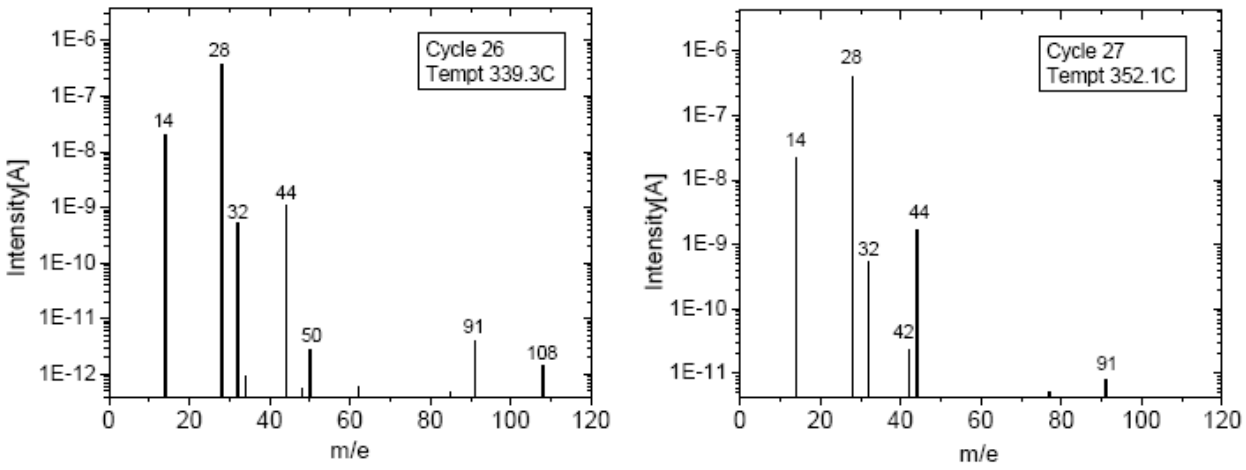

Figure 5.9. TGA data from TGA-MS measurement. Mass spectra from the 26th and 27th cycle, which are corresponded to 339.3 and 352.1C, respectively.

5.2.4 Q-DSC measurement

In order to obtain more reliable data from DSC measurement, Q-DSC was applied. In the tests, the polymer composite samples were heated to 250 ºC first to get rid of thermal history, and then heat flow vs temperature curves were obtained at a constant heat rate of 5 ºC /min.

As shown by Figure 5.10, T_g values of aged samples increased, showing that chemical molecular structure of the epoxy resin become more rigid. The possible reasons can be summarized as follows

1. There are two kinds of blocks in the polymer chain, the soft part and rigid part. The soft part are more easier to be destroyed by heat.
2. The filler loading of carbon black increased after aging, which also help to increase the T_g value.

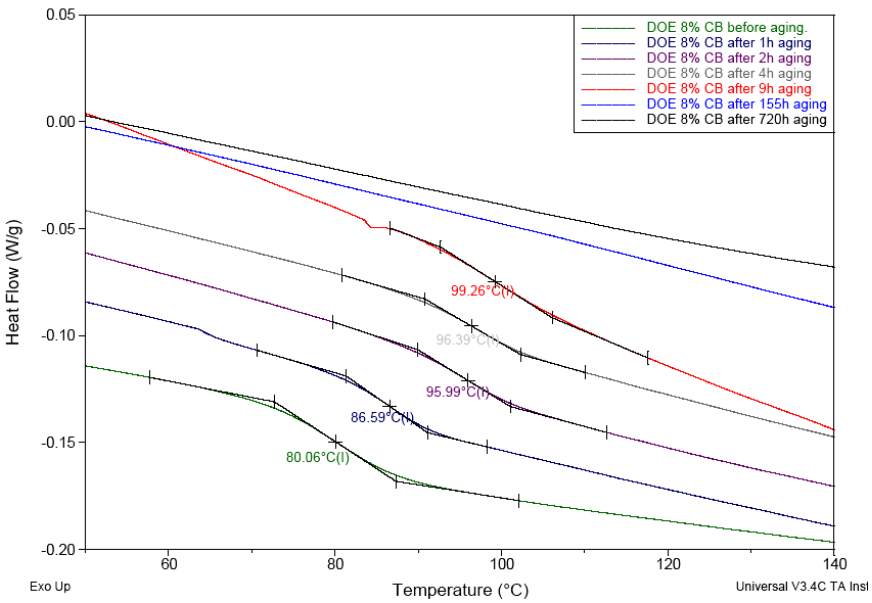

Figure 5.10 DSC measurement of samples with different aging time.

5.2.5 Shrinkage

Shrinkage may significantly affect the electrical resistance of the sample during the ageing process, due to degradation and weight loss of polymer matrix. TMA tests were applied to test the shrinkage behavior of the samples during the ageing process. As can be seen from the Figure 5.11, samples aged at different temperatures and atmospheres have different shrinking rates. It is also found that there are 2 stages in the TMA curves. At the beginning of the ageing procedure, there are rapid shrinkages which are responsible to the thermal history and release of residue internal stress. After that, the shrinkage rates tended to be more stable. The higher ageing temperature gave rather the higher shrinking rate. Moreover, at the same temperature, samples aged in air showed rather higher shrinking rate than that aged in nitrogen. Oxygen in air led to higher degradation speed of a polymer matrix, resulting in larger shrinking rates.

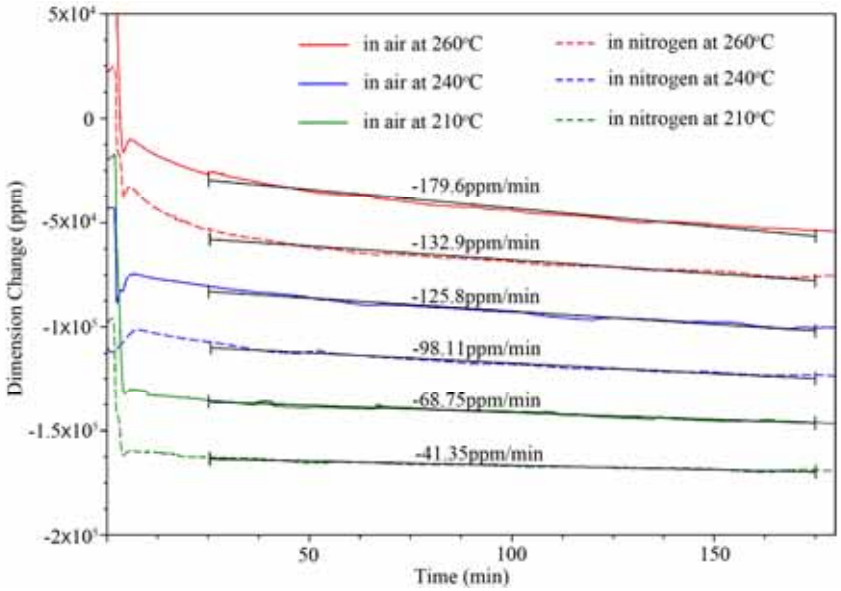

Figure 5.11 Shrinkage of the Epoxy/Carbon Black (8wt%) sample at different ageing temperature and atmosphere.

5.2.6 Weight loss of polymer matrix

In this study, in order to in-situ monitor and predict the thermal oxidation of the polymeric insulation materials, the relationship between ageing time and electrical resistance of the sensors is significantly important. In the thermal oxidation process, volume occupied by polymer matrix in the sensors decreases due to the decomposition of epoxy resin. In contrast, carbon black does not decompose at temperatures (<300 ºC) applied in the thermal oxidation, so that its volume ratio in the sensor increases. In this research, we applied a widely accepted power equation to obtain weight changes of the polymer matrix in the degradation reaction [152], as shown by equation as follows.

$$\frac{dC}{dt} = -k[C]^n \qquad \textbf{Equation 5.1}$$

$$C = \frac{W}{W_0}$$

$$k = Ae^{\left(-\frac{E_a}{RT}\right)} \qquad \textbf{Equation 5.2}$$

$$C = \left[1 - k(1-n)t\right]^{\frac{1}{1-n}} \qquad \textbf{Equation 5.3}$$

Where *t, C, W, W_0, k, n, E_a* and *R* represent ageing time, weight ratio of epoxy resin, real-time weight of epoxy resin, original weight of epoxy resin, reaction constant, an exponent of the power equation, active energy and Planic constant respectively.

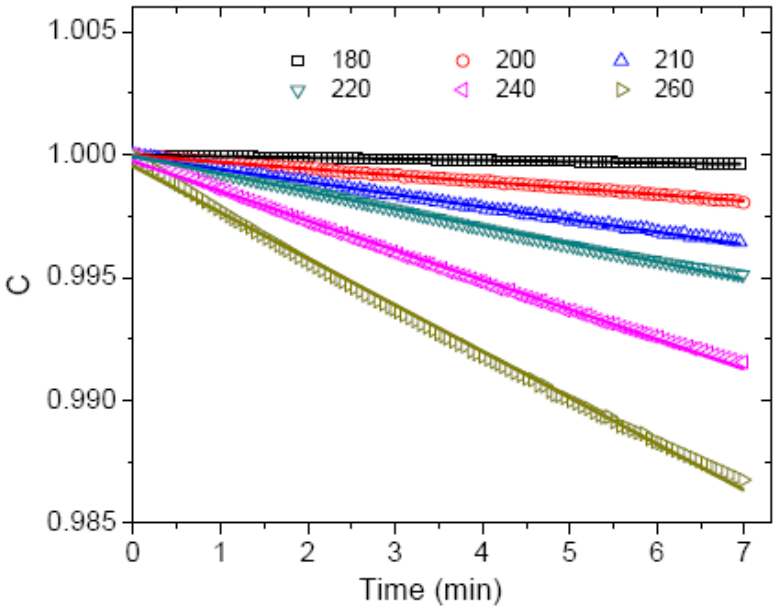

Figure 5.12 Weight loss of the bis phenal A epoxy sample at ageing temperature of 180, 200, 210, 220, 240, and 260°C.

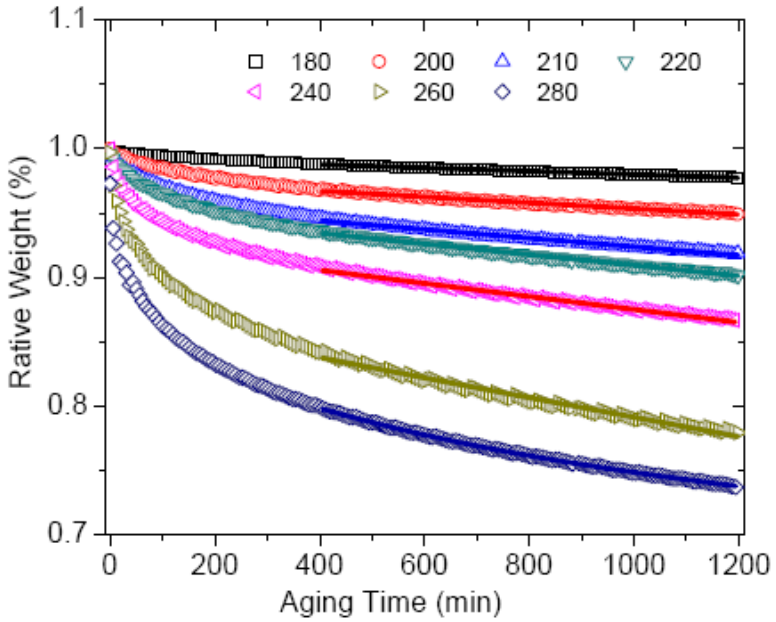

Figure 5.13 Non-linear fitting of weight loss of the bis phenal A epoxy sample at ageing temperature of 180, 200, 210, 220, 240, 260 and 280ºC (conducted on OriginPro 8.0).

As can be seen from Figure 5.12, relative weight of pure bis phenol type epoxy are tested by TGA isothermal mode and plotted as a function of ageing time. The tests are conducted at 180, 200, 220, 240, 260 and 280ºC. As shown by the solid lines in Figure 5.13, the experimental data are well fitted by a power equation with the aid of non-linear fitting conducted on OriginPro 8.0. Exponent (n) of power equation is found to be equal to 0.8408, confirming the well known first order reaction mechanism in polymer degradation process well [153]. Reaction constant for each temperature are obtained from non linear fitting in Figure 5.13. As shown by Figure 5.14, the values of *ln (k)* are plotted as a function of *1/T*. The quite good linear relationship between values of ln(k) and *1/T* confirms our assumption that the relative weight of polymer matrix follows a power equation well. According to Equation 5.2, the slope of the line can be considered as $-\frac{E_a}{R}$. By calculation, the active energy (E_a) of the degradation reaction are found to be equal to 85.48kJ/mol.

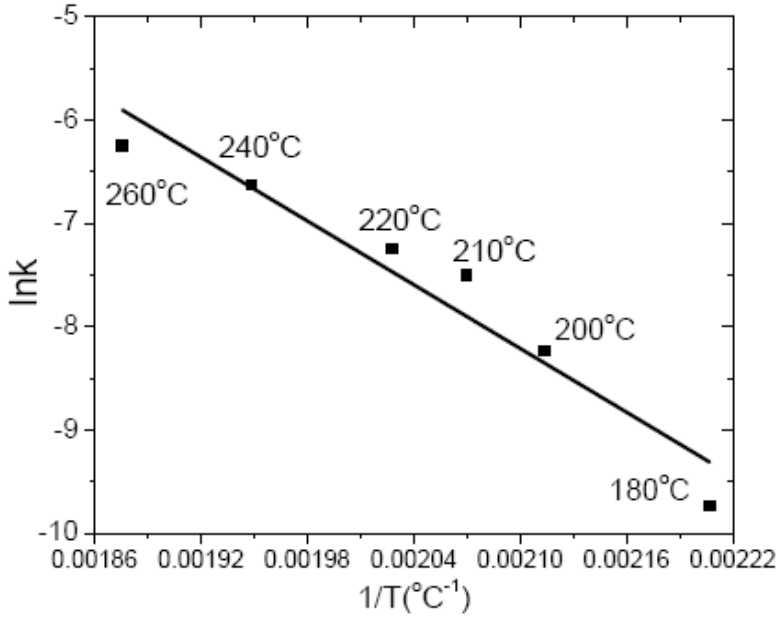

Figure 5.14 Linear relationship between ln(k) and 1/T.

5.2.7 Electrical resistivity

Liang *et al* studied the relationship between electrical conductivity and percolation theory of polymer based conductive materials [154]. Based on their theory, the relationship between the electrical resistivity of the carbon black/epoxy composites and filler loading near a percolation point can be expressed in Figure 5.15 and Equation 5.4 as follows:

$$\frac{\rho_2}{\rho_1} = (x_1 - x_2)^{\alpha}$$
$$\log(x_1 - x_2) = \frac{(\log \rho_2 - \log \rho_1)}{\alpha}$$

Equation 5.4

Where ρ, x and α represent the resistivity, volume concentration of carbon black, and exponent, respectively. And the numbers "1" and "2" in the subscripts represent two different statuses.

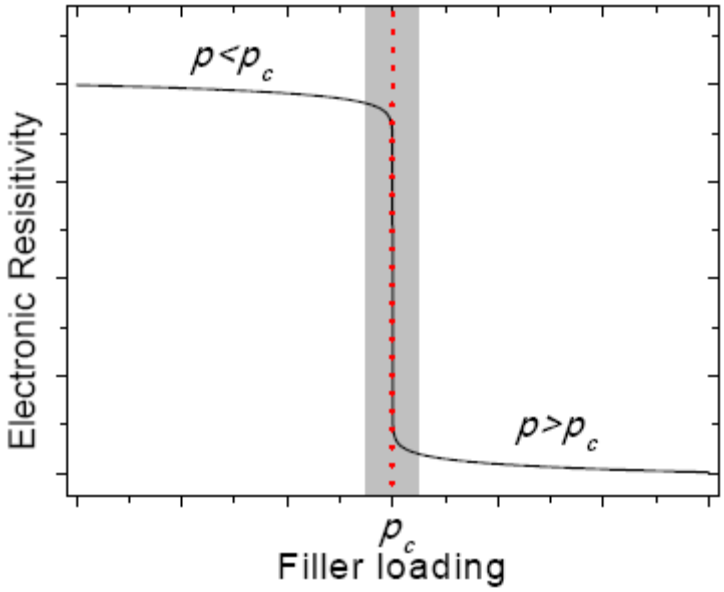

Figure 5.15 A illustration of electrical resistivity of CPCs. In shaded region, electrical conductivity of CPCs is highly sensitive to volume loading of conductive fillers.

The resistance of the sample can be considered as a function of ageing time, as follows

$$\log \rho = \frac{\log(\rho_0) - \log(\rho_\infty)}{\frac{\log(x_\infty - x_0)}{\log(x_\infty - x)}} + \log(\rho_\infty)$$

Equation 5.5

Moreover, volume concentration of carbon black can be expressed as a function of ageing time, as shown by.

$$x = \frac{x_0}{x_0 + (1 - x_0)C} \approx \frac{x_0}{C} \qquad \textbf{Equation 5.6}$$

In our model, the resistivity data were fitted by the following Boltzmann equation, as can been seen from following Equation and the approximations shown in appendix.

$$\log \rho = \frac{\log(\rho_0) - \log(\rho_\infty)}{1 + e^{\frac{\log t - \log t_c}{\Delta t}}} + \log(\rho_\infty)$$
$$\Delta t = \log e = 0.4342 \qquad \textbf{Equation 5.7}$$
$$\log t_c = -\log\left[\frac{A x_0}{2.303(x_\infty - x_0)\log(x_\infty - x_0)}\right] + \frac{E_a}{2.303RT}$$

Where the subscripts 0 and ∞ represent the states of the epoxy/carbon black composites before ageing and after infinite long time degradation, respectivley.The induction time, t_c, is corresponding to ageing time needed for a change of $\log(\rho)$ from $\log(\rho_0)$ to $[\log(\rho_0) + \log(\rho_\infty)]/2$.

However, t_c is only sensitive to ageing temperature and intial filler loading, but not dependent on initial resistivities of the carbon black filled composite samples. Here, in order to verify the theoretial deduction, three batches of samples from different preparation methodologies are applied. Although the filler concentrations of all samples are fixed at 8wt%, initial electrical resistivities of samples from are distinct due to different filler dispersion situtations induced in mixing procedure. SEM images, as can been seen in Figure 5.16, indicated the significant difference in filler dispersion situation among the 3 batches of samples. Dispersion of carbon black in batch A is much better than that in batch B and C, corresponding to their much higher initial electrical resistivity in electrical measurement.

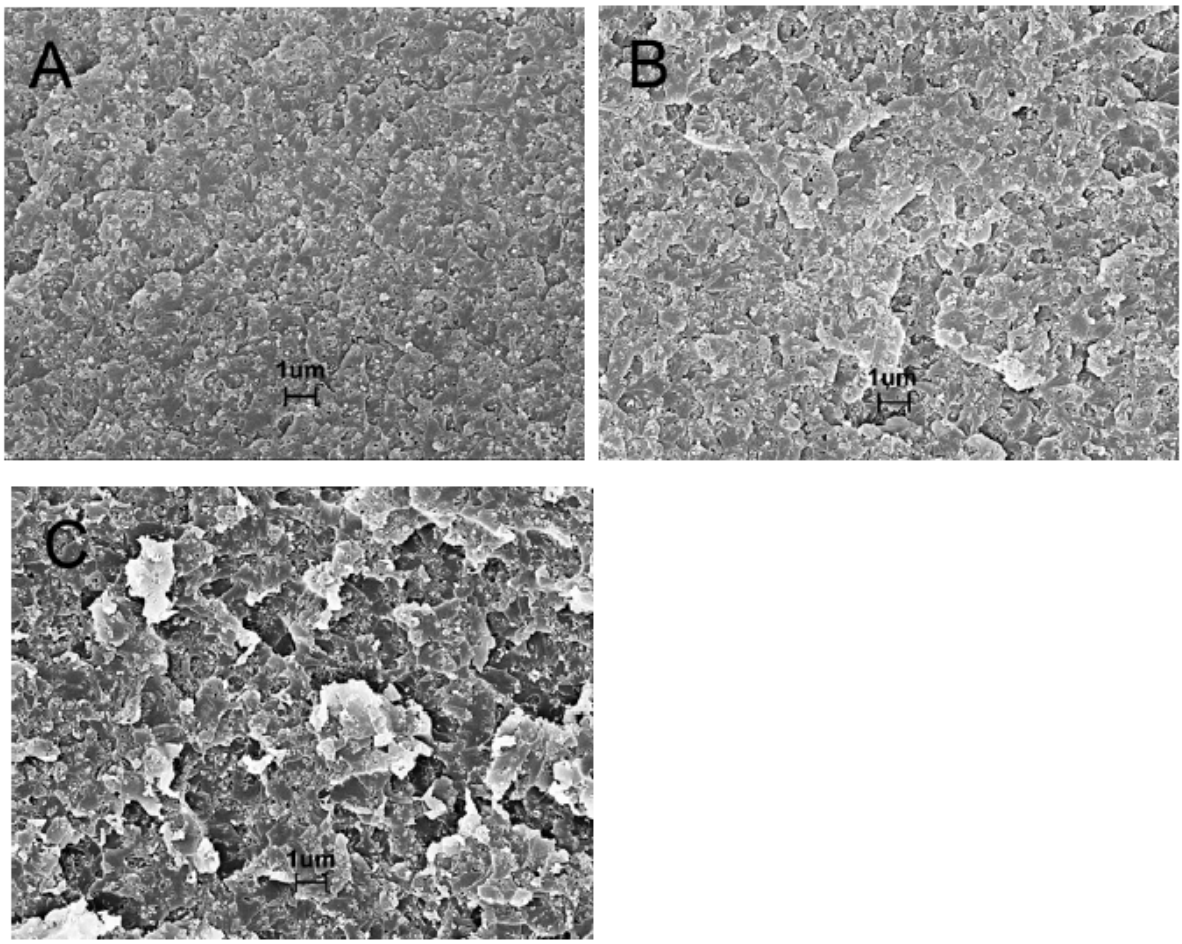

Figure 5.16 SEM images of samples from different preparation procedures with same filler loading (8wt%). A: Batch A; B: Batch B; C: Batch C.

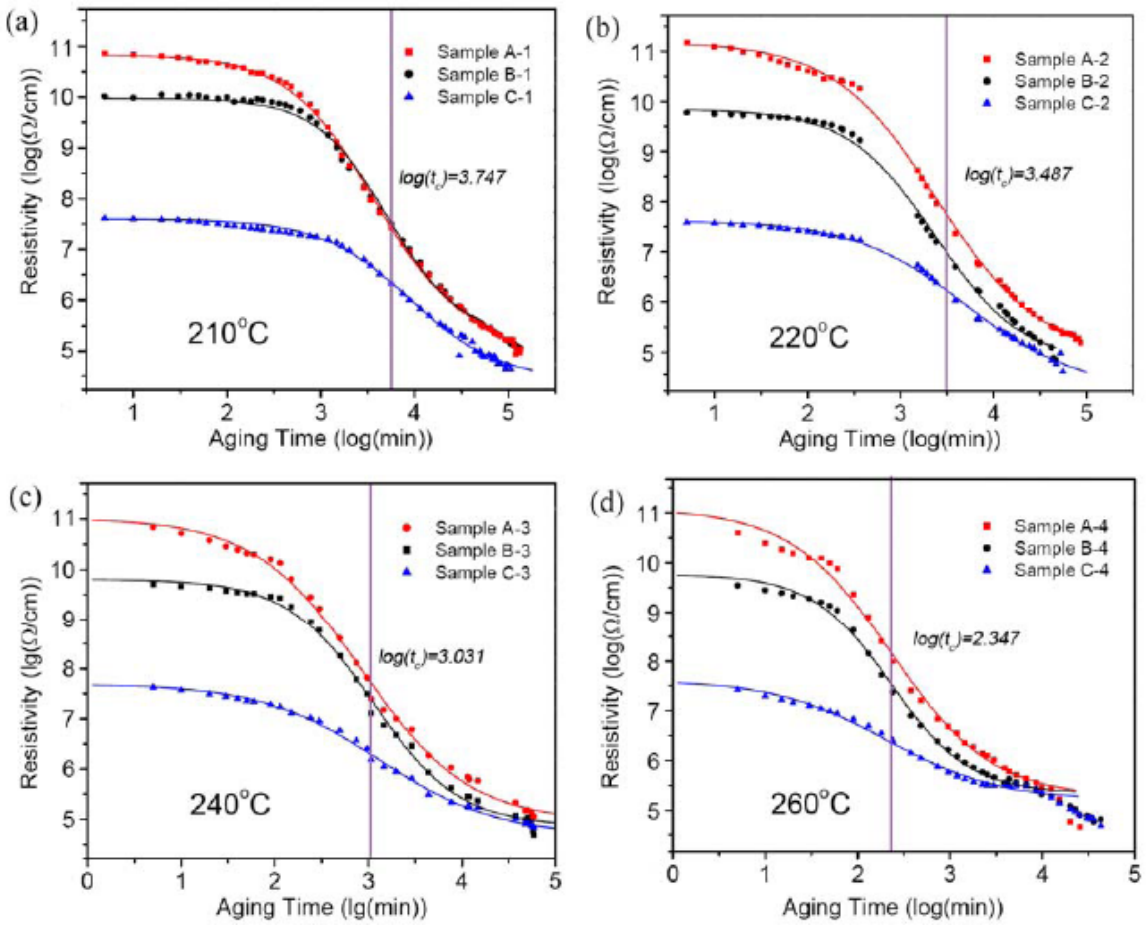

Figure 5.17 Electrical conductivity of the Epoxy/Carbon Black composites aged at (a) 210°C, (b) 220° C, (c) 240°C and (d) 260°C, where dots and lines represent the experimental data and fitting results respectively.

The carbon black/epoxy resin samples are aged in convectional oven in air and their electrical resisitivity are tested. As can be seen from Figure 5.17, the experimental data of resistivity of epoxy/carbon black composites are fitted by a Boltzman equation. From the obtained parameters from Boltzmann fitting of resistance vs. ageing time curves listed in

Table **5.2**, an interesting phenomenon can be found. Although the three different samples for respective ageing temperatures showed variations in initial resistivity values, they showed similar $log(t_c)$ values with a small diversion, confirming our model very well. As a relatively inert material, carbon black does not decompose at temperatures

lower than 300ºC. In our system, weight loss of polymeric matrix is responsible for electrical resistivity of the conductive composite sensors. Thermal oxidation of epoxy resin tunes up the filler loading around percolation, and causes a significant change in electrical resistivity due to the strong sensitivity of conductive polymer composites around percolation concentration [154].

Table 5.2 Parameters from Boltzmann fitting of electrical resistance vs ageing time curves

Temp.	Sample No.	$log(\rho_1)$	$log(\rho_2)$	$log(t_c)$	Δt
210°C	A-1	10.796	5.074	3.571	0.463
	B-1	9.935	5.225	3.717	0.384
	C-1	7.517	4.386	3.953	0.478
	Average $log(t_c)$	-	-	3.747	-
220°C	A-2	11.161	4.884	3.388	0.557
	B-2	9.817	4.756	3.373	0.470
	C-2	7.597	4.230	3.700	0.602
	Average $log(t_c)$	-	-	3.487	-
240°C	A-3	11.004	4.934	2.926	0.573
	B-3	9.782	4.845	3.050	0.460
	C-3	7.677	4.660	3.116	0.627
	Average $log(t_c)$	-	-	3.031	-
260°C	A-4	11.102	5.288	2.363	0.544
	B-4	9.787	5.366	2.359	0.425
	C-4	7.643	5.226	2.319	0.611
	Average $log(t_c)$	-	-	2.347	-

What is notable in monitoring the ageing situation of polymer based components also includes the relatively long lives (up to years) of the component at relatively low ageing temperature. This significantly extends the time needed in developing *in-situ* sensors applied at low temperature. So that, usually, researchers have to predict the ageing condition at low temperature based on the data obtained at high ageing temperature, which is also noted as an "accelerated life testing"[155, 156, 157]. Here, we plot $log(t_c)$ as a function of $1/T$, and a good linear relationship between them is found, as shown Figure 5.18, confirming Equation 5.7 very well, providing possibility of predicting electrical resistivity changing at temperature.

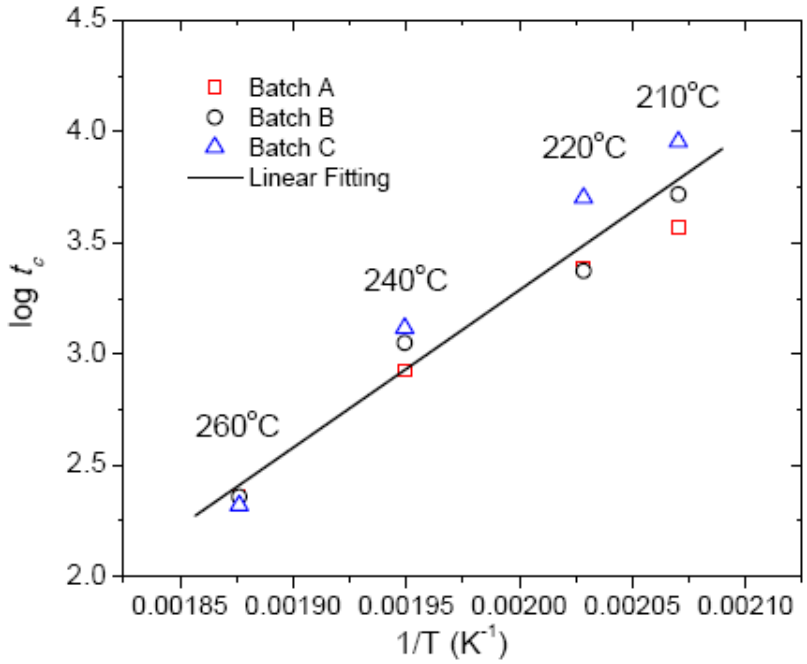

Figure 5.18 Average values of $log(t_c)$ vs 1/T

5.2.8 Conclusion

Bis-phenol A type epoxy resin, as a polymer matrix in the carbon black filled epoxy composites, shows significant changes in its chemical structure during thermal-oxidation ageing. FTIR measurements indicated that the hydroxyl group and C-H bonds degraded at the early stage of the ageing process. The generation of unsaturated carbon atoms (bonded with sp^2 carbon-carbon double bonds) in the main chain of epoxy resin

increased the rigidity of epoxy molecular structure, resulting in the higher thermal stability enhancement and storage modulus of the aged composite after ageing, which were confirmed by TGA measurement Moreover, experiment data of electrical resistivity as a function of ageing time at different temperatures can be fitted well by Botlzmann equation. Confirmed by both theoretical deductions and experimental data, the value of the induction time, $log(t_c)$, is a constant at fixed ageing temperature and independent on initial electrical resistivity. The linear relationship between $log(t_c)$ and ageing temperature curve provides possibility of predicting electrical resistivity changing at temperature other than the applied ageing temperatures in the study.

CHAPTER 6 EPOXY/h-BN COMPOSITES FOR THERMALLY CONDUCTIVE UNDERFILL MATERIALS IN FLIP-CHIP APPLICATION

Hexagonal Boron Nitride (h-BN) can be applied as a thermally conductive filler to increase the thermal conductivity of polymeric composites [158, 159]. This study is focusing on the relationship between the filler morphology and its effects on the thermal conductivity. In this study, two kinds of h-BN fillers with different morphologies were applied to generate an efficient thermal transfer path through the filler and epoxy resin interfaces. The microstructure, the dynamic mechnical properties and thermal conductivity for the h-BN filled underfills were characterized. The h-BN greatly increased the thermal conductivity of the underfill and their moduli were well controlled in a low level which can be greatly helpful to reduce thermal stress in flip-chip application.

6.1 Introduction

The current nano scale feature sized device (~45-65 nanometer) are continuously scaling down the interconnect dimensions, which has led to the introduction of copper can low-k dielectric for low RC (resistance times capacitance) delay [160, 161], noise reduction and power dissipation requirement. However, the porous nature of low k materials used in current low k application results in the Cu/low k devices being very vulnerable to mechanical and thermomechanical stress. Moreover, the porous structure of low k material has low thermal conductivity, which brings great challenge to thermal dissipation.

Underfill materials have been used to improve the flip-chip type device reliability since it was proven to be effectively distributing thermal stress generated in the package evenly to all solder joints/balls, resulting in dramatically enhancing solder joint fatigue

life [162, 163, 164]. In addition to using low modulus and low CTE underfills for reducing the thermal stress, researches have also showed the thermally conductive underfills can significantly enhance the reliability of the flip-chip because of its thermal dissipative capability as well as the mechanical protection of the flip-chip device structure [165166]. Therefore, a novel underfill material is expected to take its role in improving the Cu/low k device reliability as well. However, up to now, there is rarely underfill material available which can absorb such high thermal stress and dissipate heat to protect the next generation Cu/low k or ultra low k devices. Consequently, a novel high performance underfill/polymer composite material is required for highly reliable next generation fine pitch Cu/low k devices.

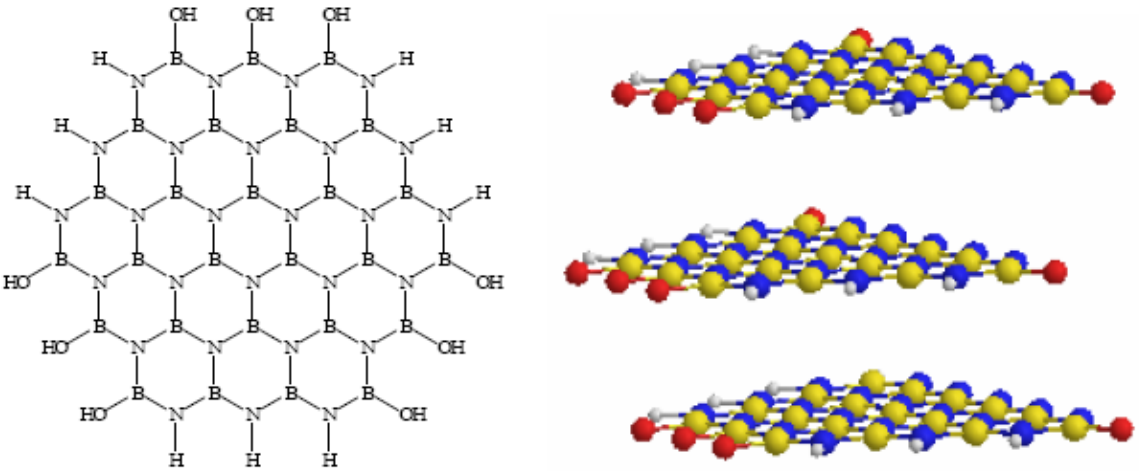

Figure 6.1 Left: 2-D structure of single sheet of h-BN, Right: 3-D structure of 3-layer h-BN.

Moreover, it is believed that morphology has significant effects on the percolation of heat conduction path as has been expected by modeling work such as Kerner-Nielsen modeling. The effects of particle morphology on thermal conductivity and mechanical properties of the underfill materials will also be studied by microstructure characterization and thermal conductivity measurement.

Due to the high thermal conductivity and isolating nature, boron nitride nano-flakes are chose as high conductive fillers in the research. I proposes the study of thin

sheets of *h*-BN in HBLED applications for their promising application in high transparent, low cost, isolating, and high thermal conductive encapsulant. The inherent conductivity of a single BN crystal is 300 to 400 W/m-K. A polymer composite with BN crystals typically yields 10 W/m-K, while conductivities up to 25 W/m-K can be achieved via special compounding techniques and optimal selection of the crystal and polymer [167,168,169]. Moreover, h-BN may be the best choice for low modulus high thermal conductive insolating material, which can also have other good performance as shown in Table 1.2.

In addition, efforts are proposed to be paid on improving the thermal conductivity of the hybrid composites, while maintain the transparency of the epoxy-silicone resin. As can be seen from, transparency is a function of the particles size, the smaller the particles are, the higher transparency/smaller absorption can be obtained in the visible light region (400-700nm).

6.2 Experimental

6.2.1 Materials

Diglycidyl ether of bisphenol A (DGEBA, EPON-828) was obtained from Miller-Stephenson Chemical (Danbury, CT). 4-Methylhexahydrophthalic anhydride (MHHPA) was supplied by Lindau Chemicals (Columbia, SC). Silicon carbide (2 Micro Powder) was purchased from Alfa Aesar® A Johnson Matthey Company (Ward Hill, MA). Hexagonal boron nitrides (PT-120 and PX-60) were obtained from Momentive Proformance Materials.

6.2.2 SEM measurement

Surface morphology of the aged samples was studied by SEM measure. A LEO 1530 SEM was applied in the measurement, and h-BN samples were dispersed in ethanol,

drop on conductive tapes, dried in a vacuum and coated with a thin layer of gold before testing.

6.2.3 DMA measurement

The DMA used is the Model 2980 by TA Instruments. The single cantilever fixture was chosen and the ramping rate was set to 10 °C /min. The multi-frequency mode was used to obtain storage modulus (G'), loss modulus (G"), tan delta, and transition temperatures (DMA Tg) at one frequency of 1 Hz.

6.2.4 TMA measurement

The coefficient of thermal expansion (CTE) of the cured sample was measured on a Thermo-Mechanical Analyzer (TMA, TA Instruments, Model 2940). The dimensions of the sample were about 5×5×2 mm. The sample was heated in the TMA furnace at 5ºC/min from room temperature to 200ºC. The CTE below the T_g is defined as α_1 and the one above as α_2.

6.2.5 Thermal conductivity measurement

Thermal conductivity tests were operated on a Light Flash Apparatus LFA 447 NanoFlash™ (NETZSCH Instruments, Inc.). In the measurement, xenon flash lamps fire a pulse at the sample's lower surface, while the infrared detector measures the temperature rise of the sample's top surface. The sophisticated software then determines the sample's thermal diffusivity. The software uses these values and the bulk density (ρ) to calculate thermal conductivity from the equation: $k = \alpha \rho C_p$. In the test, samples were cut into 10 × 10 mm^2 and then coated by Au and graphite spraying. The test temperature was set to 25°C and 6 data points were tested.

6.3 Result and discussion

6.3.1 Morphology of h-Boron Nitride

Morphology of thermal conductive fillers plays important roles in the thermal conductivity of polymer composites. As has been expected in Kerner-Nielsen model, which can be shown in below equations [170, 171, 172, 173]

$$\frac{k}{k_1} = \frac{1 + AB\phi_Z}{1 - B\psi\phi_Z}$$

$$A = k_E - 1,\ B = \frac{k_2/k_1 - 1}{k_2/k_1 + A} \qquad \textbf{Equation 6.1}$$

$$\psi \approx 1 + \left[(1-\phi_m)/\phi_m^{\,2}\right]\phi_Z$$

Where k is the thermal conductivity of the composite, k_1 and k_2 are the thermal conductivities of the polymer and filler, respectively, A is a constant related to the generalized Einstein coefficient K_E, B is a constant related to the relative conductivity of the components, ψ is a function related to the maximum packing fraction ϕ_m of the filler (ϕ_m is normally estimated to be 0.637), ϕ_z is the volume fraction of the filler. In Kerner-Nielsen model, the value of parameter A are related to generalized Einstein coefficient K_E. The shape of the filler will greatly affect the value of K_E and make great different in thermal conductivity of polymer composite.

With difference in morphology, two h-boron nitride samples PX-60 and PT-120 were applied and compared. Former research showed morphology of fillers in polymer resins plays an important role in the thermal conductivity of polymer composites. For example, in Kerner-Nielsen model, filler shape, agglomeration among fillers, and adhesion between filler and polymer matrix, will affect the value of K_E (generalized Einstein coefficient) and make great difference in thermal conductivity of polymer composite [174, 175, 176, 177]. In order to compare the morphologies between h-boron nitride samples, SEM tests were applied and the surface imagines are shown in Figure 6.2. As we can see, significantly differences existed in the shape and agglomeration

situation of h-BN fillers. In PX-60, boron nitride fillers are conglomerated and some spherical structure (with radius of 50-100μm) existed. By contrast, in PT-120, there are only irregular shaped boron nitride flakes without significant conglomeration.

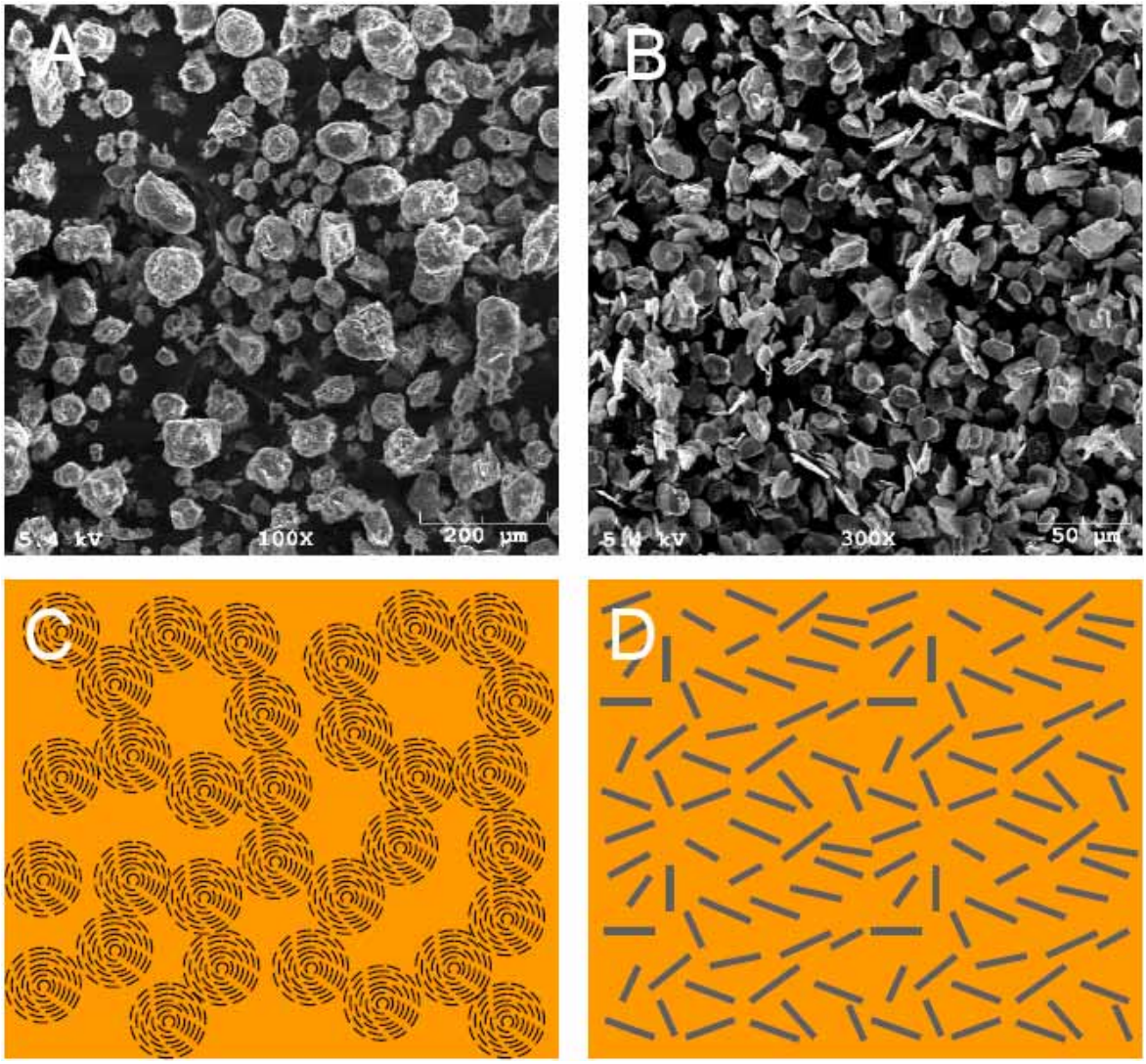

Figure 6.2 (A) SEM imagines of h-BN filler, PX-60, (B) SEM imagines of h-BN filler, PT-120. (C) A schematic illustration of h-BN filler in composite, PX-60, (D) SEM A schematic illustration of h-BN filler in composite, PT-120.

6.3.2 Thermal conductivity of h-BN/Epoxy composite

Thermal conductivities of the Epoxy/BN composite were measured by a Light Flash Apparatus LFA 447 NanoFlash™ (NETZSCH Instruments, Inc.). The obtained

values of polymer composite thermal conductivity are shown by 2 curves in Figure 6.3. As can be seen from the figure, thermal conductivity values were greatly increased by introducing h-boron nitride. Both of the two kinds of h-BN fillers showed high efficiency in increasing thermal conductivity of the epoxy composites. The highest thermal conductivity value obtained in the study is 3.35W/m.K, comparing with those of pure Epoxy 828 (~0.132 W/m.K, measured in same conduction).

Moreover, thermal conducting increased significantly in the filler loading region from 40-60wt%, indicating percolation-like phenomenon in the thermal transfer pass. Also, Epoxy 828/BN PX-60 composite showed rather larger (~2X) thermal conductivity values than there counterparts from Epoxy 828 and BN PT-120, indicating the stronger ability of BN PX-60 in increasing thermal conductivity of epoxy composites.

The possible reason for the difference between the two kinds of BN fillers in increasing thermal conductivity of composite can be described as follow. It has been widely accepted that the phonon scattering across the interface can affect the thermal conductivity of polymer composite greatly. Generally speaking, void (air)-polymer interface and polymer-particle interfaces, which are common in polymer composites can greatly reduce the thermal conductivity. In BN PX-60, BN particles conglomerates significantly, there is less interface between polymer and boron nitride fillers, hence the less phonon scattering and low thermal resistance. By thus, the difference in filler morphology can affect thermal conductivity of epoxy composite significantly.

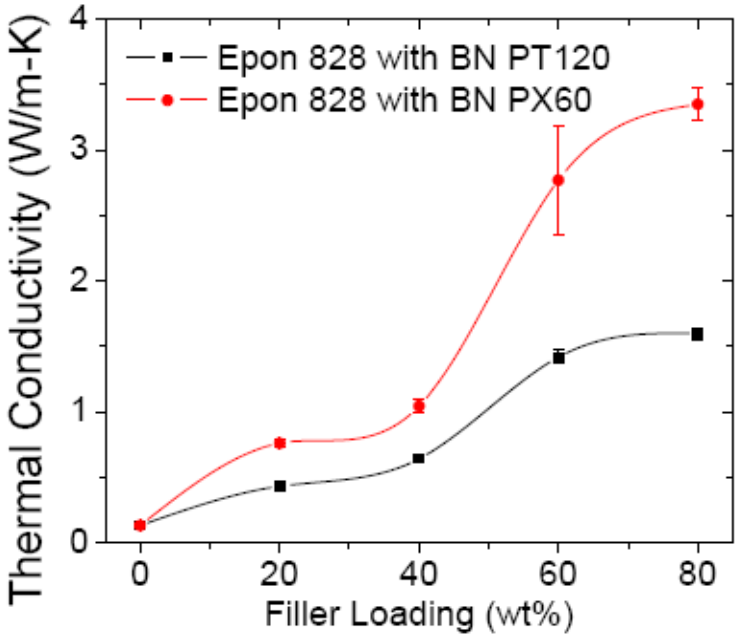

Figure 6.3 Thermal conductivity of the polymer composites at 25°C with boron nitride PX-60 and PT-120.

6.3.3 Mechanical properties of h-BN/Epoxy composite

The stress between the interface of a silicon chip and a substrate is mainly caused by the mismatch of CTE and modulus between the two components. This stress attacks certain solder joints of a flip-chip bumps structure resulting in the solder joint failures. By using the polymeric underfill in-between, the stress can be mitigated. The underfill material can distribute the generated stress other solder joints as well as absorb the stress by itself.

Such thermal stress found in the electronic packages is a major source of device failure, which can be expressed as

$$\sigma = \int_{T_1}^{T_2} E \cdot \Delta\alpha dT \qquad \textbf{Equation 6.2}$$

Where σ is the thermal mechanical stress, E , α, T are storage modulus ,coefficient of thermal expansion (CTE) of the material, and temperature, respectively. As shown in the equation, the CTE mismatch between the materials and its high elastic modulus may cause the thermal mechanical stress, which is generated during

the manufacturing process or operating (on/off) and accumulated in the device which ultimately causes device failures. In addition to the physical properties, heat in the package can significantly degrade the device reliability.

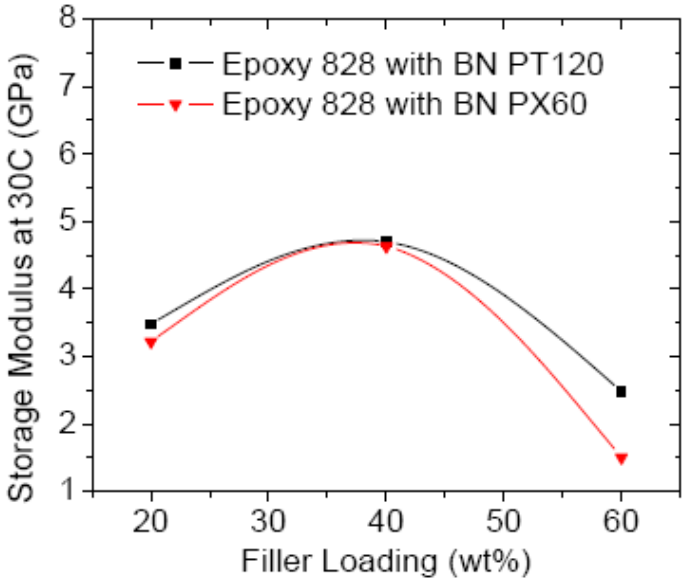

Figure 6.4 Storage moduli of Epoxy/BN composites.

DMA and TMA measurements were applied to measure the moduli, Tg and CTE of the sample. As shown by Figure 6.4, the moduli of Epoxy 828 and BN samples with 20wt%, 40 wt%, and 60wt% BN at room temperature range from 1.6 to 4.7GPa, comparing to that of epoxy 828 without any filler (1.92 GPa, in same test condition). It can be observed from the storage modulus trend of the epoxy/BN composites, storage modulus of the composites sample showed peaks around 40wt% filler loading and decreased at high filler loading region. The phenomena may due to the hexagonal polymorphs nature of h-BN, which is composed of layers of hexagonal sheet, analogous to graphite. In the hexagonal polymorphs, boron atoms lay over and above nitrogen atom, Force between these neighbor hexagonal boron nitride sheets is proven to be weaker than covalent bond, which can facilitate the relative movement between the hexagonal sheets. By thus, energy generated by thermal stress can be efficiently absorbed and moduli of the composites can be we controlled in a low level, hence helping to reduce thermal stress.

Also, TMA measurement showed that CTE values of Epoxy/BN composite samples were significantly reduced, as can be seen from Table 6.1. Moreover, T_g values of Epoxy/BN composites were also listed in Table 6.1. It can be seen that the T_g values (133.2 to 165.5°C) of the composites are not significant reduced after introducing BN fillers, helping to improve the thermal resistance of the epoxy composite.

Table 6.1 Mechanical properties of polymer composites.

Sample name	T_g(°C)	CTE(ppm/K)
Epoxy 828	141.8	76.1
Epoxy 828 with 20wt% PX-60	151.1	60.3
Epoxy 828 with 40wt% PX-60	165.5	55.7
Epoxy 828 with 60wt% PX-60	165.0	39.6
Epoxy 828 with 20wt% PT-120	133.2	61.7
Epoxy 828 with 40wt% PT-120	131.1	56.5
Epoxy 828 with 60wt% PT-120	159.9	40.2

6.4 Conclusion

By comparing the thermal and mechanical properties of composite from Epoxy 828 and two kind of BN fillers, it was found that if BN particles conglomeration significantly reduce interface between polymer and boron nitride fillers, hence the less phonon scattering and high thermal conductivity. Also, by introducing BN filler, modulus values of the composites can be well controlled in low level, contributing to the thermal stress control.

CHAPTER 7 THERMAL CONDUCTIVITY ENHANCEMENT OF EPOXY COMPOSITES BY INTERFACIAL COVALENT BONDING FOR UNDERFILL AND THERMAL INTERFACIAL MATERIALS (TIMS) IN CU/LOW K APPLICATION

Electronics and photonics devices have been pushed towards faster in speed and lower in profile. Therefore, semiconductor industry has made immense advances in operation frequency increase and IC scale reduction [85, 86]. The growing-up operation frequency and integration density also dramatically increases thermal power within devices. *e.g.,* Power dissipation for new-generation microprocessors is already over 100W. With the increasing thermal issues due to increasing operating frequency and lowering profile, performance and reliability of device will be decreased exponentially [178]. Thereby, thermally conductive electronic packaging materials, *e.g.* underfill materials and thermal interfacial materials (TIMs) shown in Figure 7.1, are strongly desired in order to improve heat dispersion and reduce operation temperature of devices [179].

Moreover, in order to increase gates' on/off speed in transistors, RC delay of gate has to be reduced [180]. Copper low-k dielectric materials have been applied to take place of traditional aluminum/dielectrical layer (ADL) in order to the meet demanding requirements in RC delay reduction [181]. Despite of speed advantages, many material properties involved issues of Cu/low k dielectrics can prevent high product yields and degrade device reliability. Usually, low k dielectric layers (LDL) are composed by porous materials because voids help to reduce dielectric constant values. However, such porous structures debate material thermal conductivity, increase thermal resistance of low k dielectric layers, which contributes to significant barriers of heat dissipation and an increase of thermal stress related failures [182].

Polymeric composites, *e.g.* underfill materials, have been used to improve the device reliability since it was proven to be effectively distributing thermal stress generated in the package evenly to all component in devices, compared with concentrating on the point with farthest distance to neutral point (DNP), resulting in significant enhanced joint fatigue life [183, 184, 185]. Therefore, polymer materials with enhanced thermal conductivity are expected to play an important role to improve reliability of Cu/low k devices [186]. Polymer composites applied in electrical packaging applications usually contains at lease two parts, inorganic fillers and polymeric matrix. Inorganic partials, *e.g.* fused silica, were traditionally applied to reduce coefficient of thermal expansion (CTE), however, has quiet low thermal conductivity (~1.38W/mK) [187]. In order to improve thermal dissipation in polymer composites, new generation fillers such as silicon carbide (SiC), carbon nano tubes, *etc.*, are substantial interested in current researches to take place of silica. [124, 123, 188] However, obtaining high thermal conductive polymer composites is still challenging. In most polymeric composites, phone scattering across the interface between inorganic fillers and polymer matrix are high. As the size of the inorganic fillers scales down in order to meet the requirement of fine pitch technology, specific interface area between inorganic partials and polymer matrix is dramatically increased [189]. Interfacial thermal resistance between fillers and polymer matrix has become a major barrier in obtaining polymer composite with high thermal conductivity and must be efficiently reduced.

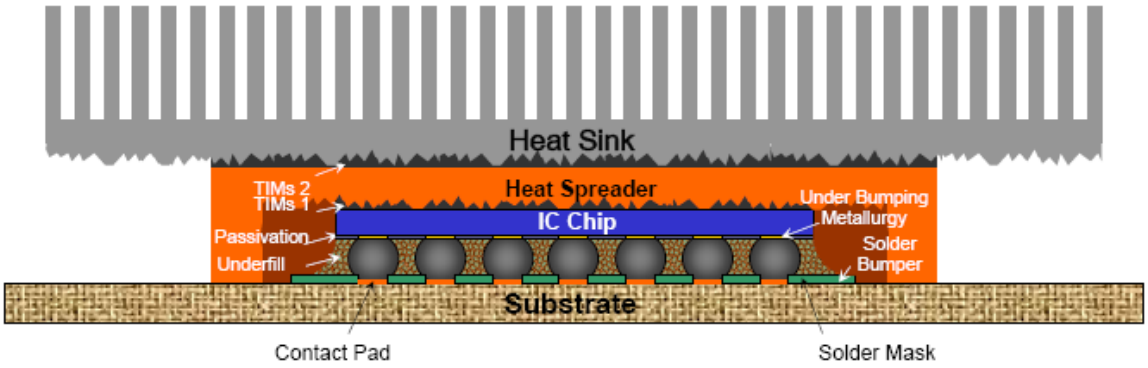

Figure 7.1 A schematic illustration of a typical flip-chip package.

Surface treatment of inorganic particles, *e.g.* nanosilica, can significantly improve particle dispersion, reduce viscosity of resin precursor, and enhance adhesion of cured polymer composites to solid substrates [190]. Moreover, particle surface functionalization can help to build solid bonding between particles and polymer matrix, which may contribute to reduction interfacial phonon scattering and thermal resistances. Here, surface of high thermal conductive fillers such as SiC particles and multiwall carbon nanotubes are successfully functionalized, which makes their surface reactive with bisphenol A diglycidyl ether and able to form chemical bonding between fillers and epoxy resin. By this means, thermal conductivity of polymer composites is found to be significantly enhanced compared with control samples, indicating the interfacial chemical bonding across interface between thermal conductive fillers and polymer matrix can promote heat dissipation in polymeric composites. The finding can benefit a development of high thermal conductive polymer composites by interfacial chemical bonding enhancement to meet the demanding requirements in current fine pitch and Cu/low k technology.

7.1 Experimental

7.1.1 Materials

Silicon carbide was purchased from Alfa Aesar. MWNTs were ordered from Sun Nanotech Co. Ltd. γ-glycidoxypropyl-trimethoxysilane (GPTMS) was obtained from OSi Specialties Inc. Diglycidyl ether of bisphenol A (DGEBA, EPON-828) was obtained from Miller-Stephenson Chemical. 4-Methylhexahydrophthalic anhydride (MHHPA) was supplied by Lindau Chemicals. (2-methylimidazolyl-(1-ethyl-4,6-diamino-s-traizine) was produced by Shikoku Company and applied as a latent accelerator in epoxy resin curing. Primaset LECY Cyanate ester (1,1-Bis(4-cyanatophenyl)ethane, CAS-No. 47073-92-7) was obtained from LONZA Group Ltd. $Cu(AcAc)_2$, ethanol, formic acid, concentrated

nitric acid and concentrated sulfuric acid applied in the study were supplied by VWR International LLC.

7.1.2 Surface oxidation and functionalization of SiC particles

In a typical procedure, SiC particles are placed in a Muffle furnace and maintained in air atmosphere at 800°C for 3 hours in order to coat a nano layer of SiO_2 on SiC surface at high temperature. γ-glycidoxypropyl-trimethoxysilane (GPTMS) are applied to functionalize the SiO_2 coated SiC particle. 1g deionated water, 20ml ethanol and 1g SiO_2 coated SiC particle are mixed and sonicated for 30minutes. Then 0.2g GPTMS and formic acid is dropped into the mixture consequently until the PH value of the mixture reaches 4. Reaction temperature is raised to ~80°C and maintained to allow the mixture reflux. Samples with reaction time of 2, 6, 13, 15, 21, 25 hours are collected, washed with ethanol, and dried at 120ºC for 6 hours.

7.1.3 Surface functionalization of MWNTs

In a typical experiment, MWNTs (2 g) is mixed with 15ml concentrated nitric acid (~69%), and 45ml sulfuric acid (~98%), magnetically stirred, heated to 130°C and kept at the temperature for 16 hours in order to complete the reaction. The reaction is stopped when there is no brown-colored NO_2 generated. The product is separated by centrifuging, washed by DI water, and then dried in vacuum oven.

7.1.4 Transmission electron microscopy (TEM) characterization

To prepare samples for Transmission Electron Microscopy (TEM) characterization, a drop of colloid solution form ethanol and surface treated fillers (SiO_2 coated SiC particle and acid treated MWNTs) is placed on a copper grid coated with carbon membrane. The solvent is evaporated at room temperature, leaving the fillers on

the grid. These samples are examined and photographed with a transmission electron microscopy (JEOL 100C, 100kV).

7.1.5 Fourier transform infrared (FTIR) characterization

A Fourier-Transform Infrared (FTIR) spectrometer (Nicolet, Magna IR 560) is used to study the surface functional groups on functionalized SiO_2 coated SiC and functionalized MWNTs. The fillers are scanned with a reflectance mode through wave numbers ranging from 500 to 4000 cm^{-1}.

7.1.6 Thermogravimetric analysis (TGA)

A Thermogravimetric Analyzer (TGA, TA Instruments, Model 2050) is applied in TGA measurement. In a typical test, a cured polymer composite sample (~5mg) is placed into a Platinum pan and tested with a ramp rate of 10°C /min from ambient temperature to 800°C in nitrogen or air.

7.1.7 Thermo-mechanical properties

A dynamic mechanical analyzer (DMA, TA Instruments, Model 2980) is applied to obtain storage & loss modulus, tan delta, and transition temperature at a frequency of 1Hz. A single cantilever mode and a ramping temperature of 10°C/min are used in the tests. The coefficients of thermal expansion (CTE) of polymer composite samples are measured on a Thermo Mechanical Analyzer (TMA, TA Instrument, Model 2940) with a temperature ramping rate at 5°C/min from room temperature to 200°C.

7.1.8 Thermal conductivity measurement

Thermal conductivity estimation of polymer composite is performed on a Light Flash Apparatus LFA 447 NanoFlash (NETZSCH Instruments, Inc.). In the measurement, polymer composite specimens were cut into 10mm*10 mm square with 1-2mm thickness and coated by gold and graphite spraying. Environment temperature is set

at 25±0.5°C. A xenon flash lamp fires a pulse at the sample's lower surface, while the infrared detector measures the temperature rise of the sample's top surface. Data points were collected and processed by sophisticated software in order to estimate thermal diffusivity (α) of the sample. The thermal conductivity from the equation: $k=\alpha\rho C_p$, where k, α, ρ, C_p are the thermal conductivity, thermal diffusivity, material density, and heat capacity, respectively.

7.2 Results and discussion

7.2.1 Surface functionalization of silicon carbide (SiC) particles

SiC is highly thermal conductive (with a thermal conductivity of ~120W/m·K), but is more difficult to be involved in a surface treatment reaction than traditionally applied silica particles, due to their relatively high chemical inertness and low concentration of silanols on their surface. Moreover, SiC is electrically semi-conductive; therefore their application as fillers in electrically insolating materials, *e.g.* underfill materials, is significantly limited. Therefore, a novel design of SiC surface treatment should be addressed in order to prepare efficiently surface-functionalized and less electrically conductive SiC particles. Here, SiC particles are treated by a two-step process. In the first step, SiC particles are thermally treated in order to generate an ultra-thin layer of silicon oxide (SiO_2), which is electrically insolating but chemically reactive with silicane coupling agent. In the second step, the SiO_2 coated SiC particles are surface-functionalized by a γ-glycidoxypropyl-trimethoxysilane (GPTMS), which can efficiently graft epoxide groups on to the particle surfaces.

As shown by Figure 7.2, a thermal surface pretreatment of SiC particles was applied to coat a nano layer of silicon oxide (SiO_2) on the SiC particle surface by oxidization treatment in air at 800°C. In the process, SiC particle surface is oxidized by O_2 and produces an ultra-thin layer of silicon oxide. The chemical reaction can be shown by a chemical reaction function as follows. [191]

$$SiC + 2O_2 \xrightarrow{\text{high temperature}} SiO_2 + CO_2$$

Transmission Electron Microscopy (TEM) is applied to detect the morphology of the coated nano layer silica on the particle. A core-shell structure in TEM image of thermal treated SiC particles in Figure 7.3 indicated that SiC particles is successfully coated by a layer of SiO_2 with a thickness ranging from 10 nm to 20 nm.

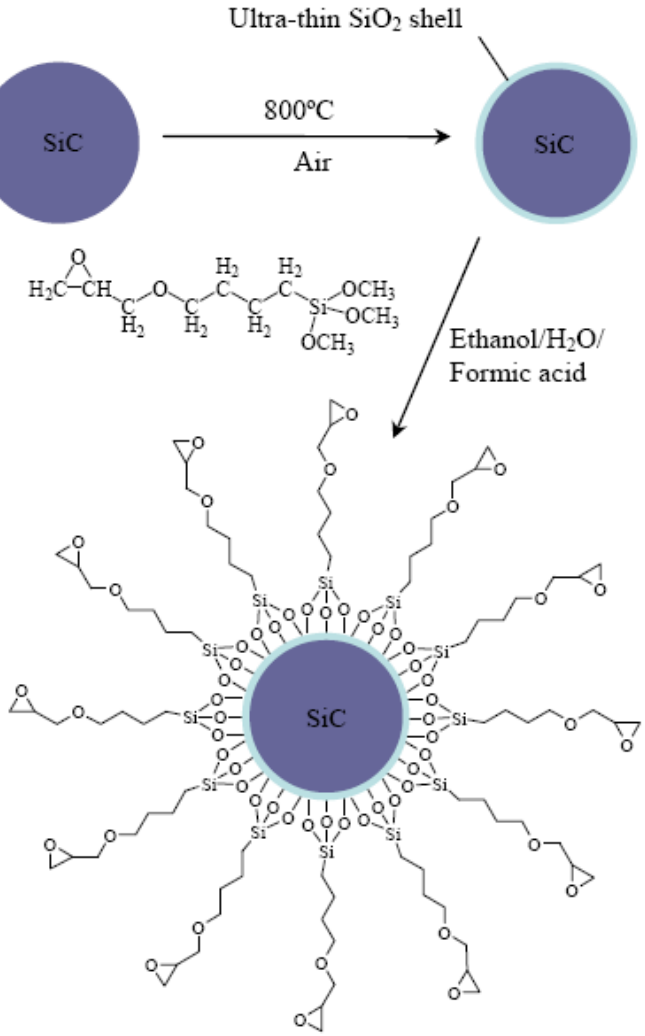

Figure 7.2 A schematic illustration of SiC surface functionalization: A thermal oxidation of SiC particle with SiO_2 layer followed by a chemical pretreatment of SiC by γ-glycidoxypropyl-trimethoxysilane (GPTMS).

Moreover, in order to build covalent chemical bonding between SiC particles and epoxy resin, SiC particle is expected to be surface functionalized with epoxide groups,

which is reactive with common applied epoxy resin with components of epoxy and hardener (4-Methylhexahydrophthalic anhydride). Silane coupling agent with epoxide groups, e.g. γ-glycidoxypropyl-trimethoxysilane (GPTMS) is a preferable chemical in the application due to their ability in react with silanol on the silicon oxide shell of the SiC particles. As shown in Figure 7.2, in a chemical pretreatment of SiO_2 coated SiC particles, GPTMS can be hydrolyzed in chemical environment (ethonal/H_2O_2/formic acid) with low PH value of ~4 and consequently react with silanols on the surface of the SiO_2 coated SiC paricles, resulting in grafting of epoxide groups on the particle surface.

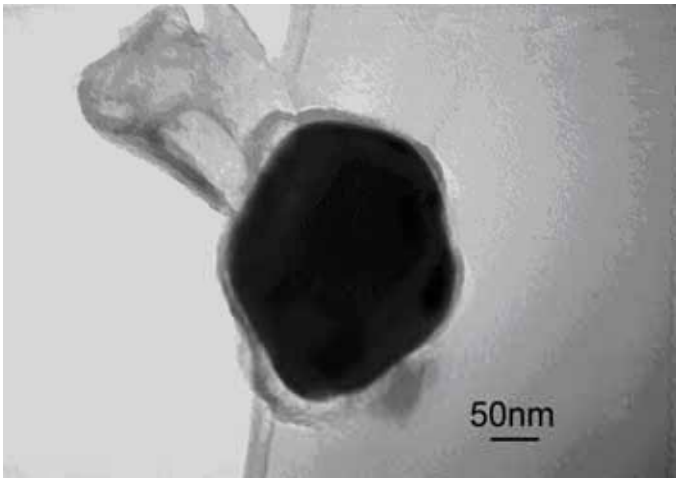

Figure 7.3 A TEM image of a SiC particle with a silicon oxide shell.

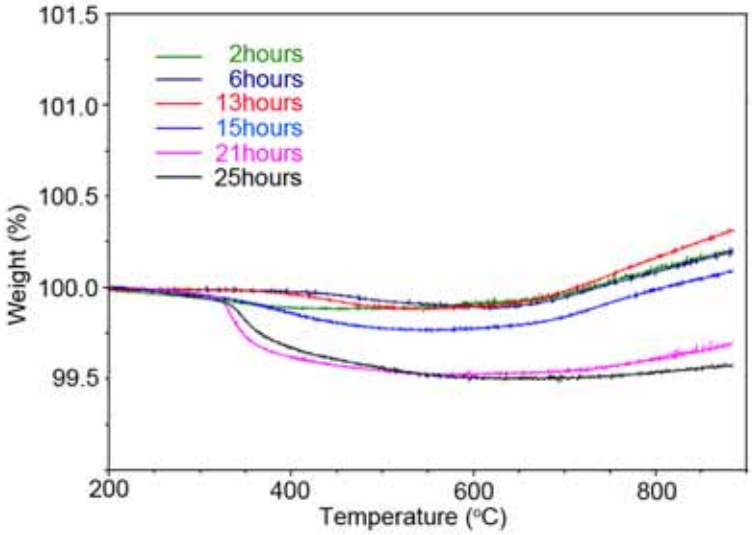

Figure 7.4 TGA measurements of GPTMS treated SiO_2 coated SiC.

TGA measurements are conducted on SiO_2 coated SiC specimens treated by GPTMS for 0, 2, 6, 13, 15, 21 and 25 hours, respectively, in order to detect organic γ-glycidoxypropyl groups grafted on the particle surface. Obvious differences in the weigh loss behaviors between GPTMS treated SiO_2 coated SiC particles and those untreated ones are shown in Figure 7.4. Untreated SiO_2 coated SiC particles shows no obvious weight loss but a slight weight gain at ~ 800°C due to further oxidation of SiC in air. In contrast, after a treatment by GPTMS for 25 hours, silane treated SiO_2 coated SiC particles shows a weight loss (~0.4%) at ~330°C in air with no obvious weight gain at ~ 800°C, respectively, corresponding to grafting of organic components (γ-glycidoxypropyl) on SiO_2 coated SiC particles.

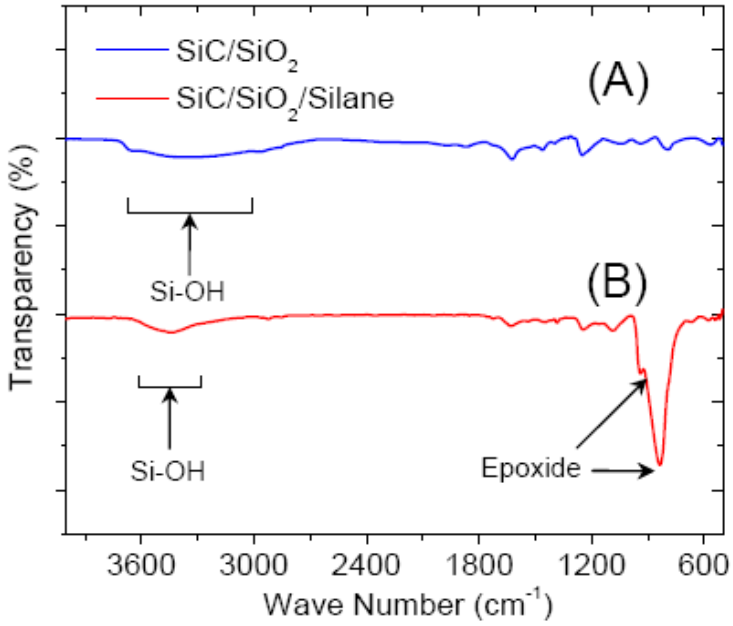

Figure 7.5 A comparison between FTIR spectra of SiO_2 coated SiC: (A) before Silane (GPTMS) treatment; (B) after Silane (GPTMS) treatment.

Moreover, FTIR spectrum of functionalized SiO_2 coated SiC confirms that γ-glycidoxypropyl is successfully grafted on particle surface. As it can be seen from Figure 7.5, in the spectra of the untreated particles, a board peaks at 3000-3700 cm^{-1} indicated that concentration of silanols on the particle surface is relatively high. In contrast, GPTMS treated particles shows a much smaller peak at ~3450 cm^{-1}, which is

corresponding to a significantly lowered silanol concentration after the reaction. Also, prominent peaks at ~ 827 and 918 cm^{-1} (epoxide) are corresponded to grafted γ-glycidoxypropyls on particle surface.

7.2.2 Chemical functionalization of MWNTs

MWNTs are also applied as thermally conductive fillers in polymer composite in order to study the influence of covalent bonding between fillers and polymer matrix on thermal conductivity of polymer composites [192]. MWNTs were treated in nitric acid in order to functionalize their surface with carbonyls and hydroxyls. TEM images in Figure 7.6 indicated that MWNTs is well debundled after acid treatment. TGA measurements, as can be seen in Figure 7.7, indicate that MWNTs are efficiently functionalized by showing a significant weight loss at ~ 250°C. FTIR spectrum in Figure 7.8 show peaks at ~3400 cm^{-1} (bonded –OH) and ~1700 cm^{-1}(C=O), indicating that COOH groups generated on MWNTs after acid treatment.

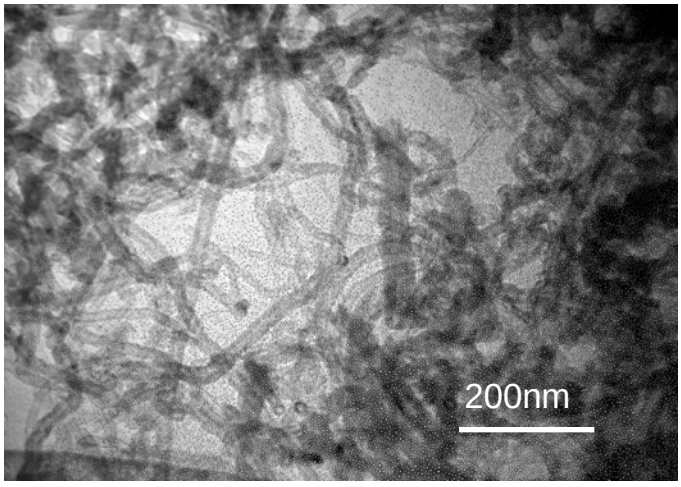

Figure 7.6 TEM image of functionalized MWNTs.

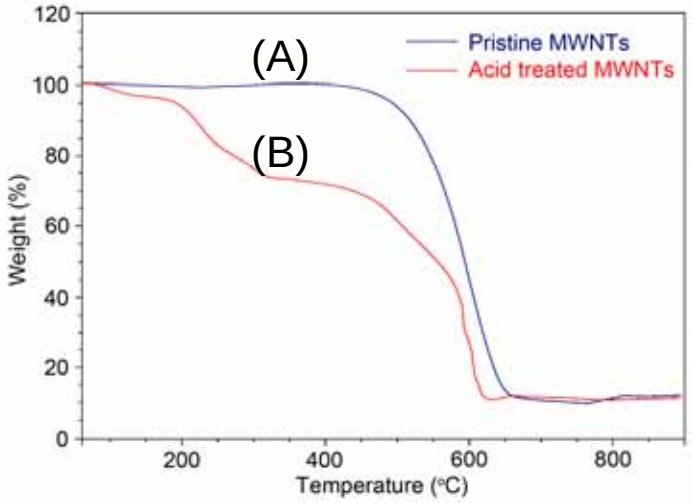

Figure 7.7 A comparison between TGA measurements of pristine (A) and functionalized MWNTs (B).

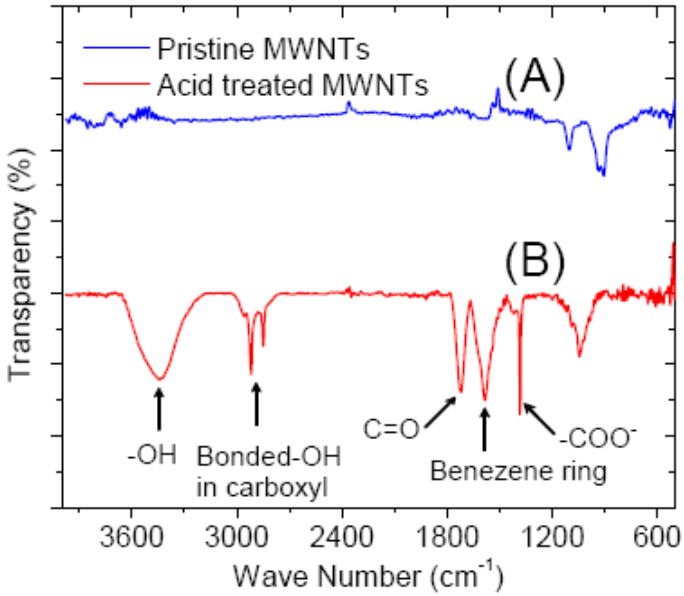

Figure 7.8 A comparison between FTIR spectra of pristine (A) and functionalized MWNTs (B).

7.2.3 Mechanical properties of polymer composites

In the study, a bisphenol A epoxy resin composed with a mixture of diglycidyl ether of bisphenol A (DGEBA) and 4-Methylhexahydrophthalic anhydride (MHHPA) are applied as polymer matrix in polymer composites. SiO_2 coated SiC particles with grafted epoxide

groups and acid treated MWNTs are applied thermal conductive fillers, respectively. Mechanical properties of thus-prepared epoxy composites are shown in Figure 7.9.

Thermal Mechanical Properties

As shown by Figure 7.9A and B, storage modulus of epoxy composite is almost linearly increased as filler loading of functionalized SiO_2 coated SiC particles and MWNTs. Temperature of glass transaction (T_g) of epoxy composite with functionalized SiO_2 coated SiC particles shows a slight reduction as filler loading increases, which was also observed on epoxy/silica composites [15]. However, in contrast, an increase in filler loading (up to 5wt %) of functionalized MWNTs causes a significant increasing of T_g of epoxy composite corresponding to the rigid long structure of MWNTs, which has also been likewise reported by Wei *et al.* [193]

Coefficient of Thermal Expension

It has been known that silica can be applied in polymer matrix in order to reduce CTE of polymer composites. Here, functionalized SiO_2 coated SiC particles also show their ability in reducing CTE of epoxy composite. As shown by Figure 7.9C, CTE of epoxy resin can be reduced from 76ppm/K for pure bisphenol A epoxy resin to ~50ppm/K of bisphenol A epoxy composite with a filler loading of 40wt%. CTE values of polymer composites can be expressed by an equation as follows. [84]

$$\alpha_{comp} = \phi\alpha_{filler} + (1-\phi)\alpha_{polymer} \qquad \textbf{Equation 7.1}$$

$$\phi = \frac{x}{x + (1-x)\dfrac{\rho_{filler}}{\rho_{polymer}}} \qquad \textbf{Equation 7.2}$$

where ϕ, α_{comp}, α_{filler}, $\alpha_{polymer}$, x, ρ_{filler} and $\rho_{polymer}$ represent volume fraction of fillers in polymer composite, CTE of polymer composite, CTE of fillers, CTE of polymer matrix, weight fraction (filler loading) of fillers, density of fillers and density of polymers, respectively.

CTE of SiC is relatively low (~4ppm/K), compared with that of fused silica (~0.5ppm/K) and pure bisphenol A epoxy resin (~76 ppm/K). Thereby, a further CTE

reduction can be expected if the filler loading of functionalized SiO_2 coated SiC is further increased. However, no obvious CTE changes are observed for MWNTs/epoxy composite here due to a relatively low filler loading of MWNTs (≤ 5wt%).

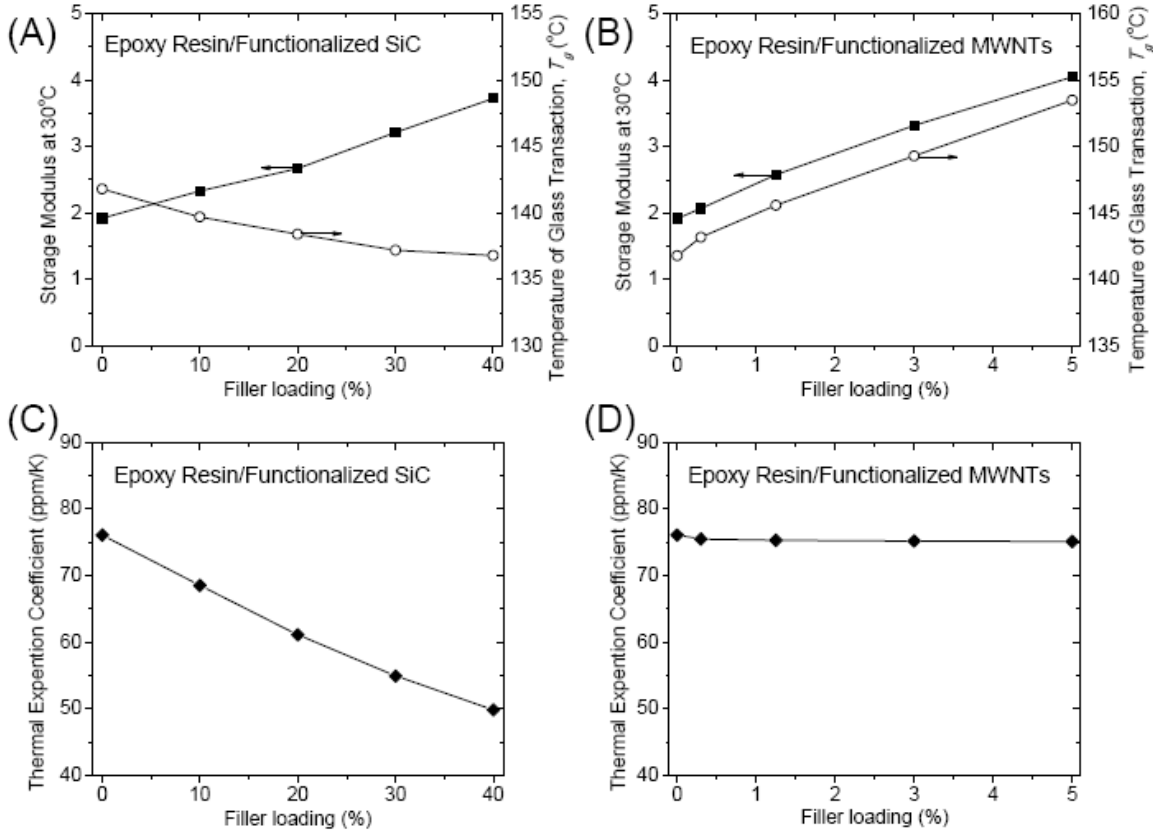

Figure 7.9 Thermal mechanical properties of polymer composites.

7.2.4 Thermal conductivity of polymer composites

Thermal diffusivity of polymer composite in the study is measured by Light Flash Apparatus (LFA 447 NanoFlash by NETZSCH Instruments, Inc.). Heat capacity (C_p) and density (ρ) were measured separately. The values of the material thermal conductivity (k) were calculated from the equation:

$$k=\alpha\rho C_p$$

where k, α, ρ, C_p are thermal conductivity, thermal diffusivity, material density, and heat capacity, respectively. In order to compare thermal conductivity of polymer composite

samples, relative thermal conductivity (k_R) is applied here with thermal conductivity of pure epoxy resin as a reference.

$$k_R = \frac{k_c}{k_{pe}} \times 100\%$$

Where k_R, k_c, k_{pe} represent relative thermal conductivity of polymer composite in percent, thermal conductivity of polymer composite, and thermal conductivity of cured pure epoxy resin.

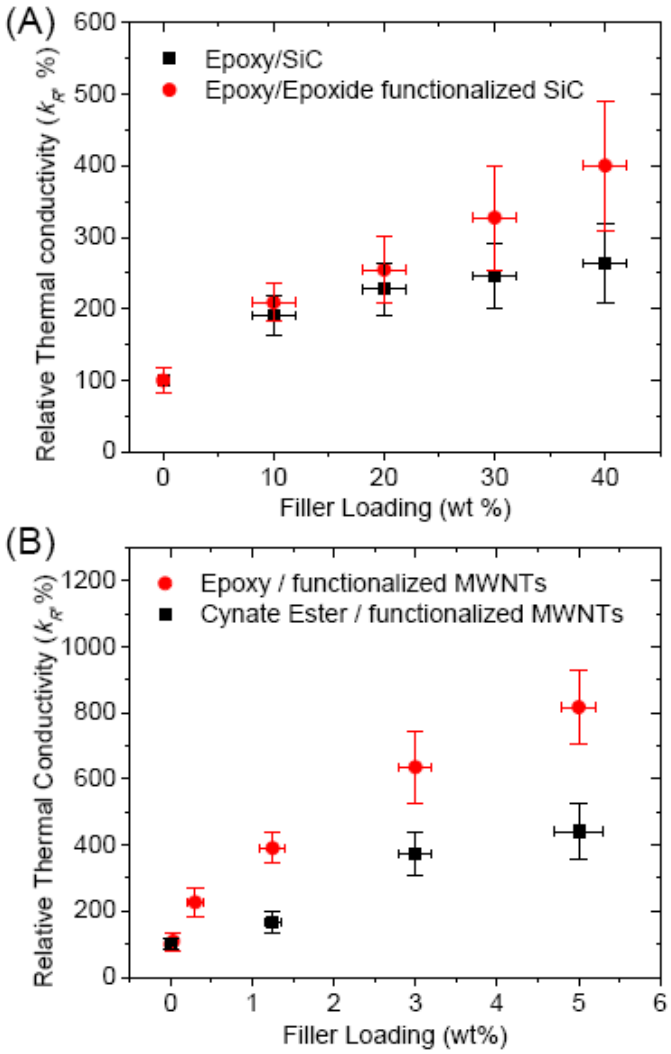

Figure 7.10 A comparison of thermal conductivity of the polymer composites at 25°C. Relative thermal conductivity is calculated with thermal conductivity of pure epoxy resin as a reference.

Thus obtained thermal conductivity values of polymer composite specimens are shown by Figure 7.10. It can be seen that the thermal conductivity values were significantly increased, compared with that of pure epoxy resin. Moreover, epoxy composites with functionalized SiO_2 coated SiC fillers are much more thermally conductive than those with untreated SiC. Although this difference is not prominent for low filler loading such as 10wt% and 20wt%, however, the significantly larger relative thermal conductivity of epoxy composite with 30wt% and 40wt% of functionalized SiO_2 coated SiC (k_R = ~ 327% and 400%, respectively) showed significant higher enhancement compared with that of samples with 30wt% and 40wt% of untreated SiC (k_R = ~ 245% and 264%, respectively). Meanwhile, as shown by Figure 7.10B, epoxy resin with functionalized MWNTs showed rather higher thermal conductivity (*e.g.*, k_R = ~ 636% and 818% at 3wt% and 5wt% filler loading, respectively) than that of cyanate ester with functionalized MWNTs (k_R = ~ 375% and 412% at 3wt% and 5wt% filler loading, respectively).

The phenomena can be understood as follows. The phonon scattering across the interface between particle filler and polymer matrix can affect the thermal conductivity of polymer composite greatly. Generally speaking, void (air)-polymer interfaces and polymer-particle interfaces, which are common in polymer composites, can greatly reduce the thermal conductivity. Compared with the void-polymer interface, particle-polymer interfaces are more important for heat transfer in polymer composites because they can not be decreased by physical method, such as vacuum and sonication. Shown in Figure 7.11A, 4-Methylhexahydrophthalic anhydride (MHHPA), a components acting as a harden in the epoxy resin, can reactive with epoxides not only from diglycidyl ether of bisphenol A (DGEBA) but also from γ-glycidoxypropyl grafted on SiO_2 coated SiC, resulting in solid covalent bonds between epoxy resin. Surface treatment in the study helped to increase the interaction between filler and polymer matrix, which can

significantly reduce the phonon scattering, can increase thermal conductivity, especially when conductive filler percolation threshold is reached.

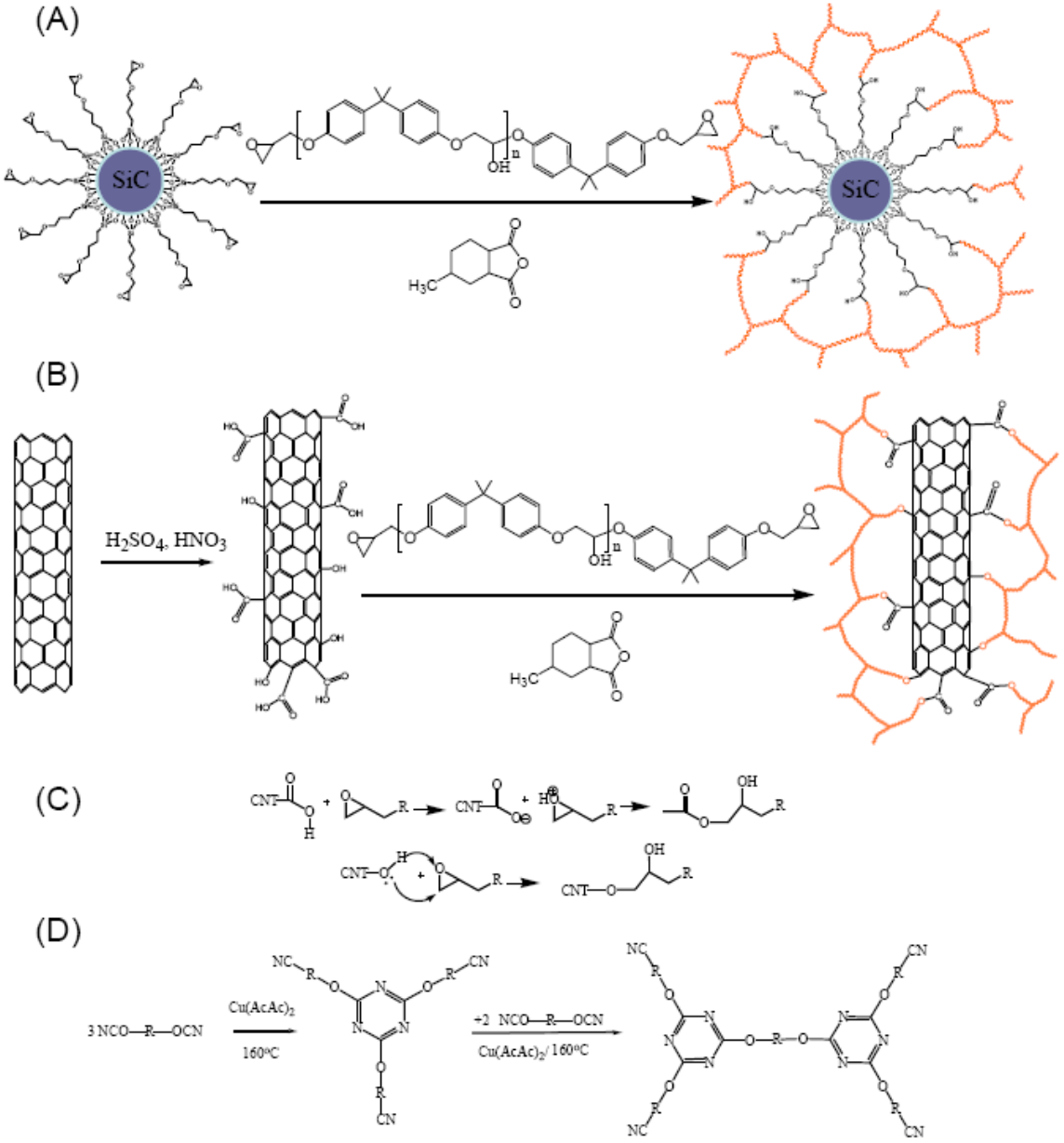

Figure 7.11 Schematic illustrations of interfacial covalent bonds between polymer matrix and thermally conductive fillers. (A). Mechanism in generating interfacial covalent bonding between SiC particle and Bisphenol A Epoxy resin. (B). Mechanism in generating interfacial covalent bonding between MWNTs and Bisphenol A Epoxy resin. (C). Chemical reactions between functionalized MWNTs and epoxide. (D). Chemical reactions curing process of cyanate ester.

Moreover, in order to find out the effect of functionalization of MWNTs to the thermal conductivity, cyanate ester was applied as polymer matrix in the composite and compared with epoxy resin. Here, epoxy resin with functionalized MWNTs showed much higher thermal conductivity than cyanate ester with functionalized MWNTs. The results suggested that surface treatment of MWNTs, in which carboxyl acid group generated as schematically illustrated in Figure 7.11B and C, greatly increased the thermal conductivity of epoxy composites. As known, cyanate ester is a group of chemical substances generally based on a bisphenol or novolac derivative, in which the hydrogen atom of the phenolic OH group is substituted by a cyanide group (-OCN), as shown Figure 7.11D. In the curing process, a trimerization of three CN groups happens and a triazine ring is formed. [194] In the process, carboxyl acid groups on treated MWNTs do not join the reaction with cyanate ester, hence the loose connection between MWNTs and cyanate ester resin and high thermal interfacial resistance. However, in contrast with cyanate ester, epoxide group is a cyclic ether ring with only three atoms. In curing process, epoxide group can be nucleophilically attacked by amine or carboxyl acid, and the crosslinking structure of epoxy resin are formed. Carboxyl acid on the treated MWNTs can join the reaction with epoxy resin by the nuclephilic addition reaction and form relatively tough chemical bonding between CNT and epoxy resin. Thus, the thermal conductivity of epoxy/MWNTs resin can be greatly increased.

7.3 Conclusion

SiC particles are successfully coated with a ultrathin SiO_2 layer by thermal oxidation method. In the following surface-functionalization by γ-glycidoxypropyl-trimethoxysilane (GPTMS), epoxide groups are grafted on the SiO_2 coated SiC particles. Mechanical measurements of epoxy composites with thus prepared functionalized SiC particles indicated the relatively low modulus, reduced coefficient of thermal expansion, and significantly enhanced thermal conductivity, which will help to reduce the global thermal stress of the underfilled flip-chip structure. Moreover, experimental results

indicate that functionalization of MWNTs can reduce interfacial thermal resistance between filler and epoxy resin by forming chemical bonding across the interface. Compared with that of control samples, significant thermal conductivity enhancement of epoxy composites with these functionalized fillers indicated that interfacial chemical bonding across interface between fillers and polymer matrix can promote significantly enhanced heat dissipation of polymeric composites, which is promising in Cu/low K applications.

CHAPTER 8 SUMMARY AND FUTURE WORK

8.1 Summary

As a new nanomaterial with high electrical mobility (exceeding 15, 000 $cm^2\ V^{-1}\ s^{-1}$), high thermal conductivity (5×10^3 W $m^{-1}K^{-1}$) and excellent mechanical properties as well as large specific surface area (~2600 cm^2/g) [1], graphene has been applied in next-generation nano-electronics [3], gas sensors [9], transparent electrical conductors [5], thermally conductive materials [8], and superior energy capacitors [4] *etc.* Convenient and productive preparation of graphene is thereby especially important and strongly desired for its manifold applications.

Ever since its discovery, graphene has been successfully prepared with various methodologies such as mechanical stretching [2], epitaxal and CVD growth [37, 38], chemical developments, *etc*. Among these, preparation of chemically developed functionalized graphene from graphene oxide (GO) has significantly high productivity and low cost, thereby has been extensively interested. However, usually prepared by an extreme oxidation of graphite flakes [49], graphene oxide is highly functionalized with decorating polar groups such as carboxyls, hydroxyls, diols, *etc*, on irregular-sized graphene-like domains [13, 14], which deliver an excellent water solubility of GO [19, 20]. These polar groups on GO inevitably introduce structural defects on fine pattern of pristine graphene, destroy conjugation among sp^2 hybridized carbon atoms as well as interconnection between of graphene-like domains, and thereby significantly reduce electrical conductance of GO. Removal of polar groups by chemical or thermal reduction can help resurgence of an interconnected graphene structure [48]. After reduction, high electrical conductance and transparency can be obtained, therefore reduced GO (rGO) is

noted as a potential candidate for large area transparent conductors [5, 6, 7]. Here, microwaves (MW) are proposed to be applied in order to reduce the amount of graphene oxide (GO) at a relatively low temperature (~165^{o}C). Preliminary results indicate that resurgence of interconnected graphene-like domains contributes to a low sheet resistance of ~7.9×10^{4} Ω/square with an optical transparency of 92.7% at ~550 nm after MW reduction, indicating the very high efficiency of MW in the reduction of GO's reduction.

Moreover, graphene is a promising candidate for thermal interfacial materials (TIMs) due to its extraordinarily high thermal conductivity (~ 5300W m^{-1} K^{-1} for suspended monolayer grapheneand ~600W m^{-1} K^{-1} for supported monolayer graphene). However, graphene is usually recumbent on solid substrates, while vertically aligned graphene architecture on solid substrate is rarely available and less studied. For TIMs, electrodes of ultracapacitors, *etc*, efficient heat dissipation and electrical conductance in normal direction of solid surfaces is strongly desired. In addition, large-volume heat dissipation requires a joint contribution of a large number of graphene sheets. Graphene sheets must be aligned in a large scale array in order to meet the requirements for TIM application. Valuable efforts have been paid on preparation of paper-like aligned graphene oxide (GO) and thermally reduced GO. However, in-plane thermal conductivity of GO and reduced GO (1.9 W m^{-1} K^{-1} and 0.14-2.87 W m^{-1} K^{-1}, respectively) is low and unlikely able to meet demanding requirements in thermal management of current photonic and electronic devices.

Here, thermally conductive fuctionalized multilayer graphene sheets (fMGs) are efficiently aligned in a large scale by vacuum filtration method at room temperature, as evidenced by SEM images and polarized Raman spectroscopy. A remarkably strong

anisotropy in properties of aligned fMGs is observed. High electrical (~386 S cm^{-1}) and thermal conductivity (~112 W m^{-1} K^{-1} at 25°C) as well as ultra-low coefficient of thermal expansion (~ -0.71 ppm K^{-1}) in in-plane direction of A-fMGs are obtained without any reduction process. VA-fMG TIMs are prepared by constructing a three-dimensional vertically aligned functionalized multilayer graphene architecture between contact Silicon/Silicon surfaces with pure Indium as a metallic medium. Compared with their counterpart from recumbent A-fMGs, VA-fMG TIMs have significantly higher equivalent thermal conductivity and lower contact thermal resistance.

Moreover, electrical and thermal conductivities of polymer composite are also greatly interested here. Previous researches indicated that filler loading, morphology of fillers, and chemical bonding across filler/polymer interfaces have significant influence on electrical/thermal conductivity of polymer composite. Therefore, the research also pay substantial attention to these issues, which is important for the application of polymer composites in polymer aging sensors, underfill materials and thermal interfacial materials etc.

First, electrical resistivity of CPCs is highly sensitive on volume or weight ratio (filler loading) of conductive fillers in polymer matrix, especially when filler loading is close to percolation threshold (p_c). Thermal oxidation aging usually can cause a significant weight loss of polymer matrix in a CPC system, resulting in a filler loading change which can be exhibited by a prompt alteration in electrical resistivity of CPCs. Here, the phenomena are applied as approach for *in-situ* monitoring thermal oxidation status of polymeric materials [144,145, 146] is developed based on an electrical sensors based on conductive polymeric composites (CPCs). It is noticed that aging status of polymer materials are difficult to detect and predict, however, very important for the reliability of polymeric insulation systems, which may work in various unforeseen environmental conditions including heat, light and oxygen in motors, aircrafts, and

electrical generators *etc*. In order to detect ongoing failures for predictive maintains, effective monitoring methods for real-time thermal oxidation aging status of polymeric components are desired and required by standards. In this study, with an original filler loading slight smaller than percolation threshold, CPCs from carbon black (filler) and bis-phenol type epoxy (polymer matrix) are prepared and aged. Carbon black is found to chemically inert and can't be decomposed in the aging condition. In contrast, several degradation mechanisms during the aging processes are accounted for a significant weight loss of bis-phenol type epoxy [147, 148, 149, 150]. Therefore, during aging, filler loading of the carbon black filled epoxy composites is continuously increasing to approach and exceed percolation threshold consequently, resulting in a dramatic change in electrical resistivity. The study developed a model for electrical resistivity of sensors from the CPCs as a function of aging time at constant aging temperature, which is in a good agreement with a Boltzmann-Sigmoidal equation. Based on the finding, the sensors show their capability of *in-situ* in-situ monitor and estimate aging status of polymeric components by a fast and convenient electrical resistance measurement.

Second, it is noticed that real industrial applications give various requirements for thermally conductive materials. Among current conductive materials(*e.g.* metals and metallic alloys), most are both electrically and thermally conductive, which could satisfy many traditional applications (*e.g.* electrical cords for power transmission). However, exceptional situation always exist, as industrial requirements keep becoming more demanding. For instance, thermally conductive electrical-insulators are strongly desired for underfill materials, which are important for packaging of photonics and electronic devices. Naturally, electrically-insulating yet thermally conductive nano-materials with acceptable cost, such as boron nitride, surface treated silicon carbide, *etc*, are also chosen and studied as thermal conductive fillers. Properties of their polymer composites are also significantly highlighted in the study for their excellent performance in industrial

applications. Here, interfacial issues related to these thermal conductive fillers are systemically studied.

On the one hand, the study focuses on relationship between morphology of h-BN particles and thermal conductivity of their epoxy composites. It is found that spherical-agglomeration of h-BN particles can significantly enhance thermal conductivity of epoxy resin, compared with dispersed h-BN plates, by substantially reducing specific interfacial area between h-BN and epoxy resin. On the other hand, surface treatment / functionalization of inorganic particles can significantly enhance adhesion of cured polymer composites to solid substrates by building solid bonding between particles and polymer matrix, which contribute to reduction of interfacial phonon scattering and thermal resistances across filler/polymer interface. Here, surface of high thermal conductive fillers such as SiC particles and MWNTs are successfully functionalized, which makes their surface reactive with bisphenol A diglycidyl ether and able to form chemical bonding between fillers and epoxy resin. By this means, thermal conductivity of polymer composites is found to be significantly enhanced compared with control samples, indicating the interfacial chemical bonding across interface between thermal conductive fillers and polymer matrix can promote heat dissipation in polymeric composites. The finding can benefit a development of high thermal conductive polymer composites by interfacial chemical bonding enhancement to meet the demanding requirements in current fine pitch and Cu/low k technology.

Based on the above facts, it is believed that specific interfacial area between filler and polymer materials is dramatically important for thermal conductivity of polymer composite. The particle shape and agglomeration of thermal conductive particle is critical in reducing thermal interfacial resistance among polymer composite due to their influence to specific interfacial area. Moreover, solid covalent bonding across fillers/polymer interface can promote heat dissipation in polymeric composites more than

physical adsorption, hence more preferred in thermal conductivity enhancement of polymer composite.

As described above, in summary, the finding in the study provides:

1. A convenient methodology for GO reduction with high efficiency, which have potentials in broadening the application of reduced GO as transparent electric conductors.
2. Lyotropic alignment of fMGs, a convenient low temeparature mass processing methodology of graphene plates.
3. A throughout approach for graphene-based TIM assembly.
4. Knowledge of aligned graphene architectures and its anisotropy, which may not only facilitate graphene's application in current demanding thermal management but also promote its widespread applications in electrodes of energy storage devices, conductive polymeric composites, etc.
5. A systematic kinetic study for a direct relationship between electrical resistivity of conductive polymer composite and aging conditions (*e.g.* aging temperature and aging time) and its application as in-situ ageing sensors of polymer ageing.
6. Electrically-insolating thermally conductive composites with enhanced thermal conductivity and its applications in electronic packaging materials.
7. A further understanding on influence of filler morphology/shape and surface functionalization on polymer composite thermal conductivity.

8.2 Future Work

8.2.1 Generating phonon coupler among A-fMGs

Phonon transports along chemical bonding is faster than that conducted by weak Van der Waals force. How to improve the thermal transfer among fMGs sheets is a key issue in obtaining high thermal conductivity. Moreover, in order to apply A-fMGs as TIMs, the interfacial thermal resistance between A-fMGs and different subtracts (such as Si, Cu, Al) have significant importance. In future work, chemical structures will be applied as phonon coupler via molecular welding to improve the thermal conductivity of the A-fMGs material and reduce the thermal resistivity between A-fMGs and substrates [195, 196, 197].

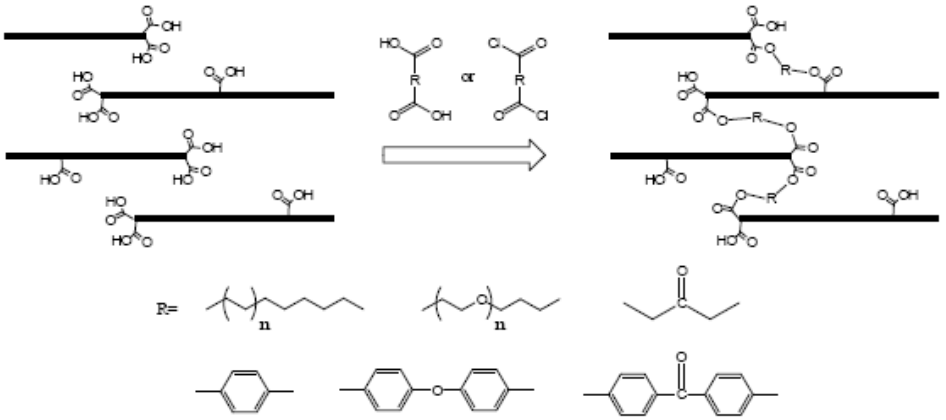

Method A

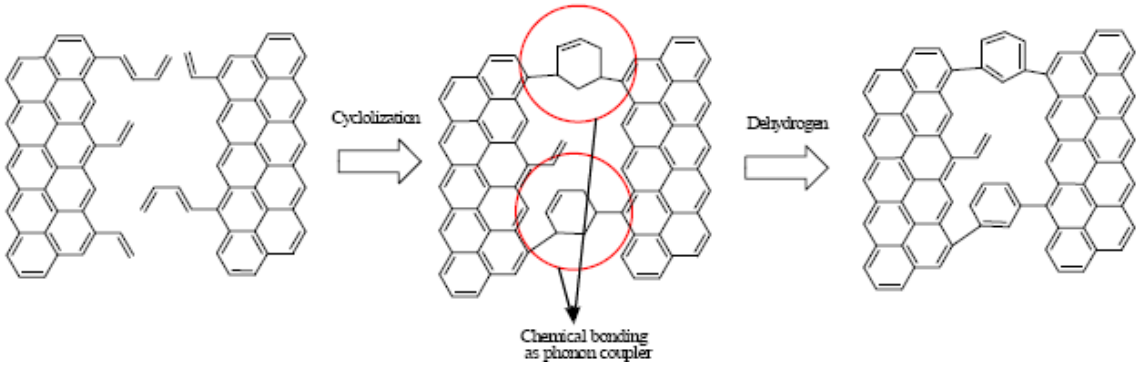

Method B

Figure 8.1 Chemical reactions applied in generating phonon coupler.

Phonon couplers between fMG will be generated by the reaction between A-fMGs and different chemicals. By this method, aromatic rings, hydrocarbon chains with different lengths, and functional groups (such as ester, ether groups) will connect the graphene sheets and form chemical bonding between sheets. Understanding of influence of the phonon coupler from different chemical structures and electrical & thermal properties of bulky aligned graphene samples will be the major task.

Two chemical reactions are proposed to be applied in generating phonon couplers between the graphene sheets via molecular welding, as shown by Figure 8.1. In method A, a group of chemicals with two functional groups can react with the carboxyl acid groups on graphene sheets by ionic substitution reaction. In method B, thermal cyclolization conducted by Diels-Alder addition reaction between the diene and vinyl groups can generate aromatic rings as phonon couplers connecting graphene sheets.

Two parameters of the phonon coupler will be studied. First, the density (volume density of a phonon coupler), can affect the thermal transfer between the graphene nanoplates. Chemicals (for example, SO_2Cl_2) of high reactivity with carboxyl groups on fMGs, will be applied and tested in their ability to generate the higher density of chemical bonds between and along with the edges of graphene sheets. Moreover, the uncontrollable distance variety among carboxyl groups may also prevent the generation of chemical bonding. In order to optimize the high phonon coupler density, chemicals with different molecular lengths, as longer chains could decrease the phonon coupling effectiveness, as such their optimized structures will also be studied. Secondly, the chemical structure of the phonon coupler may also influence thermal transfer between graphene sheets. Theoretically, graphene-like chemical structures can reduce phonon scattering between graphene sheets. In method B, the created C-C linkages and aromatic rings have very similar hybridization structures with that of graphite. These interface compounds are expected to act as a phonon coupler to transfer the phonons from one graphene to another; with reduced phonon scattering at the interface and increasing bulk

thermal transport capability. Also, understanding that functionalization of graphene sheets can also impact thermal transfer in graphene sheets, the PI proposes Raman test to monitor functionalization degrees of graphene sheets and optimize the thermal conductivity by studying the relationship between them.

8.2.2 Evaluating the influence of phonon coupler on the electronic & thermal properties of A-fMGs

Mathematically, electrical and thermal resistance of perfectly aligned graphene can be shown by Figure 8.2. The electronic and thermal resistivity of the A-fMGs in in-plane direction can be divided into two parts: the first part is the thermal resistance in fMGs sheet (in-plane direction), the other is that between fMGs.

$$R_{total} \sim \sum_{i=1}^{n/2} R_{2i+1} + \sum_{i=1}^{n/2} R_{2i} \qquad \textbf{Equation 8.1}$$

$$n \sim \frac{L}{l} \qquad \textbf{Equation 8.2}$$

where n is the total number of graphene layers along the thermal transfer pass, L is the length of bulk sample in in-plane direction, l is the average dimension of graphene sheet in lateral direction. The former part $\sum_{i=1}^{n/2} R_{2i+1}$ should be very small due to the ultra high thermal conductivity of graphene in this direction, while the latter part $\sum_{i=1}^{n/2} R_{2i}$ is the very large due to the phonon scattering between nanoplates. Although, calculations indicated that the number of the interfaces n should be proportional to $\frac{L}{l}$, which should not be dramatically large, bad contact across the interfaces can cause a dramatically large resistance and affect the in-plane thermal conductivity as well. Naturally, the anisotropy of electronic and thermal conductance of the A-fMGs sample will be significantly, if the graphene layers is ideally aligned.

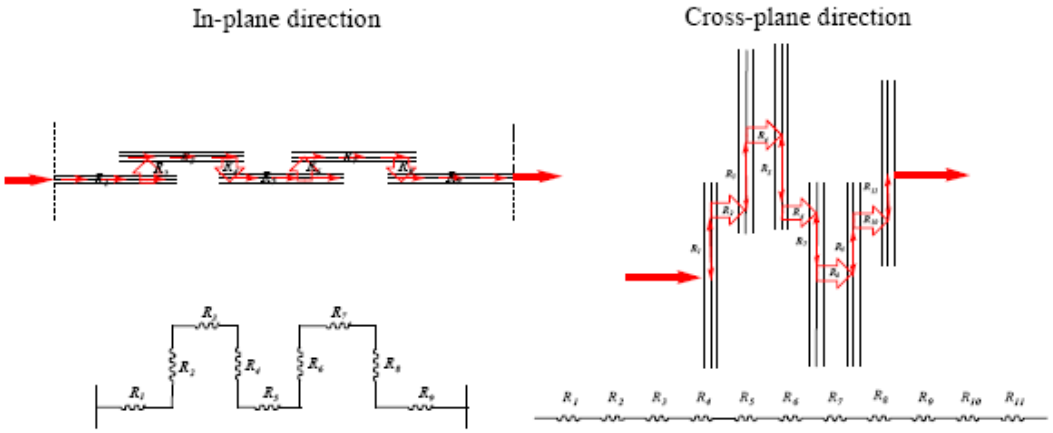

Figure 8.2 A schematic illustration of perfectly aligned graphene sheets.

However, in a real situation, some of fMGs layers in A-fMGs may not oriented in exactly same direction with others. It has been found that the angular distribution can affected thermal conductivity of A-fMGs and polymer composites**.**

8.2.3 Epoxy Composite with functionalized AlN

Due to its high thermal conductivity (~230 W/m.K), low CTE(4.1ppm/K), medium dielectric constant (8.7@1MHz), and a high density (3.26g/cm^3), aluminum nitride (AlN) particles also interested in thermal conductive composite. As shown by Figure 8.3, a modeling result based on Kerner-Nielsen model indicates that composite based on AlN particles can be highly thermally conductive. Moreover, AlN particles are usually coated with silica in commercial product, in order to prevent its reaction with water. These facilitate a reaction of silica-coated AlN (SCAN) with silane coupling agent, *e.g.* γ-glycidoxypropyl-trimethoxysilane (GPTMS). A reaction process applied in GPTMS treatment of Silica coated SiC, as shown in Chapter 7, can also be applied in SCAN surface treatment.

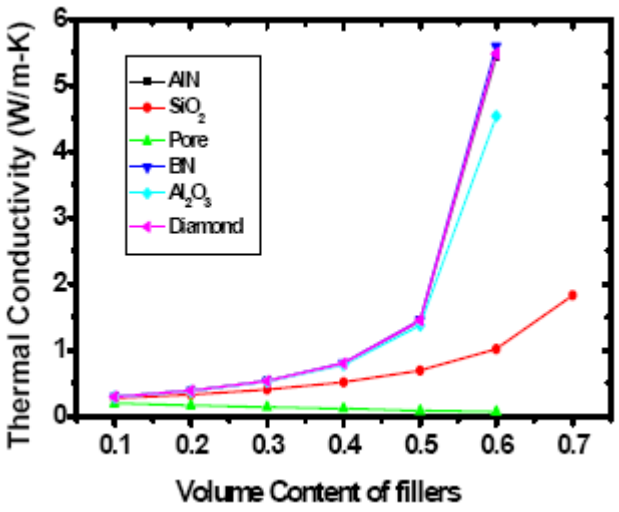

Figure 8.3 Thermal conductivities of composites using Kerner-Nielsen Model and based on irregular particle shape.

Preliminary results indicate that FTIR and TGA can be applied in characterization of SCAN surface functionalization. Figure 8.4A shows that FTIR spectra of SCAN treated with GPTMS can be successfully functionalized. In the spectrum of GPTMS functionalized SCAN, vibration bands for Si-O at 1089 cm^{-1}, CH_2 absorption band at 2944 cm^{-1} and 2878 cm^{-1} can be observed indicated that GPTMS reacted with silanol on SCAN surface and graft γ-glycidoxypropyl on to the particle surface. A intensitive -OH at ~3400cm^{-1} is also observed. A contrast between TGA spectra of untreated SCAN and surface functionalized SCAN confirms above results. In TGA spectrum of untreated SCAN, weight loss above 400^{o}C is significantly limited (smaller than 0.2%). However, functionalized SCAN shows more than 1.8% weight losses at a temperature above 400 ^{o}C. Moreover, reaction condition is also influencial. It is found that pH value in the reaction can affect the reaction rate and final functionalization of the particle significantly, as shown by the obvious difference in TGA spectra in Figure 8.4B.

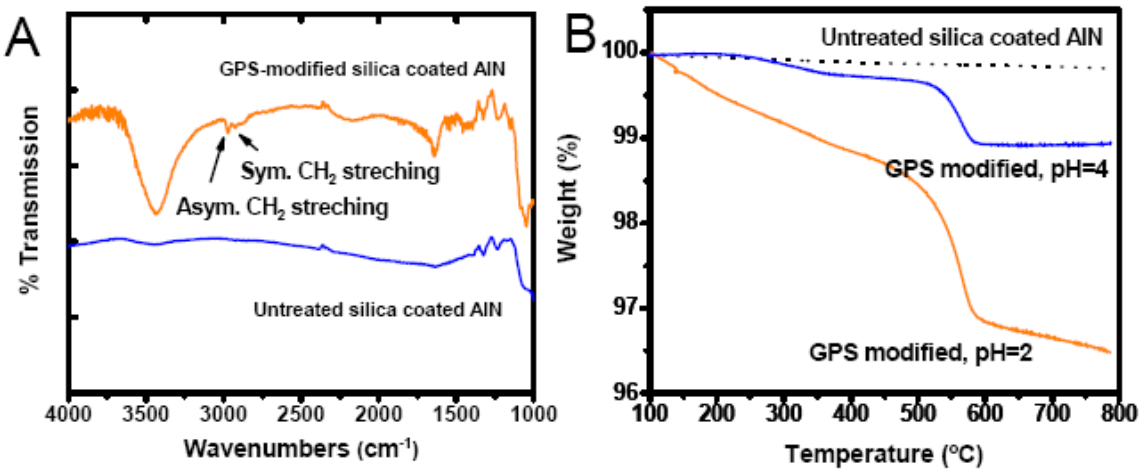

Figure 8.4 (A)FT-IR spectra of untreated SCAN and SCAN functionalized by GPTMS, respectively. (B). TGA of SCAN and SCAN functionalized by GPTMS, respectively.

As pH increases, the weigh loss of functionalized SCAN obviously decreases. It may indicate that less functional groups is grafted to SCAN surface when treated at higher pH value. This results can be confirmed by FTIR spectra.

In future work, the effect of GPTMS grafting on the SCAN particle surface and also be characterized by XRD. The methodology is expected to characterize phase change after surface functionalization. The effect of the possible surface phase change can also be explored. Different silane coupling agents with various functional group and chain length would also be an interesting issue due to the difference in reaction activity and functionalizion effects. Moreover, morphology (size and shape) of filler is also important.

8.2.4 Preparation of Ultra Thin 2-D Boron Nitride

Current fine feature sized devices (~45 nanometer) are continuously scaling down the interconnect dimensions, which has led to the introduction of copper and low-k dielectrics for low RC delay, noise reduction and power dissipation requirement. However, the porous nature of the low k dielectics has low thermal conductivity, which brings great challenge to thermal dissipation. Moreover, the porous structure also results

in the Cu/low k devices being very vulnerable to mechanical and thermomechanical stress. The objective of this project is to study novel highly thermally conductive underfill materials with optimized mechanical, physical, rheological and thermal properties (modulus, CTE, and thermal conductivity) to simultaneously minimize stresses on Cu-low k and interconnection joints.

The underfill materials have been used to improve the flip-chip device reliability since it was proved to be effectively distributing thermal stress generated in the package evenly to all solder joints/balls vs concentrating on the farthest to the distance neutral point (DNP), resulting in dramatically enhancing solder joint fatigue life [198, 199, 200]. In addition to using low modulus and CTE underfills for reducing the stress, researches also show the thermally conductive underfill can enhance the reliability because of its thermal dissipative capability as well as the mechanical protection of the flip-chip device structure [169]. Therefore, the underfill material is expected to play an important role to improve the Cu/low k device reliability as well. Some research on improving the Cu/low k device reliability by using a low modulus underfill was reported. However there is no underfill material available which can absorb such high thermal stress and dissipate heat to protect the next generation Cu/low or ultra low k devices. Consequently, a novel high performance underfill/polymer composite material is required for the highly reliable next generation fine pitch Cu/low k devices.

Thermally conducting but electrically insulating materials are needed for underfill materials used in electronic packaging. Metals are both thermally and electrically conducting, so they cannot be used for this purpose. Diamond is outstanding in its high thermal conductivity while it is electrically insulating, but it is expensive, even in powder form. Almost all polymers are electrically insulating, but they are also thermally insulating due to low crystalline degree, low crystalline regularity and high phonon scattering. Thus, polymers alone cannot be used for this purpose. On the other hand, polymers have low processing temperatures, which allow them to be easily made into

polymer matrix composites in bulk or coating forms. By using fillers which are thermally conducting but electrically insulating, a polymer-matrix composite can become thermally conducting while electrically insulating.

Carbon and ceramic materials with high thermal conductivity have been used as fillers within the polymer matrix. These candidate fillers include alumina, boron nitride, diamond, aluminum nitride, carbon nanotubes, graphite, and so on. Among these candidates, ultra thin two-dimensional structure filler showed significant merit in improving the thermal conductivity of epoxy resin, comparing with traditional 3-D fillers, SWNTs (1-D structure) and carbon blacks (amorphous structure). For example, thermal expended graphite nanoplatelets can improve the thermal conductivity of epoxy resin by up to 3000% (~6.4W/mK at 20°C with a volume filler loading of 25%), as shown in Charpter 6. The results also showed that the thinner the 2-D fillers are, the larger thermal conductivity enhancement in the epoxy-based composites. Naturally, ultra thin 2-D h-boron nitride and functionalized single graphene sheet are considered as thermal conductive filler in improving the thermal conductivity of underfill materials. This study will focus on optimizing the thermal and mechanical properties of these high performance underfill materials by applying ultra thin 2-D boron nitride fillers and functionalized graphene single sheets.

NMR SPECTRA OF EPOXY RESIN APPLIED IN CHARPTER 5

(A): ^{1}H-NMR spectrum of Bisphenol epoxy resin mixture used for polymer aging sensor

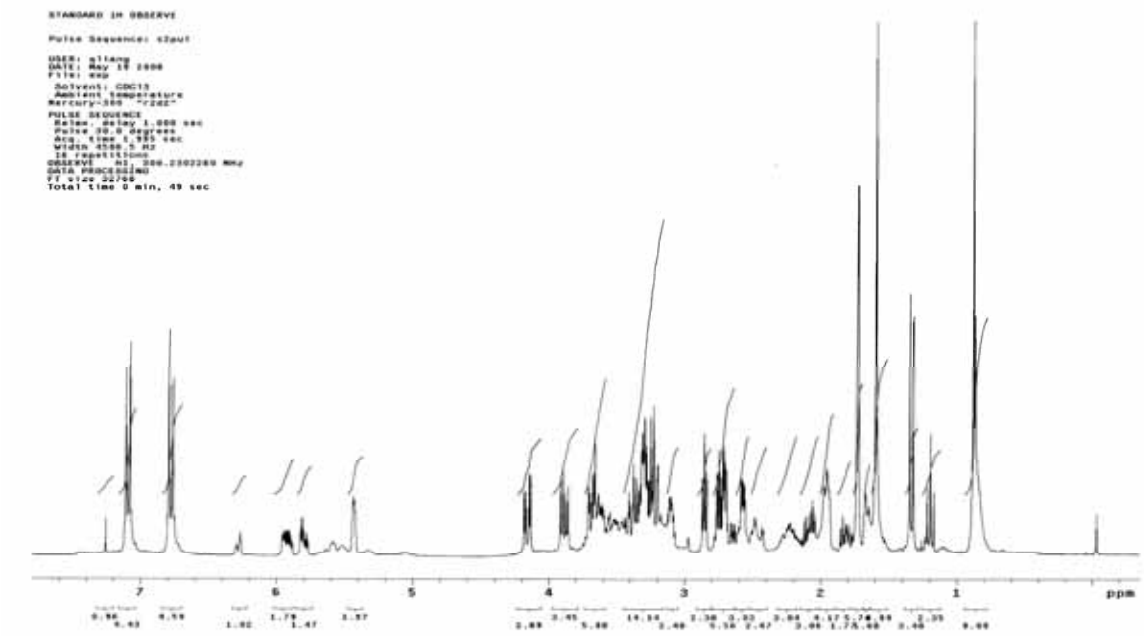

(B): ^{1}H-NMR spectrum of Bisphenol epoxy integrant used for polymer aging sensor

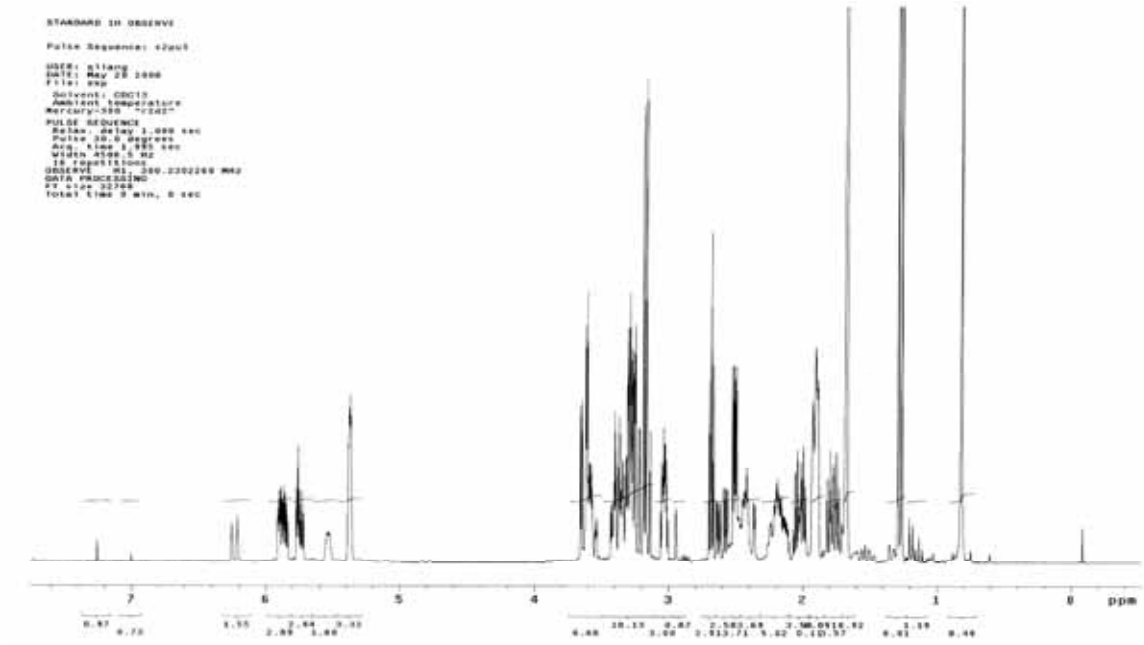

(C) **^{13}C-NMR spectrum of epoxy resin mixture used for polymer aging sensor**

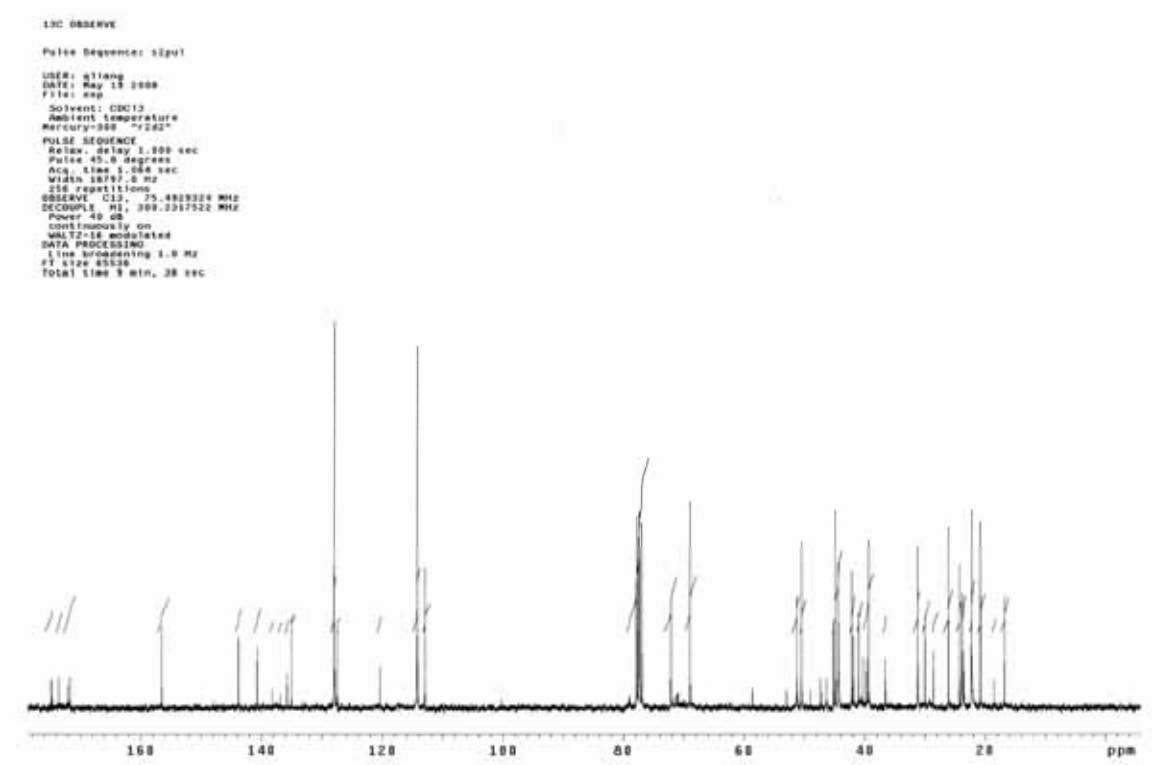

(D): ^{13}C-NMR spectrum of separated epoxy integrant used for polymer aging sensor

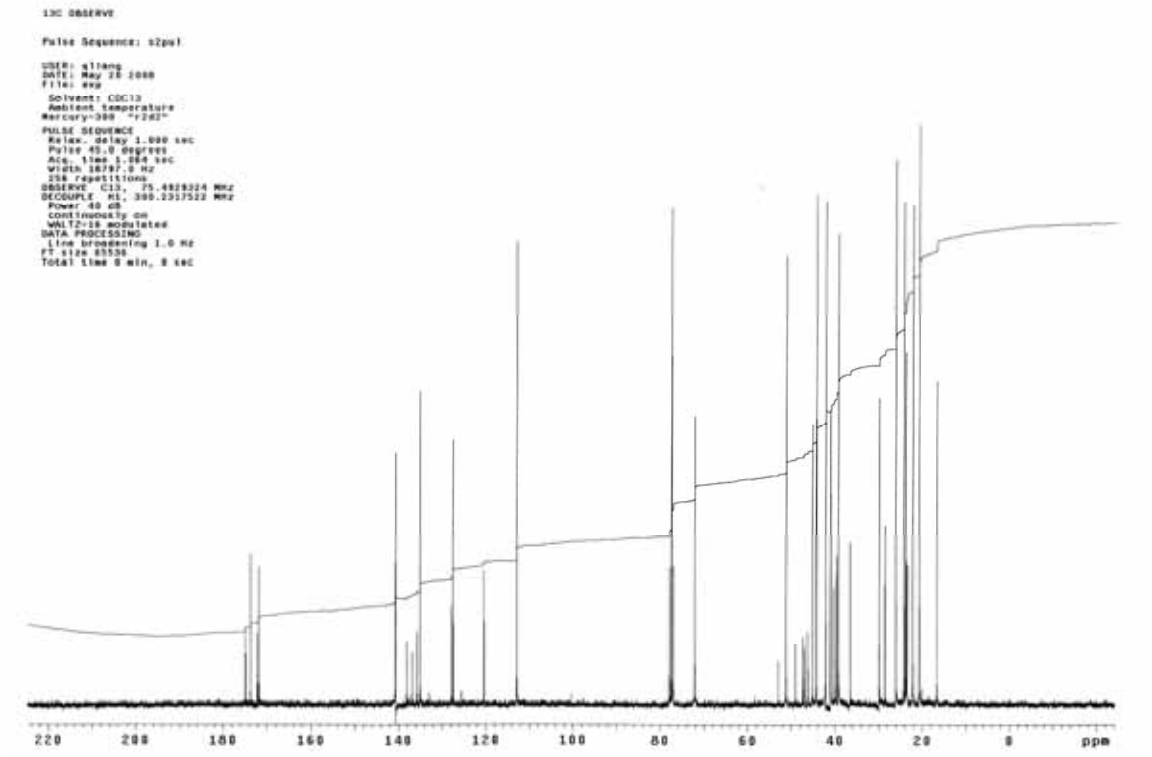

APPENDIX A

TGA-MS SPECTUM OF CURED EPOXY RESIN USED FOR POLYMER AGING SENSOR IN CHARPTER 5

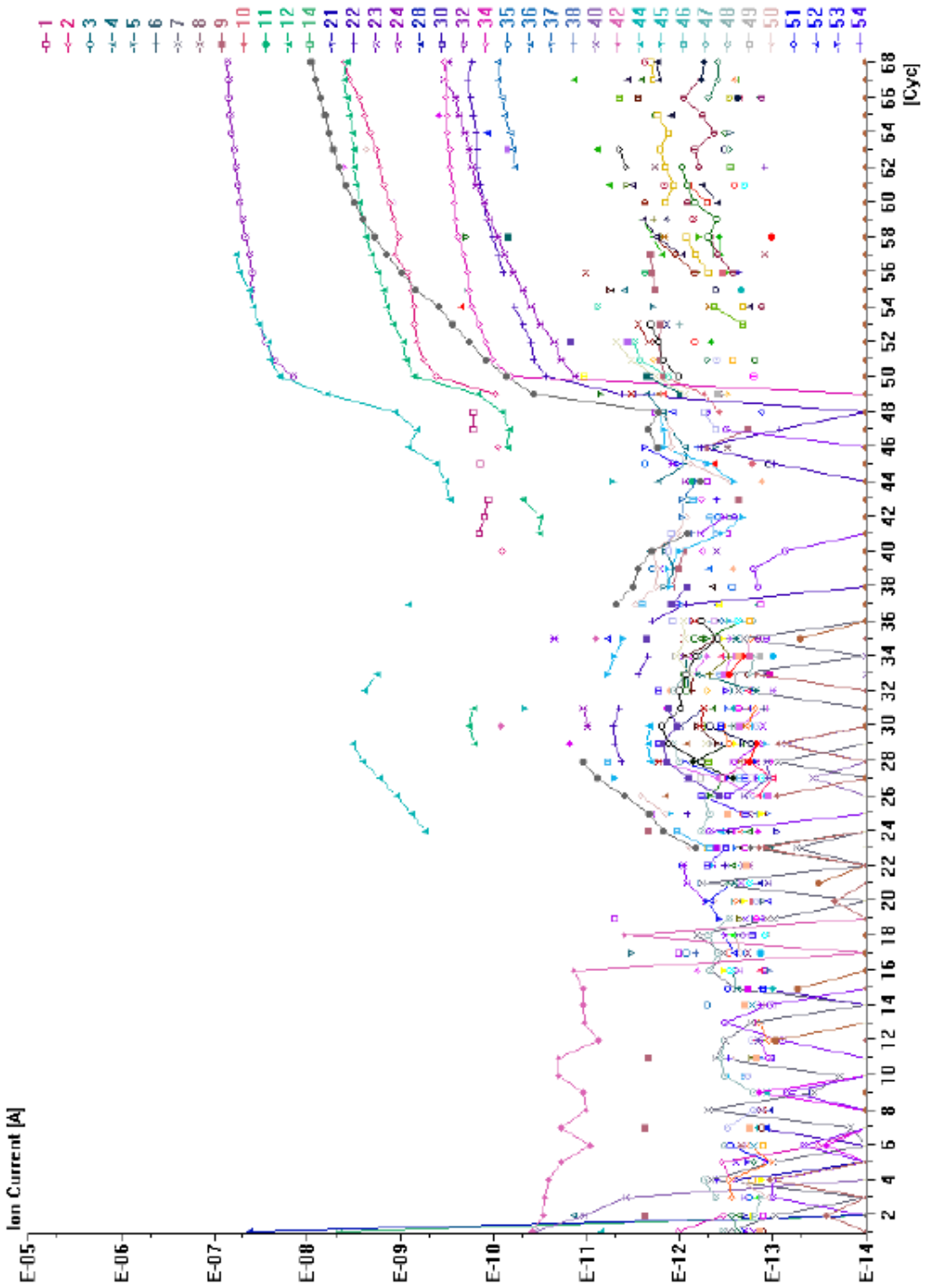

APPENDIX B

A DETAILED INDUCTION OF ELECTRICAL CONDUCTIVITY CALCULATION FOR CARBON BLACK/EPOXY COMPOSITE IN CHARPTER 5

The value of $x_0\left(1-\frac{1}{C}\right)$ is relatively small, so that Taylor polynomial approximation can be applied as follows,

$$\log(x_\infty - x_0)\frac{1}{\log\left(x_\infty - x_0 + x_0\left(1-\frac{1}{C}\right)\right)}$$

$$\approx 1+\frac{x_0\left(\frac{1}{C}-1\right)}{2.303(x_\infty - x_0)\log(x_\infty - x_0)}$$

$$=1+\frac{x_0}{2.303(x_\infty - x_0)\log(x_\infty - x_0)}\left\{\left[1+k(n-1)t\right]^{\frac{1}{n-1}}-1\right\}$$

The value of $k(n-1)t$ is also very small. Applying Taylor polynomial approximation again, it can be found that:

$$1+\frac{x_0}{2.303(x_\infty - x_0)\log(x_\infty - x_0)}\left\{\left[1+k(n-1)t\right]^{\frac{1}{n-1}}-1\right\}$$

$$\approx 1+\frac{x_0 kt}{2.303(x_\infty - x_0)\log(x_\infty - x_0)}$$

So that, we can get:

$$\log\rho=\frac{\log(\rho_0)-\log(\rho_\infty)}{1+\frac{x_0 kt}{2.303(x_\infty - x_0)\log(x_\infty - x_0)}}+\log(\rho_\infty)$$

$$=\frac{\log(\rho_0)-\log(\rho_\infty)}{1+\frac{x_0 k e^{\frac{\log t}{2.303}}}{2.303(x_\infty - x_0)\log(x_\infty - x_0)}}+\log(\rho_\infty)$$

$$=\frac{\log(\rho_0)-\log(\rho_\infty)}{1+e^{\frac{\log t-\log t_c}{\Delta t}}}+\log(\rho_\infty)$$

where

$$\Delta t = \log e = 0.4342$$

$$\log t_c = -\log\left[\frac{x_0 k}{2.303(x_\infty - x_0)\log(x_\infty - x_0)}\right]$$

$$= -\log\left[\frac{x_0}{2.303(x_\infty - x_0)\log(x_\infty - x_0)}\right] - \log(Ae^{\left(-\frac{E_a}{RT}\right)})$$

$$= -\log\left[\frac{Ax_0}{2.303(x_\infty - x_0)\log(x_\infty - x_0)}\right] + \frac{E_a}{2.303RT}$$

APPENDIX C

AUTHOR'S PUBLICATIONS

A.1 JOURNAL PUBLICATIONS

[1]. **Qizhen Liang,** Xuxia Yao, Wei Wang, Yan Liu, Ching Ping Wong, A Three-dimensional Vertical Aligned Functionalized Multilayer Graphene Architecture: An Approach for Graphene-Based Thermal Interfacial Materials (TIMs), *ACS Nano* **2011**, *3*, 2392-401.

[2]. **Qizhen Liang,** Sinsar Alec Hsie, and Ching Ping Wong, An Low-Temperature Solid-state Microwave Reduction of Graphene Oxide For Applications as Transparent Electrical Conductive Coatings on Flexible Polydimethylsiloxane (PDMS), in preparation/submitted.

[3]. **Qizhen Liang,** Kyoung-Sik Moon, Mark The Nyugen, Ken Watkins, Lilian T Morato, Ching Ping Wong. Dynamic Study and Predictive Modeling of Thermal Oxidation Degradation and Electrical Resistivity of In-situ Polymer Ageing Sensors Based on Carbon-Black Filled Epoxy Composites, in preparation/submitted.

[4]. **Qizhen Liang,** Kyoung-Sik Moon, C. P. Wong Enhanced Thermal Conductivity of Polymer Composite by Interfacial Treatment of Fillers, in preparation/submitted.

[5]. **Qizhen Liang,** Xuxia Yao, Sinsar Hsie, *and* Ching Ping Wong, Conductivity of Aligned Functionalized Multilayer Graphene, in preparation/submitted.

A.2 CONFERENCE PUBLICATIONS

[1]. **Qizhen Liang**, Kyoung-Sik Moon, C.P. Wong, "High thermal conductive underfill materials for flip-chip application", PORTABLE-POLYTRONIC 2008. 2nd IEEE International Interdisciplinary Conference on, Garmish-Partenkirchen, German, pp1 – 4, 2008.

[2]. **Qizhen Liang**, Kyoung-Sik Moon, Yuelan Zhang, C.P. Wong. "Low stress and high thermal conductive underfill for cu/low-k application", 58th Electronic Components and Technology Conference, Orlando, FL USA, pp1958-1962, 2008.

[3]. Qizhen Liang, Wei Wang, Kyoung-Sik Moon, C.P. Wong, "Thermal conductivity of epoxy/surface functionalized carbon nano materials", 59th Electronic Components and Technology Conference, San Diego, CA, pp460 – 464, 2009.

[4]. Qizhen Liang, Yonghao Xiu, Wei Lin, Kyoung-Sik Moon, C.P. Wong, "Epoxy/h-BN composites for thermally conductive underfill material", 59th Electronic Components and Technology Conference, San Diego, CA, pp437 – 440, 2009.

A.3 PATENT DISCLOSURE

[1]. Qizhen Liang, Ching Ping Wong, "Vertical Aligned Functionalized Multilayer Graphene Architecture-A throughout approach for graphene-based Thermal Interfacial Materials (TIMs)", GT Disclosure ID 5440.

[2]. Qizhen Liang, Ching Ping Wong, "Polymer transfer process for polymer based thermal interfacial materials (TIMs) from vertically aligned CNTs and aligned ultra thin graphite nano plates/graphene", GT Disclosure ID 4987

[3]. Qizhen Liang, Ching Ping Wong, "Generation of phonon coupler among graphitic nanoplates", GT Disclosure ID 4769

[4]. Qizhen Liang, Ching Ping Wong, "Preparation of Laminated Polymer Composite from Graphitic Nanoplates", GT Disclosure ID 4768

[5]. Qizhen Liang, Ching Ping Wong, "Generation of phonon coupler across the interface between aligned graphitic nanoplates and substrates", GT Disclosure ID 4767

[6]. Qizhen Liang, Ching Ping Wong, "Low stress and high thermal conductive underfill materials for Cu/low k application", GT Disclosure ID 4378

REFERENCES

[1].Geim, A. K.; Novoselov, K. S. The Rise of Graphene. *Nat. Mater.* **2007**, *6*, 183-91.

[2].Novoselov, K. S.; Geim, A. K.; Morozov, S. V.; Jiang, D.; Zhang, Y.; Dubonos, S. V.; Grigorieva, I. V.; Firsov, A. A. Electric field effect in atomically thin carbon films. *Science* **2004**, *306*, 666-9.

[3].Avouris, P.; Chen, Z.; Perebeinos, V. Carbon-based electronics. *Nat. Nanotechnol.* **2007**, *2*, 605-13.

[4].Stoller, M. D.; Park, S. J.; Zhu, Y. W.; An, J. H.; Ruoff, R. S. Graphene-Based Ultracapacitors. *Nano Lett.* **2008**, *8*, 3498-502.

[5].Becerri, H. A.; Mao, J.; Liu, Z.; Stoltenberg, R. M.; Bao, Z. N.; Chen, Y. S. Evaluation of solution-processed reduced graphene oxide films as transparent conductors. *ACS Nano* **2008**, *2*, 463-70.

[6] Watcharotone, S.; Dikin, D. A.; Stankovich, S.; Piner, R.; Jung, I.; Dommett, G. H. B.; Evmenenko, G.; Wu, S. E.; Chen, S. F.; Liu, C. P.; Nguyen, S. T.; Ruoff, R. S. Graphene-silica composite thin films as transparent conductors. *Nano Lett* **2007**; *7*, 1888-92.

[7] Wang, X.; Zhi, L. J.; Mullen, K. Transparent, conductive graphene electrodes for dye-sensitized solar cells. *Nano Lett*, **2008**; *8*, 323-7.

[8].Balandin, A. A.; Ghosh, S.; Bao, W.; Calizo, I.; Teweldebrahn, D.; Miao, F.; Lau, C. N. Superior Thermal Conductivity of Single Layer Graphene. *Nano Letters* **2008**, *8*, 902-7.

[9].Fowler, J. D.; Allen, M. J.; Tung, V. C.; Yang, Y.; Kaner, R. B.; Weiller, B. H. Practical Chemical Sensors from Chemically Derived Graphene. *ACS Nano* **2009**, *3*, 301-06.

[10].http://facweb.bhc.edu/academics/science/harwoodr/geol101/study/minerals.htm

[11].Inagaki, M. New Carbons-Control of Structure and Functions. Amsterdam, Netherlands: Elsevier, 2000.

[12]. Bundy, F. P. Bassett, W. A. Weathers, M. S.; Hemley, R. J. Mao, H. K.; Goncharov, A. F. The pressure-temperature phase and transformation diagram for carbon. *Carbon* **1996**, *34*, 141-53.

[13] Szaho, T.; Berkesi, O.; Fergo, P.; Josepovits, K.; Sanakis, Y.; Petridis, D.; Dekany, I. Evolution of surface functional groups in a series of progressively oxidized graphite oxides. *Chem. Mater.* **2006**; *18*, 2740-9.

[14].Kudin, K. N.; Ozbas, B.; Schniepp, H. C.; Prud'homme, P. K.; Aksay, I. A.; Car, R. Raman spectra of graphite oxide and functionalized graphene sheets. *Nano Lett* **2008**, *8*, 36-41.

[15]. Szabo, T.; Berkesi, O.; Forgo, P.; Josepovits, K.; Sanakis, Y.; Petridis, D.; Dekany, I. Evolution of surface functional groups in a series of progressively oxidized graphite oxide. *Chem. Mater.* **2006**, *18*, 2740-9.

[16].Boukhvalov, D. W.; Katsnelson, M. I. Chemical functionalization of graphene with defects. *Nano Lett.* **2008**, *8*, 4373-9.

[17].Katsnelson, M. I.; Boukhvalov, D. W. Chemical functionalization of graphene. *Journal of Physics: Condensed Matter* **2009**, *21*, 344205.

[18]. Hashimoto, A.; Suenaga, K.; Gloter, A.; Urita, K.; Iijima, S. Direct Evidence for atomic defects in graphene layers. *Nature* **2004**, *430*, 870-3.

[19].Tung, V. C.; Allen, M. J.; Yang, Y.; Kanar, R. B. High-throughput solution processing of large-scale graphene. *Nature Nanotech* **2009**, *4*, 25-9.

[20] Li, D.; Muller, M. B.; Gilje, S.; Kaner, R. B.; Wallace, G. G. Processable aqueous dispersions of graphene nanosheets. *Nature Nanotech* **2008**, *3*, 101-5.

[21].Schwamb, T.; Burg, B. R.; Schirmer, N. C.; Poulikakos, D. An Electrical Method for the Measurement of the Thermal and Electrical Conductivity of Reduced Graphene Oxide Nanostructures. *Nanotechnology* **2009**, *20*, 405704.

[22]. Partonens, B. Peeters, F. M. From graphene to graphite: Electronic structure around the K point. *Physical Review B* **2006**, *74*, 075404.

[23]. Castro Neto, A. H.; Guinea, F.; Peres, N. M. R.; Novoselov, K. S.; Geim, A. K. The electronic properties of graphene, *Review of Modern Physics* **2009**, *81*, 109-62.

[24]. Seol, J. H.; Jo, I.; Moore, A. L.; Linday, L.; Aitken, Z. H.; Pettes, M. T.; Li, X. S.; Yao, Z.; Huang, R.; Broido, D. *et al.* Two-Dimensional Phonon Transport in Supported Graphene. *Science* **2010**, *328*, 213-6.

[25].Khveshchenko, D. V. Magnetic-Field-Induced Insulating Behavior in Highly Oriented Pyrolitic Graphite. *Phys. Rev. Lett.* **2001**, *87*, 206401.

[26].Kato, H.; Baba, T.; Okaji, M. Anisotropic thermal-diffusivity measurements by a new laser-spot-heating technique. *Measurement Sci. Tech.* **2001**, *12*, 2074-80.

[27].Mohr, M.; Maultzsch, J.; Dobardzic, D.; Reich, S.; Milosevic, I.; Damnjanovic, M.; Bosak, A.; Krisch, M.; Thomsen, C. Phonon dispersion of graphite by inelastic x-ray scattering. *Phys. Rev. B*. **2007**, *76*, 035439.

[28].Saito, R.; Jorio, A.; Souza, A. G.; Dresselhaus, G.; Dresselhaus, M. S.; Pimenta, M. A. Probing phonon dispersion relations of graphite by double resonance Raman scattering. *Phys. Rev. Lett.* **2002**, *88*, 027401.

[29].Lee, C.; Wei, X.; Kysar, J. W.; Hone, J. Measurement of the Elastic Properties and Intrinsic Strength of Monolayer Graphene. *Science* **2008***, 321*, 385-8.

[30]. http://www.gizmag.com/graphene-supercapacitor-energy-density-record/17188/

[31].Ando, T.; Zheng, Y.; Suzuura, H. Dynamical conductivity and zero-mode anomaly in honeycomb lattice. *J. Phys. Soc. Jpn*. **2002**, *71*, 1318-24.

[32].Gusynin, V. P.; Sharapov, S. G.; Carbotte, J. P. Unusual microwave response of Dirac quansiparticles in graphene. *Phys. Rev.Lett.* **2006,** *96*, 256802.

[33].Kuzmenko, A. B.; van Heumen, E.; Carbone, F.; van der Marel, D. Universal optical conductance of graphite. *Phys. Rev. Lett.* **2008**, *100*, 117401.

[34]. Nair, R. R.; Blake, P.; Grigorenko, A. N.; Noveselov, K. S.; Booth, T. J.; Stauber, T.; Peres, N. M. R.; Geim, A. K.; Fine structure constant defines visual transparency of graphene. *Science* **2008**, *320*, 1308.

[35].Eda, G.; Fanchini, G.; Chhowalla, M. Large-area ultrathin films of reduced graphene oxide as a transparent and flexible electronic material. *Nature Nanotechnology* **2008**, *3*, 270-4.

[36].Novoselov, K. S.; Jiang, D.; Schedln, F.; Booth, T. J. Khotkevich, V. V.; Morozov, S. V.; Gelm, A. K. Two-dimensional atomic crystals. *Proceedings of the National Academic Society* **2005**, *102*, 10451-3.

[37].Berger, C.; Song, Z. M.; Li, T. B.; Li, X. B.; Ogbazghi, A. Y.; Feng, R.; Dai, Z. T.; Marchenkov, A. N.; Conrad, E. H.; First, P. N.; de Heer W. A. Ultrathin Epitaxial Graphite 2D Electron Gas Properties and a Route toward Graphene-based Nanoelectronics, *J. Phys. Chem. B* **2004**, *108*,19912-6.

[38].Reina, A.; Jia X. T.; Ho, J.; Nezich, D.; Son, H. B.; Bulovic, V.; Dresselhaus, M. S.; Kong, J. Large area, few-layer graphene films on arbitrary substrates. *Nano Lett.* **2009**, *9*, 30-35.

[39]. Kim, K. S.; Zhao, Y.; Jang, H. Lee, S. Y.; Kim, J. M.; Kim, K. S..; Ahn, J. –H.; Kim, P.; Choi, J. –Y.; Hong, B. H. Large-scale pattern growth of graphene films for stretchable transparent electrodes. *Nature* **2009**, *457*, 706-10.

[40]. Shen, T.; Gu, J. J.; Xu, M.; Wu, Y. Q.; Bolen, M. L.; Capano, M. A.; Engel, L. W.; Ye P. D. Observation of quantum-Hall effect in gated epitaxial graphene grown on SiC (0001). *Appl. Phys. Lett.* **2009**, *95*, 172105.

[41].Wu, X. S.; Hu, Y. K.; Ruan, M.; Madiomanana, N. K.; Hankinson, J.; Sprinkle, M.; Berger, C.; de Heer W. A. Half integer quantum Hall effect in high mobility single layer epitaxial graphene. *Appl. Phys. Lett.* **2009**, *95*, 223108.

[42]. Hass, J.; Varchon, F.; Millan-Otoya, J. E.; Sprinkle, M.; Sharma, N.; de Heer, W. A.; Berger, C.; First, P. N.; Magaud, L.; Conrad, E. H. Why multilayer graphene on 4H-SiC(0001) behaves like a single sheet of graphene. *Phys. Rev. Lett.* **2008**, *100*, 125504.

[43].Kedzierski, J.; Hsu; P. –L.; Healey, P.; Wyatt, P.W.; Keast, C. L.; Sprinkle, M.; Berger, C.; de Heer, W.A. Epitaxial Graphene Transistors on SiC Substrates *IEEE transaction on Electron Devices* **2008**, *55*, 2078–85.

[44]. Sutter, P. W.; Flege, J. I.; Sutter E. A. Epitaxial graphene on ruthenium. *Nature Mater.* **2008**, *7*, 406-11.

[45]. Pletikosic, I.; Kralj, M.; Pervan, P.; Brako, R.; Coraux, J.; N'Diaye, A. T.; Busse, C.; Michely, T. Dirac Cones and Minigaps for Graphene on Ir(111). *Physical Review Letters* **2009**, *102*, 056808.

[46]. Li, X. S.; Cai, W. W.; An, J.; Kim, S.; Nah, J.; Yang, D. X.; Piner, R.; Velamakanni, A.; Jung, I.; Tutuc, E.; Banerjee, S. K.; Colombo, L.; Ruoff, R. S. Large-Area Synthesis of High-Quality and Uniform Graphene Films on Copper Foils. *Science* **2009**, *324*, 1312

[47].McAllister, M. J.; Li, J. L.; Adamson, D. H.; Schniepp, H. C.; Abdala, A. A.; Liu, J.; Herrera-Alonso, O. M.; Milius, D. L.; Car, R.; Prud'homme, R. K.; Aksay, I. A. Single Sheet Functionalized Graphene by Oxidation and Thermal Expansion of Graphite. *Chem. Mater*. **2007**, *19*, 4396-404.

[48] Gemez-Navarro, C.; Weitz, R. T.; Bittner, A. M.; Scolari, M.; Mews, A.; Burghard, M.; Kern, K. Electronic transport properties of individual chemically reduced graphene oxide sheets. *Nano Lett* **2007**, *7*, 3499-503.

[49] Hummers, W. S.; Offeman, J. R. E. Preparation of graphitic oxide. *J Am Chem Soc* **1958**, *80*, 1339-9.

[50].Schniepp, H. C.; Li, J.-L.; McAllister, M. J.; Sai, H.; Herrera-Alonso, M.; Adamson, D. H.; Prud'homme, R. K.; Car, R.; Saville, D. A.; Aksay, I. A. Functionalized Single Graphene Sheets Derived from Splitting Graphite Oxide. *J. Phys. Chem. B*, **2006**, *110*, 8535.

[51]. Stankovich, S.; Dikin, D. A.; Piner, R. D.; Kohlhass, K. A.; Kleinhammes, A.; Jia, Y.; Wu, Y. Nguyen, S. T.; Ruoff, R. S.; Synthesis of graphene-based nanosheets via chemical reduction of exfoliated graphite oxide. *Carbon* **2007**, *45*, 1558-65.

[52]. Schniepp, H. C.; Li, J. L.; McAllister, M. J.; Sai, H.; Herrera-Alonso, M.; Adamson, D. H.; Prud'homme, R. K.; Car, R.; Saville, D. A.; Aksay, I. A. Functionalized single graphene sheets derived from splitting graphite oxide. *J. Phys. Chem. B* **2006**, *110*, 8535-9.

[53]. Gilje, S.; Han, S.; Wang, M. S.; Wamg. K. L.; Kaner, R. B. A chemical route to graphene for device applications. *Nano Lett.* **2007**, *7*, 3394-8.

[54].Veca, L. M.; Meziani, M. J.; Wang, W.; Wang, X.; Lu, F. S.; Zhang, P. Y.; Lin, Y.; Fee, R.; Connell, J. W.; Sun, Y. P. Carbon Nanosheets for Polymeric Nanocomposites with High Thermal Conductivity. *Adv. Mater.* **2009**, *21*, 2088-92.

[55].Eda, G.; Chhowalla, M. Chemically Derived Graphene Oxide: Towards Large-Area Thin-Film Electronics and Optoelectronics. *Adv. Mater.* **2010**, *22*, 2392-415.

[56].Stankovich, S.; Dikin, D. A.; Dommett, G. H. B.; Kohlhaas, K. M.; Zimney, E. J.; Stach, E. A.; Piner, R. D.; Nguyen, S. T.; Ruoff, R. S. Graphene-based composite materials.*Nature* **2006**, *442*, 282-6.

[57].Dikin, D. A.; Stankovich, S.; Zimney, E. J.; Piner, R. D.; Dommett, G. H. B.; Evmenenko, G.; Nguyen, S. T.; Ruoff, R. S. Functionalized Graphene Sheets for Polymer Nanocomposites. *Nature* **2007**, *448*, 457-60.

[58]. Yakobson, B. J.; Brabec, C. J.; Bernholc, J. Nanomechanics of carbon tubes: Instabilities beyond linear response. *Phys. Rev. Lett.* **1996**, *76*, 2511-4.

[59]. Thostenson, E. T.; Ren, Z. F.; Chou, T. W. Advances in the science and technology of carbon nanotubes and their composite: a review. *Composite Science and Technology* **2001**, *61*, 1899-1912.

[60]. Tasis, D.; Tagmatarchis, N.; Bianco, A.; Prato, M. Chemistry of carbon nanotubes. *Chemical Reviews* **2006**, *106*, 1105-36.

[61]. Javey, A.; Guo, J.; Wang, Q.; Lunstrom, M.; Dai, H. J.; Ballistic carbon nanotube field effect transistors. *Nature* **2003**, *424*, 654-7.

[62]. Zhu, L. B.; Hess, D. W.; Wong, C. P. Assembling carbon nanotube films as thermal interfacial materials. *Electronic Components and Technology Conference* **2007**, 2006-10.

[63]. Wang, X. W.; Zhong, Z. R.; Xu, J. Noncontact Thermal Characterization of Multiwall Carbon Nanotubes. *J. Appl. Phys.* **2005**, *97*, 064302

[64]. Hu, X. J.; Padilla, A. A.; Xu, J.; Fisher, T. S.; Goodson, L. E. 3-Omega Measurements of Vertically Oriented Carbon Nanotubes on Silicon. *J. Heat Transf.* **2006***, 128,* 1109-13.

[65]. Cola, B. A.; Xu, J.; Cheng, C. R.; Xu, X. F.; Fisher, T. S.; Hu H. P. Photoacoustic Characterization of Carbon Nanotube Array Thermal Interfaces. *J. Appl. Phys.* **2007**, *105*, 054313.

[66]. Lin, W.; Zhang, R.; Moon, K. S.; Wong, C. P. Molecular Phonon Couplers at Carbon Nanotube/Substrate Interface to Enhance Interfacial Thermal Transport. *Carbon* **2010**, *48*, 107-13.

[67].Prasher, R. Graphene Spreads the Heat. *Science* **2010**, *328*, 185-6.

[68]. Biscoe, J.; Warren, B. E. An X-ray study of carbon black. *J. Appl. Phys.* **1942**, *13*, 364-71.

[69]. Boehm, H. P. Some aspects of the surface-chemistry of carbon-blacks and other carbons. *Carbon* **1994**, *32*, 759-69.

[70]. Medalia, A. I. Effect of carbon-black on dynamic properties of rubber vulcanizates. *Rubber Chemistry and Technology* **1978**, *51*, 437-523.

[71].http://www.momentiveceramics.com/downloads/documents/81501.pdf.

[72]. Liu, L.; Feng, Y. P.; Shen, Z. X. Structural and electronic properties of h-BN, *Physical Review B* **2003**, *68*, 104102.

[73].http://accuratus.com/silicar.html

[74].Harris, G. L. *Properties of silicon carbide.* **1995:** INSPEC, the Institute of Electrical Engineers London, United Kingdom.

[75]. http://www.esk.com/en/products-brands/products/sealing-components/gas-seal-rings.html

[76]. http://www.microwaves101.com/encyclopedia/siliconcarbide.cfm

[77].Allen, M. J.; Tung, W. C.; Gomez, L.; Xu, Z.; Chen, L. M.; Nelson, K. S.; Zhou, C.; Kaner, R. B.; Yang, Y. Soft Transfer Printing of Chemically Converted Graphene *Adv. Mater.* **2008***, 21*, 2098-102.

[78].Bogdal, D. Microwave-Assisted Organic Synthesis One Hundred Reaction Procedures. *Tetrahedron Organic Chemistry Series* **2005**, vol 25, ed Bckvall J-E, Baldwin J E and Williams R M (Amsterdam: Elsevier), p13-22

[79].de la Hoz, A.; Diaz-Ortiz, A.; Moreno, A. Microwaves in organic synthesis. Thermal and non-thermal microwave effects. *Chem. Soc. Rev.* **2005**, *34*, 164-78.

[80].Stuerga, D.; Delmotte, M. *Microwave in Organic synthesis* **2002,** vol 1, ed Loupy A (Weinheim:Wiley-VCH), p1-35

[81].Murugan, A. V.; Muraliganth, T.; Manthiram, A. Rapid, facile microwave-solvothermal synthesis of graphene nanosheets and their polyaniline nanocomposites for energy storage *Chem. Mater.* **2009**, *21*, 5004-6.

[82].Booske, J. H.; Cooper, R. F.; Freeman, S. A. Microwave enhanced reaction kinetics in ceramics. *Mater. Res. Innov.* **1997***, 1,* 77-84.

[83].Lin, W.; Moon, K.-S.; Zhang, S. J.; Ding, Y.; Shang, J. T.; Chen, M. X.; Wong, C. P. Microwave makes carbon nanotubes less defective. *ACS Nano* **2010***, 4,* 1716-22.

[84].Wong, C. P.; Bollampally, R. S. Thermal conductivity, elastic modulus, and coefficient of thermal expansion of polymer composites filled with ceramic particles for electronic packaging. *J. Appl.Polym. Sci.* **1999**, *74*, 3396-403.

[85].Stan, M. R.; Burleson, W. P. Bus-invert coding for low-power I/O. *IEEE Transactions on Very Large Scale Integration (VLSI) Systems* **1995**, *3*, 49-58.

[86].Borkar, S. Y. Design challenges of technology scaling. *IEEE Micro.* **1999**, *19*, 23-9.

[87].Meindl, J. D. Low Power Microelectronics: Retrospect and Prospect. *Proceedings of the IEEE* **1995***, 83*, 619-635.

[88].Narendran, N.; Gu, Y. Life of LED-Based based white light sources. *IEEE/OSA Journal of Display Technology* **2006**, *1*, 167-71.

[89].Kapur, P.; McVittie J. P.; Saraswat**,** K. C. Technology and reliability constrained future copper interconnects. I. Resistance modeling. *IEEE transaction on Electron Device*, **2002**, *49*, 590-7.

[90].Obreja, V. V. N. On the Reliability of Power Silicon Rectifier Diodes above the Maximum Permissible Operation Junction Temperature. *Industrial Electronics, 2006 IEEE International Symposium on,* **2006**, *2*, 835-40.

[91].Yoon, Y. G.; Mazzoni, M.; Choi, H. J.; Ihm, J.; Louie, S. G. Structural deformation and intertube conductance of crossed carbon nanotube junctions. *Phys. Rev. Lett.* **2001**, *86*, 472-5.

[92].Zhu, L. B.; Wong C. P. et al. Aligned Carbon Nanotube Stacks by Water-Assisted Selective Etching. *Nano Letters*, **2005**, *5*, 2641-5.

[93]. Hone, J.; et al. Thermal Properties of Carbon Nanotubes and Nanotube-Based Materials," *Appl. Phys. A-Materials Science & Processing* **2002**, *74*, 339-43.

[94].de Heer, W. A.; Bacsa, W.; Gerfin, T.; Baker, R. H.; Forro, L.; Ugarte, D. Aligned Nanotube Films: Production and Optical and Electronic Properties. *Science* **1995**, *268*, 845-7.

[95].Baughman, R. H.; Zakhidov, A. A.; de Heer, W. A. Carbon Nanotubes—the Route Toward Applications *Science* **2002***, 297*, 787.

[96].Kim, P.; Shi, L.; Majumdar, A.; McEuen, P. L. Thermal transport measurements of individual multiwalled nanotubes. *Phys. Rev. Lett* **2001**, 87, 215502.

[97]. Biercuk, M. J.; et al. Carbon Nanotube Composites for Thermal Management. *Phys Lett.* **2002**, *80*, 2767-9.

[98].Yu, A. P.; et al. Effect of Single-Walled Carbon Nanotube Purity on the Thermal Conductivity of Carbon Nanotube-based Composites. *Appl. Phys. Lett.* **2006**, *89*, 133102.

[99].de Heer, W. A.; Berger, C.; Wu, X.; First, P. N.; Conrad, E. H.; Li, X.; Li, T.; Sprinkle, M.; Hass, J.; Sadowski, M. L.; Potemski, M.; Martinez G. Epitaxial graphene. *Solid State Communications* **2007**, *143*, 92-100.

[100].Rollings, E.; Gweon, G.-H.; Zhou, S. Y.; Mun, B. S. McChesney, J. L.; Hussain, B. S.; Fedorov, A. V.; First, P. N.; de Heer, W. A.; Lanzara, A. Synthesis and characterization of atomically thin graphite films on a silicon carbide substrate. *J. Phys. Chem. Solids* **2006**, *67*, 2172-7.

[101].Akturk, A.; Goldsman, N. Electron transport and full-band electron-phonon interactions in graphene. *J. Appl. Phys.* **2008**, *103*, 053702.

[102]. Tombros, Nikolaos; et al. Electronic spin transport and spin precession in single graphene layers at room temperature. *Nature* **2007**, *448*, 571–5.

[103].Saito, K.; Nakamura, J.; Natori, A. Ballistic thermal conductance of a graphene sheet. *Phys. Rev. B* **2007**, *76*, 115409.

[104]. Lidstorm, P. Tierney, J. Wathey, B.; Westman, J. Microwave assisted organic synthesis – a review. *Tetrahedron* **2001**, *57*, 9225-83.

[105]. Kappe, C. O.; Controlled microwave heating in modern organic synthesis. Angewante Chemie-International Edition 2004, 43, 6250-84.

[106]. Varma, R. S. Solvent-free organic synthesizes – using supported reagents and microwave irradiation. *Green Chemistry* **1999**, *1*, 43-5.

[107]. Ferrari, A. C.; Meyer, J. C.; Scardaci, V.; Casiraghi, C.; Lazzeri, M.; Piscanec, S.; Jiang, D.; Novoselov, K. S.; Roth, S.; Geim, A. K. Raman Spectrum of Graphene and Graphene Layers. *Phys. Rev. Lett.* **2006**, *97*, 187401.

[108].Kurabayashi, K.; Goodson, K. E. Impact of molecular orientation on thermal conduction in spin coated polyimide films. *J. Appl. Phys.* **1999**, *86*, 1925-31.

[109].Park, S.; Lee, K.-S.; Bozoklu, G;, Cai, W.; Nguyen, S. T.; Ruoff, R.S. Graphene oxide papers modified by divalent ions- Enhancing mechanical properties via chemical cross-linking. *ACS Nano* **2008**, *2*, 572-8.

[110].Paek, S. M.; Yoo, E.; Honma, I. Enhanced cyclic performance and lithium strorage capacity of SiO_2/graphene nanoporous electrodes with three-dimensionally delaminated flexible structure. *Nano Lett.* **2009**, *9*, 72-5.

[111] Wagner, C. D.; Davis, L. E.; Zeller, M. V.; Taylor, J. A.; Raymond, R. H.; Gale, L. H. Empirical Atomic Sensitivity Factors for Quantitative-Analysis by Electron-Spectroscopy for Chemical-Analysis, Surf. Interface Anal. 1981, 3, 211—225

[112].Reich, S.; Thomson, C. Raman Spectroscopy of Graphite. *Phil. Trans. R. Soc. Lond. A* **2004**, *362*, 2271-88.

[113].Gommans, H. H.; Alldredge, J. W.; Tashiro, H.; Park, J.; Magnuson, J. Fibers of Aligned Single-Walled Carbon Nanotubes: Polarized Raman Spectroscopy. *J. Appl. Phys.* **2000**, *88*, 2509-14.

[114].Rao, A. M.; Jorio, A.; Pimenta, M. A.; Dantas, M. S. S.; Saito, R.; Dresselhaus, G.; Dresselhaus, M. S. Polarized Raman Study of Aligned Multiwalled Carbon Nanotubes. *Phys. Rev. Lett.* **2000**, *84*, 1820-3.

[115] Sun, H. D.; Tang, Z. K.; Chen, J.; Li, G. Polarized Raman spectra of single-wall carbon nanotubes mono-dispersed in channels of AlPO4-5 single crystals. *Solid State Commun.* **1999**, *109*, 365-9.

[116].Ajiki, H.; Ando, T. Aharonov-Bohm Effect in Carbon Nanotubes. *Physica B* **1994**, *201*, 349-52.

[117]Jiang, J-.W.; Tang, H.; Wang, B. -S.; Su, Z. -B. Raman and Infrared properties and layer dependence of the phonon dispersions in multilayered graphene.*Physical Review B* **2008**, *77*, 235421.

[118] Saha, S. K.; Waghmare, U. V.; Krishnamurthy, H. R.; Sood, A. K. Phonons in few-layer graphene and interplanar interaction: A first-principles study. *Physical Review B* **2008**, *78*, 165421.

[119].Tsang, D. K. L.; Marsden, B. J.; Fok, S. L.; Hall, G. Graphite Thermal Expansion Relationship for Different Temperature Ranges. *Carbon* **2005**, *43*, 2902-6.

[120].Maniwa, Y.; Fujiwara, R.; Kira, H.; Tou, H.; Kataura, H.; Suzuki, S.; Achiba, Y.; Nishibori, E.; Takata, M.; Sakata, M. et al. Thermal Expansion of Single-Walled Carbon Nanotube (SWNT) Bundles: X-ray Diffraction Studies. *Phys. Rev. B* **2001**, *64*, 241402.

[121].Yosida, Y. High-temperature shrinkage of single-walled carbon nanotube bundles up to 1600K. *J. Appl. Phys.* **2000**, *87*, 3338-41.

[122].Jiang, H.; Liu, B.; Huang, Y. Hwang, K. C. Thermal expension of single wall carbon nanotubes. *J. Eng. Mater. Tech. – Transaction of the ASME* **2004**, *126*, 265-70.

[123].Tong, T.; Zhao, Y.; Delzeit, L.; Kashani, A.; Meyyappan, M.; Majumdar, A. Dense, vertically aligned multiwalled carbon nanotube arrays as thermal interfacial materials. *IEEE Trans. Compon. Pack. Technol.* **2007**, *30*, 92-100.

[124]. Xu, J.; Fisher, T. S. Enhancement of Thermal Interface Materials with Carbon Nanotube Arrays. *Int. J. Heat. Mass. Transf.* **2006**, *49*, 1658-66.

[125].Ngo, Q.; Cruden, B. A.; Cassell, A. M.; Sims, G.; Meyyappan, M.; Li, J.; Yang, C. Y. Thermal Interface Properties of Cu-Filled Vertically Aligned Carbon Nanofiber Arrays. *Nano Lett.* **2004**, *4*, 2403-7.

[126]. Robinson, J. A.; LaBella, M.; Trumbull, K. A.; Weng, X. J.; Cavelero, R.; Daniels, T.; Hughes, Z.; Hollander, M.; Fanton, M.; Snyder, D. Epitaxial Graphene Materials Integration: Effects of Dielectric Overlayers on Structural and Electronic Properties. *ACS Nano* **2010**, *4*, 2667-72.

[127].Chen, H.; Muller, M. B.; Gilmore, K. J.; Wallace, G. G.; Li, D. Mechanically Strong, Electrically Conductive, and Biocompatible Graphene Paper. *Adv. Mater.* **2008**, *20*, 3557-61.

[128]. Wei, Z. Q.; Wang, D. B.; Kim, S.; Kim, S-.Y.; Hu, Y. K.; Yakes, M. K.; Laracuente, A. R.; Dai, Z. T.; Marder, S. R.; Berger, C. et al. Nanoscale Tunable Reduction of Graphene Oxide for Graphene Electronics. *Science* **2010**, *328*, 1373-6.

[129].Danilov, N. A.; Krylov, Yu. S.; Korpusov, G. V.; Kostikova, G. V.; Barabanov, I. R.; Bezrukov, L. B.; Kornoukhov, V. N.; Novikova, G. Ya.; Yanovich, E. A.; Nesterova, N. P. *et al.* A Study of Indium Extraction with Carboxylic Acids with the Aim to Produce Scintillators for Solar Neutrino Detection by LENS Spectroscopy of Low-Energy Neutrino. *Radiochemistry* **2005**, *47,* 487-93.

[130]. Rajesh, N.; Subramanian, M. S. Extractive Separation and Determination of Thallium and Indium by Liquid Scintillation Counting. *Analyst* **1994***, 119,* 2071-4.

[131]. Jiang, D. E.; Sumpter, B. G.; Dai, S. How Do Aryl Groups Attach to a Graphene Sheet? *J. Phys. Chem.* **2006**, *47*, 23628-32.

[132]. Kim, J.; Cote, L. J.; Kim, F.; Yuan, W.; Shull, K. R.; Huang, J. Graphene Oxide Sheets at Interfaces. *J. Am. Chem. Soc.* **2010**, *132*, 8180-6.

[133]. Yuge R.; Zhang, M. F.; Tomonari, M.; Yoshitake, T.; Iijima, S.; Yudasaka, M. Site Identification of Carboxyl Groups on Graphene Edges with Pt Derivatives. *ACS Nano* **2008**, *2*, 1865-70.

[134]. Ajayan, P. M.; Iijima, S. Capillary-Induced Filling of Carbon Nanotubes. *Nature* **1993***, 361*, 333-4.

[135]. Ajayan, P. M.; Ebbesen, T. W.; Ichihashi, T.; Iijima, S. Opening Carbon Nanotubes with Oxygen and Implications for Filling. *Nature* **1993***, 362,* 522-5.

[136]. Dujardin, E.; Ebbesen, T. W.; Hiura, H.; Tanigaki, K. Capillary and Wetting of Carbon Nanotubes. *Science* **1994**, 265, 1850-2.

[137]. Zhu, L. B.; Sun, Y. Y.; Hess, D. W.; Wong, C. P. Well-Aligned Open-Ended Carbon Nanotube Architectures: An Approach for Device Assembly. *Nano Lett.* **2006**, *6*, 243-7.

[138]. Xiu, Y. H.; Zhu, L. B.; Hess, D. W.; Wong, C. P. Biomimetic Creation of Hierarchical Surface Structures by Combining Colloidal Self-Assembly and Au Sputter Deposition. *Langmuir* **2006**, *22*, 9676-81.

[139]. Zhu, L. B.; Xiu, Y. H.; Xu, J.; Tamirisa, P. A.; Hess, D. W.; Wong, C. P. Superhydrophobicity on Two-tier Rough Surfaces Fabricated by Controlled Growth of Aligned Carbon Nanotube Arrays Coated with Fluorocarbon. *Langmuir* **2005**, *21*, 11208-12.

[140]. Futaba, D. N.; Hata, K.; Yamaha, T. Hiraoka, T.; Hayamizu, Y.; Kakudate, Y.; Tanaike, O.; Hatori, H.; Yumura, M.; Iijima, S. Shape-Engineerable and Highly Densely Packed Single-Walled Carbon Nanotubes and Their Applications as Super-Capacitor Electrodes. *Nat. Mater.* **2006**, *5*, 987-94.

[141].Eatah, A. I.; Ghani, A. A.; Hasham, A. A. Effect of concentration and temperature on the electrical-conductivity for butyl rubber loaded with different types of carbon-black. *Polym. Degrad. Stab.* **1989**, *23*, 9-18.

[142].Gillen, K. T.; Celina, M.; Clough, R. L. Density measurements as a condition monitoring approach for following the ageing o f nuclear power plant cable materials. *Radiat. Phys. Chem.* **1999**, *56*, 429-47.

[143].Mason, L. R.; Reynolds, A. B. Standardization of oxidation induction time testing used in life assessment of polymeric electric cables. *J. Appl. Polym. Sci.* **1997**, *66*, 1691-702.

[144].Watkins, K.; Morris, S.; Wong, C. P.; Luo, S.; Masakowski, D. D. U.S. Pat. Pending.

[145].Sun, Y. Y.; Luo, S.; Watkins, K.; Wong, C. P. Electrical approach to monitor the thermal oxidation ageing of carbon black filled ethylene propylene rubber. *Polym. Degrad. Stab.* **2004**, *86*, 209-15.

[146].Sun, Y. Y.; Fan, L.; Watkins, K.; Peak, J.; Wong, C. P. An electrical approach to monitor wire and cable thermal oxidation ageing condition based on carbon black filled conductive polymer composite. *J. Appl. Polym. Sci.* **2004**; *93*, 513-20.

[147].Grassie, N.; Guy, M. I.; Tennent, N. H.; Degradation of epoxy polymers 2: Mechanism of thermal-degradation of bisphenol-A diglycidyl ether. *Polym. Degrad. Stab.* **1985**, *13*, 11-20.

[148].Grassie, N.; Guy, M. I.; Tennent, N. H. Degradation of epoxy polymers 4 Thermal-degardation of bis-phenol A diglycidyl ether cured with ethylene diamine. *Polym. Degrad. Stab.* **1986**, *14*, 125-37.

[149].Chen, J. -S.; Ober, C. K.; Poliks, M. D.; Zhang, Y.; Wiesner, U.; Cohen, C. Controlled degradation of epoxy networks: analysis of crosslink density and glass transition temperature changes in thermal reworkable thermosets. *Polymer* **2004**, *45*, 1939-50.

[150].Chen, J. -S.; Ober, C. K.; Poliks, M. D.; Zhang, Y. Charaterization of thermal reworable thermosets: materials for environmentally friendly processing and reuse. *Polymer* **2004**, *43*, 131-9.

[151].Levchik, S. V.; Weil, E. D. Thermal decomposition, combustion and flame-retardancy of epoxy resins – a review of recent literature. *Polym. Int.* **2004**, 53, 1901-29.

[152].Teyssandier, F.; Sun, Y. Y.; Wong, C. P.; Love, B. J.; Cure versus flow in dispersed chip-underfill materials. *Macrom. Mater. and Eng.* **2008**, *293*, 828-31.

[153].Greenberg, A. R.; Kamel, I. Kinetics of anhydride Formation in Poly(acrylic Acid) and its effect on the properties of a PAA-Alumina composite, *J. Polym. Sci.: Polym. Chem. Ed.* **1977**, *15*, 2137-49.

[154].Liang, N. T.; Shan, Y.; Wang, S. –Y. Electrical conductivity and percolation theory in aggregated films. *Phys. Rev. Lett.* **1976**, 37, 526-9.

[155].Jacques, L. F. E.; Accelerated and outdoor/natural exposure testing of coatings. *Progress in polymer science* **2000**, *25*, 1337-62.

[156].Yin, X. K.; Sheng, B. Z.; Some aspects of accelerated life testing by progressive stress. *IEEE transactions on reliability* **1987**, *36*, 150-5.

[157]. Suryanarayana, D.; Hsiao, R.; Gall, T. P.; Mccreary, J. M. Enhancement of flip-chip fatigue life by encapsulation, *IEEE transactions on components hybrids and manufacturing technology* **1991**, *14*, 218-23.

[158]. Kusunose, T. Sekino, T. Choa, Y. H. Nihara, K. Fabrication and microstructure of silicon nitride/boron nitride nanocomposites. *Journal of the American Ceramic Society* **2002**, *85*, 2678-88.

[159]. Eichler, J.; Lesniak, C. Boron nitride (BN) and BN composite for high-temperature applications. *Journal of the European Ceramic Society* **2008**, *28*, 1105-9.

[160]. Alpert, C. J.; Devgan, A.; Kashyap, C. V. RC delay matrics for performance optimization. *IEEE transactions on computer-aided design of integrated circuits and systems* **2005**, *24*, 849-61.

[161]. Lin, T. M.; Mead, C. A. Signal delay in general RC-networks. *IEEE transaction on computer-aided design of integrated circuit and systems* **1984**, *3*, 331-49.

[162]. Han, S. J.; Wang, K. K. Analysis of the flow of encapsulant during underfill encapsulation of flip-chip. *IEEE transactions on components packing and manufacturing technology Part B-Advanced Packaging* **1997**, *20*, 424-33.

[163]. Nguyen, L.; Quentin, C.; Fine, P.; Cobb, B.; Bayyuk, S.; Yang, H.; Bidstrup-Allen, S. A. Undefill of flip-chip on laminate: Simulation and validation. *IEEE transaction on components and packaging technologies* **1999**, *22*, 168-76.

[164]. Chen, L.; Zhang Q.; Wang, G. Z.; Xie, X. M.; Cheng, Z. N. The effect of underfill and its material models on thermomechanical behaviors of a flip-chip package. *IEEE Transactions on Advanced Packaging* **2001**, *24*, 17-24.

[165]. Wong, C. P., Shi, S. H.; Jefferson, G. High performance no-flow underfills for low-cost flip-chip applications: Material characterization. *IEEE Trans. Compon. Packag. Manufact. Tech. Part A.* **1998**, *21*, 450-8.

[166]. Yeh, E. C. C.; Choi, W. J.; Tu, K. N.; Elenius, P.; Balkan, H. Current-crowding-induced electromigration failure in flip chip solder joints. *Appl. Phys. Lett.* **2002**, *80*, 580-2.

[167].Xu Y. S.; Chuang, D. D. L. Increasing the thermal conductivity of boron nitride and aluminum nitride particle epoxy-matrix composites by particle surface treatments. *Composite Interfaces* **2000**, *7*, 243–256.

[168].Lee, W. S.; Yu, J. Comparative study of thermally conductive fillers in underfill for the electronic components. *Diamond & Related Materials* **2006**, 14, 1647-53.

[169].Yung, K. C.; Liem, H. Enhanced Thermal Conductivity of Boron Nitride Epoxy-Matrix Composite Through Multi-Modal Particle Size Mixing. *J. Appl. Polym. Sci.* **2007**, *106*, 3587–91.

[170]. Jancar, J.; Dibenedetto, A. T. The mechanical-properties of ternary composites of polypropylene with inorganic fillers and elastomer inclusions. *J. Mater. Sci.* **1994**, *29*, 4651-8.

[171]. Tavman, I. H. Thermal and mechanical properties of copper powder filled poly(ethylene) composites. *Powder Technology* **1997**, *91*, 63-7.

[172]. Tavman, I. H. Effective thermal conductivity of isotropic polymer composites. *International Communications in Heat and Mass Transfer* **1998**, *25*, 723-32

[173]. He, H.; Fu, R. L.; Han, Y. H. Shen, Y.; Song, X. F. Thermal conductivity of ceramic particle filled polymer composites and theoretical predictions. *J. Mater. Sci.* **2007**, *42*, 6749-54.

[174]. Pal, R. On the Lewis-Nielsen model fo thermal/electrical conductivity of composites. *Composites Part A-Applied Science and Manufacturing* **2008**, *39*, 718-26.

[175]. Hauser, R. A.; Keith, J. M. King, J. A.; Holdren, J. L. Thermal conductivity models for single and multiple filler carbon/liquid crystal polymer composites. *J. Appl. Polym. Sci.* **2008**, *110*, 2914-23.

[176]. Singh, R.; Sharma, P. K. Effective thermal conductivity of metal filled polymer composites. *Indian Journal of Pure & Applied Physics* **2011**, *49*, 112-6.

[177]. Mishra, S.; Mukherji, A. Studies of thermal conductivity of nano $CaCO_3$/HIPS composites by unsteady state technique and simulation with Nielsen's model. *Polymer-Plastics Technology and Engineering* **2007**, *46*, 239-44.

[178].Bohr, M. T. Interconnect Scaling -The Real Limiter to High Performance ULSI. in *Proc. IEEE International Electron. Devices Meeting* **1995**, 241-2.

[179]Zhang, Y. X.; Hu, X. Y.; Zhao, J. H.; Sheng, K.; Cannon, W. R.; Wang, X. H.; Fursin, L. Rheology and thermal conductivity of diamond powder-filled liquid

epoxy encapsulants for electronic packaging. *IEEE Trans. Compon. Pack. Technol.* **2009**, *32*, 716-23.

[180].Morgen, M.; Ryan, E. T.; Zhao, J. H.; Hu, C.; Cho, T.; Ho, P. S. Low dielectric constant materials for ULSI interconnects. *Annu. Rev. Mater. Sci.* **2000**, *30*, 645-80.

[181].Maex, K.; Baklanov, M. R.; Shamiryan, D.; Iacopi, F.; Brongersma, S. H.; Yanovitskaya, Z. S. Low dielectric constant materials for microelectronics. *J. Appl. Phys.* **2003**, *93*, 8793-841.

[182].Oqawa, E. T.; Lee, K. D.; Blaschke, V. A.; Ho, P. S. Electromigration reliability issues in dual-damascence Cu interconnections. *IEEE Trans. Reliab.* **2002**, *61*, 403-19.

[183].Michaelides, S.; Sitaraman, S. K. Die Cracking and Reliable Die Design for Flip-Chip Assemblies. *IEEE Trans. Adv. Packag.* **1999**, *22*, 602-13.

[184].Tsai, M. Y.; Hsu, C. H. J.; Wang, C. T. O. Investigation of thermomechanical behaviors of flip chip BGA packages during manufacturing process and thermal cycling. *IEEE Trans. Compon. Pack. Technol.* **2004**, *27*, 568-76.

[185].Liu, Y.; Wang, Y. F.; Gerasimov, T.G.; Heffner, K. H.; Harmon, J. P. Thermal analysis of novel underfill materials with optimum processing characteristics. *J. Appl. Polym. Sci.* **2005**, *98*, 1300-7.

[186].Chen, L.; Zhang, Q.; Wang, G. Z.; Xie, X. M.; Cheng, Z. N. The effects of underfill and its material models on thermomechanical behaviors of a flip chip packaging. *IEEE Trans. Compon. Pack. Technol.* **2001**, *24*, 17-24.

[187].Wray, K. L.; Connolly, T. J. Thermal conductivity of clear fused silica at high temperatures. *J. Appl. Phys.* **1959**, *84*, 1702-5.

[188].Slack, G. A. Thermal conductivity of pure and impure silicon, silicon carbide, and diamond. *J. Appl. Phys.* 35, 3460-6.

[189].Prasher, R. Thermal Interface Materials: Historical Perspective, Status, and Future Directions. *Proc. IEEE* **2006**, *94*, 1571-86.

[190].Sun, Y. Y.; Zhang, Z. Q.; Wong, C. P. Study on Mono-Dispersed Nano-Sized Silica by Surface Modification for Underfill Applications. *J. Colloid Interf. Sci.* **2005**, *292*, 436-44.

[191].Lavrenko, V. A.; Pugach, E. A.; Filipchenko, S. I.; Gogotsi, Yu. G. High temperature oxidation of silicon carbide based materials. *Oxid. Met.* **1987**, 27, 83-93.

[192]. Lau, K. T.; Gu, C.; Hui, D. A critical review on nanotube and nanotube/nanoclay related polymer composite materials. *Composites Part B-Engineering* **2006**, *37*, 425-36

[193].Wei, C. Y.; Srivastava, D.; Cho, K. Thermal expansion and diffusion coefficient of carbon nanotube-polymer composites. *Nano Lett.* **2002**, *2*, 647-50.

[194].Bauer, M.; Bauer, J.; Hamerton, I. (Editor), Aspect of the kinectics, modeling and simulation of network building up during cyanate ester cure. *Chemistry and Technology of Cyanate Ester Resins* **1994***,* 58-86, Chapman & Hall, London,.

[195].Liang, Q. Z.; Wong, C. P. Generation of phonon coupler across the interface between aligned graphitic nanoplates and substrates. *Georgia Tech Invention disclosure.*

[196].Liang, Q. Z.; Wong, C. P. Generation of phonon coupler among graphitic nanoplates. *Georgia Tech Invention disclosure.*

[197].Lin, W.; Xiu, Y. H.; Jiang, H. J.; Zhang, R. W.; Hildreth, O.; Moon, K. –S. Wong, C. P. Self-Assembled Monolayer-Assisted Chemical Transfer of In Situ Functionalized Carbon Nanotubes. *J Am Chem Soc* **2008**, *130*, 9636-7.

[198].Lee, W. S.; Han, I. Y.; Yu, J.; Kim, S. J.; Byun, K. Y. Thermal characterization of thermally conductive underfill for a flip-chip package using novel temperature sensing technique. *Thermochimica Acta* **2007**, pp.148–55.

[199].Yu, A.P.; Ramesh, P.; Itkis, M. E.; Bekyarova, E.; Haddon, R. C. Graphite Nanoplatelet-Epoxy Composite Thermal Interface Materials. *J. Phys. Chem.* C **2007**, *111*, 7565-7569.

[200].Xu, Y. S.; Chuang, D. D. L. Increasing the thermal conductivity of boron nitride and aluminum nitride particle epoxy-matrix composites by particle surface treatments", *Composite Interfaces* **2000**, *7*, 243–56.

VITA

QIZHEN LIANG

Qizhen Liang was born in Rizhao, Shandong Province, China in 1980. He obtained B.S. in Applied Chemistry/Polymer Materials and a M.S. in Polymer Materials from Dalian University of Technology, China in 2002 and 2005, respectively, In 2006, he come to School of Polymer, Textile and Fiber Engineering, Georgia Tech and joined Dr C. P. Wong's group in School of Materials Science and Engineering at Georgia Tech, as a PhD student and graduate research assistant. He is expecting his PhD in Polymer, Textile and Fiber Engineering in August 2011.